

DEPARTMENT OF PHYSICS AND ASTRONOMY

HEIDELBERG UNIVERSITY

Master thesis in Physics

submitted by

**KAREN WADENPFUHL**

born in Darmstadt (Germany)

2023

EMERGENCE OF SYNCHRONISATION  
IN A DRIVEN-DISSIPATIVE HOT RYDBERG VAPOUR

This Master thesis has been carried out by

KAREN WADENPFUHL

at the

Department of Physics, Durham University, under the supervision of

PROF. C. STUART ADAMS

and the

Physikalisches Institut, Heidelberg University, under the supervision of

PROF. MATTHIAS WEIDEMÜLLER

## ABSTRACT

---

Nonlinear systems display a wide range of rich and varied dynamics which are usually modelled in the framework of nonlinear dynamics and bifurcation theory. Adding dissipation to the system fundamentally changes the dynamics of the system and leads to the formation of even more interesting solutions, such as attractive limit cycles which represent phase oscillators. In an ensemble of coupled phase oscillators one can observe the onset of a collective response under certain coupling conditions, also known as synchronisation. Many effects that occur in nature have been attributed to synchronisation. However, an experimental study of synchronisation in ensembles of many coupled oscillators has proved challenging due to the lack of a suitable system. In this thesis, we report on the emergence of synchronisation in a driven-dissipative hot Rydberg vapour. Two-photon EIT spectroscopy of Rydberg states reveals oscillations in the bulk transmission of the probe laser by a thermal rubidium vapour at temperatures between 35 and 60 °C. Simulations of the hot vapour system support the interpretation of the observed oscillatory response as the onset of synchronisation in a driven-dissipative atomic system with global coupling via a Rydberg atom density field. The appeal of this system is twofold. Firstly, its wide tunability and fast oscillation frequencies on the order of 10 kHz allows for an exploration of the synchronisation transition over a large parameter space. Secondly, the Rydberg vapour contains  $\sim \mathcal{O}(10^9)$  atoms in the beam volume and a somewhat lower number of constituent oscillators, which gives access to a large number of coupled oscillators. Additionally, connections to continuous dissipative time crystals and other phenomena can be drawn, which adds another layer of interest.

## ZUSAMMENFASSUNG

---

Nichtlineare Systeme zeigen eine Bandbreite an vielfältigen Dynamiken, welche meistens im Rahmen der Theorie nichtlinearer Systeme und Bifurkationstheorie untersucht werden. Wenn man zu einem solchen System nun dissipative Elemente hinzufügt, dann können sich die daraus resultierenden dynamischen Verhaltensweisen des Systems fundamental ändern. Unter anderem können sich sogenannte *limit cycles* als Attraktoren ausbilden, sodass das System zur Klasse der Phasenoszillatoren gehört. Viele in der Natur auftretenden Effekte können als Synchronisation von gekoppelten selbstoszillierenden Einheiten, den Phasenoszillatoren, verstanden werden wobei das Ensemble einen kollektiven, synchronisierten Zustand einnimmt. Experimentell ist es schwierig Ensembles mit einer großen Anzahl an gekoppelten Phasenoszillatoren zu untersuchen, da entsprechende Systeme bisher fehlen. In dieser Arbeit stellen wir ein solches System vor, nämlich ein kontinuierlich getriebenes, dissipatives warmes Rydberg-Gas. Zwei-Photonen *EIT*-Spektroskopie von Rydbergzuständen zeigt Oszillationen in der Transmission des *probe*-Lasers durch ein warmes Rubidiumgas mit Temperaturen im Bereich von 35 bis 60 °C. Simulationen der Prozesse im Rydberg-Gas unterstützen die Interpretation der beobachteten Oszillationen als Signatur von Synchronisation der Atomzustände, wobei die Kopplung (indirekt) über die Rydbergzustandsdichte erfolgt. Das hier vorgestellte System ist aus zwei Gründen besonders interessant. Einerseits ermöglicht das System es einen weiten Parameterbereich zu erkunden, da die Rydbergzustände sehr versatil und veränderbar sind, und die schnellen Oszillationsfrequenzen in der Größenordnung von 10 kHz schnell ausgelesen werden können. Zum Zweiten sind etwa  $\sim \mathcal{O}(10^9)$  Atome im aktiven Strahlvolumen enthalten, wodurch eine große Anzahl an global gekoppelten Oszillatoren untersucht werden kann. Außerdem können Verbindungen zur Physik von kontinuierlichen, dissipativen Zeitkristallen sowie anderen bekannten Effekten hergestellt werden. Dies macht das System noch in einem weiteren Zusammenhang interessant.

# LIST OF PUBLICATIONS

Parts of this thesis have been published in the following publication, and figures in Chapters 4 and 5 have been adapted or reproduced from the publication.

EMERGENCE OF SYNCHRONISATION IN A DRIVEN-DISSIPATIVE HOT RYDBERG VAPOR

Karen Wadenpfehl and C. Stuart Adams

accepted for publication in *Physical Review Letters*

arXiv: [10.48550/arXiv.2306.05188](https://arxiv.org/abs/10.48550/arXiv.2306.05188)

# CONTENTS

<b>List of figures</b>	<b>1</b>
<b>1 Introduction</b>	<b>3</b>
<b>2 Atom-light interaction</b>	<b>5</b>
2.1 Semiclassical approximation	5
2.1.1 Two-level system, Rabi oscillations, and dressed states	6
2.1.2 Three-level system and electromagnetically induced transparency	7
2.2 Fine- and hyperfine structure of atoms	10
2.3 Additional effects occurring in a hot vapour	11
<b>3 Rydberg atoms</b>	<b>14</b>
3.1 General properties and scaling laws	14
3.1.1 Example application: rf field sensing	15
3.2 Rydberg-Rydberg interactions	16
3.2.1 Underlying mechanism: dipole-dipole interactions	17
3.2.2 Second-order interaction processes	20
3.2.3 Structure of the $C_6$ interaction coefficient	22
3.2.3.1 Angular dependency and angular momentum channels	24
3.2.3.2 Radial coupling strength	26
3.2.3.3 Energy defect	28
3.2.3.4 Structures in $C_6$ maps	29
3.2.3.5 Förster zero states in degenerate manifolds	30
3.2.4 Tunability of interactions with electric and magnetic fields	32
3.2.5 Example application: photon-photon interaction on demand	32
<b>4 Theoretical model</b>	<b>34</b>
4.1 Introduction to the model systems	35
4.2 Steady state solutions for a single velocity class	36
4.2.1 Effective 2-level model	36
4.2.2 Stability analysis of steady states in dynamical systems	40
4.2.3 3-level model	41
4.2.4 Hopf bifurcation	44
4.2.5 Behavior of the limit cycle region in the 3-level model	46
4.3 Scaling of interaction term	48

4.4	Hot vapour simulation for all velocity classes . . . . .	50
4.4.1	Synchronisation . . . . .	52
4.4.2	Behaviour of the limit cycle region in hot vapour simulations . . . . .	53
4.5	Relation to other models, effects, and phenomena . . . . .	56
4.5.1	Ergodicity breaking . . . . .	56
4.5.2	Time crystals . . . . .	57
4.5.3	Kuramoto model and nonequilibrium phase transitions . . . . .	57
4.6	Closing remarks . . . . .	58
<b>5</b>	<b>Oscillations</b>	<b>60</b>
5.1	Experimental setup . . . . .	61
5.2	Behaviour and scaling of oscillation region with experimental parameters . . . . .	63
5.2.1	Dependence of oscillations on Rabi frequencies . . . . .	63
5.2.2	Scaling with vapour density and Rydberg state . . . . .	64
5.2.3	Oscillation frequency scaling . . . . .	66
5.2.4	Shape and frequency of oscillations along scan . . . . .	67
5.3	Interpretation of the experimental results . . . . .	69
5.4	Open questions, outlook, and conclusion . . . . .	72
<b>6</b>	<b>Conclusion and outlook</b>	<b>75</b>
 <b>APPENDIX</b>		
<b>A</b>	<b>Steady-state solutions and stability analysis for driven systems</b>	<b>I</b>
A.1	Effective 2-level system . . . . .	I
A.2	3-level system . . . . .	V
<b>B</b>	<b>Interaction Hamiltonian for van der Waals-type interactions</b>	<b>X</b>
<b>C</b>	<b>Approximation of the plasma model</b>	<b>XV</b>
<b>D</b>	<b>Spatial distribution of atoms in a thermal vapour</b>	<b>XVIII</b>
<b>E</b>	<b>New TA-SHG laser @ 480 nm</b>	<b>XX</b>
<b>F</b>	<b>Cavity lock</b>	<b>XXI</b>
<b>G</b>	<b>Bibliography</b>	<b>XXIV</b>
<b>H</b>	<b>Acknowledgements</b>	<b>XXXVII</b>

# LIST OF FIGURES

1.1	Schematic representation of the synchronisation of three phase oscillators. . . . .	4
2.1	Rabi oscillations and dressed states in a two-level system. . . . .	6
2.2	EIT and Autler-Townes splitting in a three-level ladder ( $\Xi$ ) system. . . . .	8
2.3	Fine- and hyperfine structure of rubidium in a typical $\Xi$ Rydberg system. . . . .	9
2.4	Electric dipole allowed transitions and intensity radiation patterns. . . . .	10
2.5	Motion-induced detuning and transit-time broadening in a hot vapour. . . . .	11
3.1	RF field detection via EIT spectroscopy in a four-level scheme. . . . .	16
3.2	THz transitions accessible with two-photon schemes for Rb and Cs. . . . .	17
3.3	Angular dependency of dipole interaction operator $\hat{V}_{dd}$ . . . . .	18
3.4	Pair state system and coupling-induced shift of eigenstates from resonance. . . . .	19
3.5	Second-order interaction in the van der Waals regime and Rydberg blockade effect. . . . .	21
3.6	Structures in the $C_6$ coefficients of $P_J$ -states in rubidium. . . . .	23
3.7	Basis rotation and angular dependency of $ n_1P_{1/2}, n_2P_{1/2}\rangle$ angular momentum channels. . . . .	25
3.8	Radial coupling strength for low- $l$ dipole transitions in rubidium. . . . .	27
3.9	Förster resonances of the angular momentum channels coupled to $ n_1P_{1/2}, n_2P_{1/2}\rangle$ in rubidium. . . . .	28
3.10	Förster resonance structure and resulting angular dependency of $C_6(60S_{1/2}, n_2S_{1/2})$ in rubidium. . . . .	31
4.1	Level schemes for 2-level and 3-level model. . . . .	35
4.2	Bistability in the 2-level model. . . . .	38
4.3	Scaling of the bistable region in the 2-level model. . . . .	39
4.4	Multiple bifurcations in the 3-level model. . . . .	43
4.5	Hopf bifurcation in the 3-level model. . . . .	44
4.6	Limit cycles in the 3-level model. . . . .	45
4.7	Shape of limit cycles for variation of the bifurcation parameter. . . . .	46
4.8	Scaling of bistable and limit cycle regions in the 3-level model. . . . .	47
4.9	Two separate spectral regions with globally attractive limit cycles. . . . .	48
4.10	Temporal shape of limit cycle at different detunings. . . . .	49
4.11	Thermal vapour simulation leading to time-periodic response. . . . .	51
4.12	Local and global attractiveness of the hot vapour system. . . . .	53
4.13	Example limit cycle shapes in hot vapour system. . . . .	54

---

4.14	Contributing velocity classes, oscillation frequency entrainment, and phase freedom in limit cycle of thermal vapour system. . . . .	55
5.1	Bistability, hysteresis, and oscillations in the response of a thermal vapour. . . . .	60
5.2	Experimental setup and relevant level scheme of rubidium. . . . .	61
5.3	Onset of oscillations with increasing coupling Rabi frequency. . . . .	62
5.4	Scaling of oscillation regime with Rabi frequencies. . . . .	63
5.5	Scaling of oscillation region with experimental parameters. . . . .	65
5.6	Sudden break in oscillation region for $ 77D_{5/2}\rangle$ state. . . . .	65
5.7	Comparison of oscillation frequency in different regimes. . . . .	66
5.8	Change in frequency and shape of oscillations along scan. . . . .	67
5.9	Example traces in oscillation regime. . . . .	68
5.10	Pair interaction potentials and Stark shifts for $43D_{5/2}$ , $50D_{5/2}$ , $63D_{5/2}$ and $79D_{5/2}$ states in rubidium. . . . .	71
5.11	Phase drift of oscillations in a single realisation. . . . .	73
C.1	Electric microfield strength distribution induced by different charge densities. . . . .	XVI
D.1	Spatial distribution of particles in $d$ dimensions. . . . .	XIX
F.1	Schematics of cavity lock. . . . .	XXI
F.2	Optical setup of cavity lock for two lasers at $\sim 960$ nm. . . . .	XXII
F.3	Electronics setup of cavity lock. . . . .	XXIII

# 1 | INTRODUCTION

Have you ever sat in an audience and noticed the applause change from chaotic clapping to a rhythmic pattern? Ever wondered why slightly detuned metronomes placed on a common baseplate tick together, and why fireflies flash in unison? Or why an ensemble of Rydberg atoms responds collectively to continuous driving, even though each atom individually is subject to random motion?

As different as these situations may seem, the underlying processes are very similar. All instances can be abstracted to an ensemble of constituents that undergo their own periodic processes which, eventually, begin to align to a single, collective response. This alignment of the periodic processes, however, does not happen by chance. The constituents cannot be thought of as independent of each other, rather there is some form of interaction between them. In the case of the audience this interaction is given by hearing the clapping of ones neighbor which might cause one to adjust one's own clapping pattern. As a result, a growing group of people begin to clap in synchrony which, in turn, compels even more people to adjust to this pattern until the entire crowd claps as one. This kind of process is a universal phenomenon known as synchronisation<sup>1</sup> [4, 5].

Synchronisation is ubiquitous in nature and has been employed to explain the examples above, but also many other processes such as pattern formation in chemical reactions [6–8] and the strong vibrations of the Millennium bridge in London on its opening day<sup>2</sup> [10]. A detailed understanding of the conditions required for the emergence of synchronisation is therefore key to understanding many phenomena that occur in our environment. The mathematical study of synchronisation has made many advances since the first discussions of the phenomenon by Winfree [11] and, later, Yoshiki Kuramoto [12]. However, even though many processes have been described using the framework of nonlinear dynamics and synchronisation, it is still challenging to probe and study the phenomenon for very large numbers of coupled oscillators. Ideally, the test system would be easy to implement, simple to monitor, and have a set of widely tunable parameters. For low numbers of oscillators, such experiments have been performed e.g. with two pendula fixed to a common support [13] or metronomes placed on a moving baseplate [2]. For large numbers of coupled oscillators, the demands on the system are hard to come by – particularly the tunability of the coupling strength and the other parameters is difficult to obtain in generic systems.

---

<sup>1</sup>References for the examples mentioned above are: synchronisation of applause in an audience [1], of coupled metronomes [2] and the flashing of fireflies [3].

<sup>2</sup>This interpretation is contested, mechanisms other than synchronisation could also be employed to explain the strong lateral vibrations. See e.g. [9].

In this thesis we report on the emergence of synchronisation in a driven-dissipative hot Rydberg vapour. The system consists of an estimated  $\sim \mathcal{O}(10^7)$  coupled oscillators with widely tunable parameters and coupling strengths. Additionally, the setup and monitoring of the system is easily done in an atomic physics laboratory. The oscillation frequency on the order of 10 kHz permits real-time monitoring and quick feedback, as opposed to other known and controlled instances of synchronisation like in the Belousov-Zhabotinsky reaction [14, 15].

To lead towards the experiment and provide an understanding of the mechanisms causing the emergence of synchronisation in our system, the thesis starts with a description of the fundamental building blocks of our experiment. That is, the framework to describe interactions of individual atoms with light is outlined in Chapter 2. The exaggerated properties of highly-excited atomic states, so-called Rydberg atoms, is introduced in Chapter 3 with a particular focus on the strong second-order interactions between pairs of Rydberg atoms. These chapters set the prerequisites required for the remainder of the thesis, where a theoretical study and simulations of a hot Rydberg vapour in Chapter 4 is followed by a presentation of the experimental results in Chapter 5. We first show that a dissipative three-level system with a power-law shift of the Rydberg state is attracted towards limit cycles under certain conditions, and that interactions via a global mean field lead to synchronisation of the dynamics of individual atoms in a hot vapour simulation. As a result, oscillations of the bulk quantities of the driven-dissipative hot Rydberg vapour are predicted. We then show the experimental observation of persistent oscillations in the transmission of a probe laser in a three-level Rydberg EIT configuration. The behaviour of the resulting oscillation regime with changes in the experimental parameters is presented and possible mechanisms are discussed. Detailed calculations and derivations as well as further information on the experimental setup can be found in the appendices.

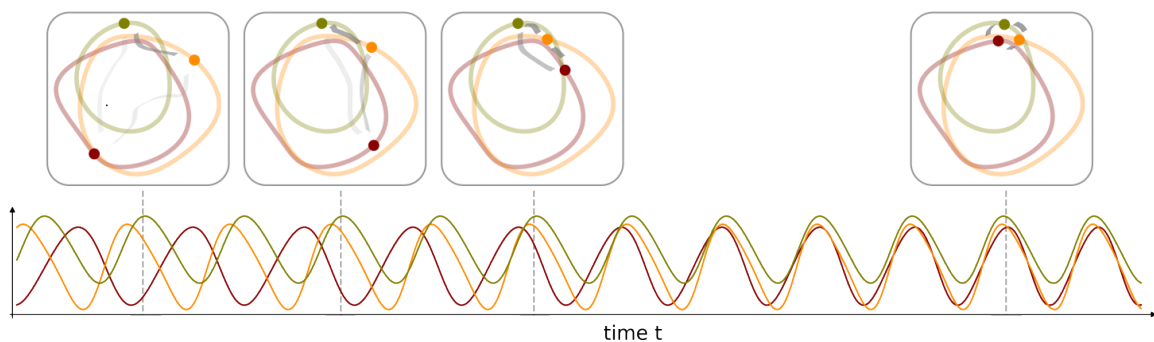


**Fig. 1.1: Schematic representation of the synchronisation of three phase oscillators.** The phase space trajectories of three phase oscillators are shown in the insets, with the dot indicating the state of the system at a given time  $t$ . A coupling between the oscillators (gray) induces a force which entrains the oscillators in frequency and phase on their limit cycles. As a result, synchronisation emerges.

## 2 | ATOM-LIGHT INTERACTION

The object of interest in this thesis is a driven-dissipative hot Rydberg vapour and some notable processes occurring therein. However, in order to understand the relevant phenomena we must first revisit the fundamentals of atom-light interactions. The semiclassical approximation and the resulting framework for a description of the atom-light system are introduced first, and some well-known effects are discussed. This semiclassical treatment of an  $n$ -level system is usually an idealisation of the actual situation, which presents itself as more complex. Complications are, among others, Doppler broadening and associated motion-induced effects as well as the complex level structure of atoms on the fine- and hyperfine level. These effects, and how one can incorporate them into a semiclassical description of the light-matter interaction, are therefore briefly mentioned at the end of the chapter.

### 2.1 SEMICLASSICAL APPROXIMATION

When working in the regime of quantum optics, one usually deals with single or few photons and an ensemble of individual to many atoms [16]. In such a situation, both the atomic and the photonic part of the system have to be quantised in order to provide a useful description of the atom-photon system. For strongly driven systems in the many-photon limit, one needs not quantise the photonic field in order to arrive at a useful description of the system [16]. The resulting semiclassical approximation can account for e.g. the well-known effects of Rabi oscillation [17], electromagnetically induced transparency (EIT) [18], and Autler-Townes splitting [19].

In the semiclassical approximation, light is treated as a classical field  $\mathbf{E}$  while the atomic component is quantised into discrete energy states  $\{|1\rangle, |2\rangle, \dots, |n\rangle, \dots\}$  as is encapsulated in the single-atom Hamiltonian  $\hat{\mathcal{H}}_0$ . These atomic states are coupled via resonant driving by the light field, such that the photon energy matches the energy difference of the atomic states and a population transfer is induced between the states. The dipole coupling strength between two atomic levels is quantified via the Rabi frequency<sup>1</sup>  $\Omega_{ij} = \langle i | \hat{\mathbf{d}} \cdot \hat{\mathbf{E}}_0 | j \rangle / \hbar$ , where  $\hat{\mathbf{d}} = e\hat{\mathbf{r}}$  denotes the dipole operator. Additionally, decay channels introduce dissipative dynamics into the system and can fundamentally change the resulting behaviour. For the remainder of this thesis we assume that the atomic basis is complete insofar as all decay occurs within the basis set and no atomic population is lost. This is enshrined in the trace condition for the density matrix  $\text{tr}(\hat{\rho}) = 1$ .

---

<sup>1</sup> $\mathbf{E}_0$  denotes the amplitude of the electric field  $\mathbf{E}$ , including spatial orientation.

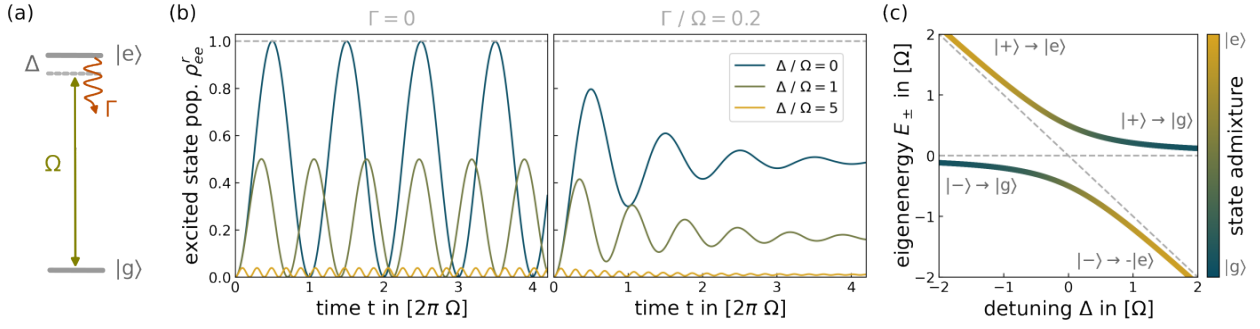


**Fig. 2.1: Rabi oscillations and dressed states in a two-level system.** The 2-level atom-light system is shown schematically in (a) and the resulting dynamics in (b). In the case of no decay from the excited state, Rabi oscillations persist (left). These oscillations are damped and quickly fade out when the decay is included (right). (c) The eigenenergies  $E_{\pm}$  of the dressed states  $|\pm\rangle$  and the state admixture  $\chi_{\pm} = |\langle i|\pm\rangle|^2$  for  $|i\rangle \in \{|g\rangle, |e\rangle\}$  are colour-encoded.

### 2.1.1 TWO-LEVEL SYSTEM, RABI OSCILLATIONS, AND DRESSED STATES

The simplest case is that of a two-level system with ground and excited states  $|g\rangle$  and  $|e\rangle$ , respectively, as shown in Figure 2.1 (a). The levels are coupled via a light field of Rabi frequency  $\Omega$  and detuning<sup>2</sup>  $\Delta$ , and the excited state decays into the ground state at rate  $\Gamma$ . In the dipole and rotating wave approximations [16], the atom-light Hamiltonian is given by  $\hat{\mathcal{H}}_{AL} = -\hat{\mathbf{d}} \cdot \hat{\mathbf{E}}_0$  which results in an overall single-atom Hamiltonian

$$\mathcal{H} = \mathcal{H}_0 + \mathcal{H}_{AL} = \frac{\hbar}{2} \begin{pmatrix} 0 & \Omega \\ \Omega & -2\Delta \end{pmatrix}. \quad (2.1)$$

The coherent time evolution of the system is governed by the von Neumann equation<sup>3</sup> [16] and formulated in operator representation via the density matrix  $\hat{\rho}$

$$\frac{\partial \hat{\rho}}{\partial t} = -\frac{i}{\hbar} [\hat{\mathcal{H}}, \hat{\rho}]. \quad (2.2)$$

As a result, one finds that a two-level system subject to constant driving undergoes Rabi oscillations, as shown in Figure 2.1 (b). The population oscillation frequency is given by the effective Rabi frequency  $\Omega_{\text{eff}} = \sqrt{\Omega^2 + \Delta^2}$  which depends on the detuning from the excited state, as does the magnitude of population that oscillates between the two states.

Analysing the Hamiltonian  $\hat{\mathcal{H}}$  reveals an interesting effect for strong coupling  $\Omega$ . The light-induced coupling of the bare atomic states produces a new set of eigenstates  $|\pm\rangle$  of the Hamiltonian, the so-called dressed states, which are a mixture of the bare states. Their corresponding eigenenergies are given by  $E_{\pm} = \frac{\hbar}{2} (-\Delta \pm \sqrt{\Delta^2 + \Omega^2})$ . On resonance where  $\Delta = 0$ , the eigenstates are not degenerate as one might initially expect, but have an energy splitting of  $\Omega$ . This

<sup>2</sup>For an atomic transition of frequency  $\omega_0$  and a driving field of frequency  $\omega$ , the detuning  $\Delta$  from resonance is defined as  $\Delta = \omega - \omega_0$ .

<sup>3</sup>At this stage, the time evolution can equivalently be described by the well-known Schrödinger equation. The framework of the von Neumann equation is chosen here due to the introduction of dissipation and dephasing later in the chapter.

results in an avoided crossing of the system's eigenstates  $|\pm\rangle$  as can be seen in Figure 2.1 (c). Such dressing of a pair of atomic states via strong coupling has been observed in a wide range of systems and has found applications in e.g. terahertz field sensing [20].

However, real-world systems rarely ever behave as neatly coherent as was shown above. Usually, the states are subject to decay and additional dephasing of the atomic coherences, e.g. via laser phase noise. This can be included by extending the von Neumann equation (2.2) with the Lindblad superoperator [21]

$$\mathcal{D}(\hat{\rho}) = \sum_{ij} \left( L_{ij} \hat{\rho} L_{ij}^\dagger - \frac{1}{2} \left[ L_{ij}^\dagger L_{ij}, \hat{\rho} \right]_{\text{PB}} \right) \quad (2.3)$$

where  $[\cdot, \cdot]_{\text{PB}}$  denotes the Poisson bracket. The operators  $\hat{L}_{ij}$  represent the decay channels for  $i \neq j$  and the dephasing of atomic coherences for  $i = j$ . In bra-ket representation, the operators are denoted as  $L_{ij} = \sqrt{\Gamma_{ij}} |i\rangle \langle j|$  with  $\Gamma_{ij}$  being the corresponding decay or dephasing rate. The resulting time evolution of the density matrix is then determined by the quantum Liouville (Lindblad) equation

$$\frac{\partial \hat{\rho}}{\partial t} = \mathcal{L}(\hat{\rho}) = -\frac{i}{\hbar} \left[ \hat{\mathcal{H}}, \hat{\rho} \right] + \mathcal{D}(\hat{\rho}). \quad (2.4)$$

Accounting for incoherent processes leads to significantly different behaviour of the system. Figure 2.1 (b) shows Rabi flopping of a two-level system without decay, this coherent dynamic would continue infinitely if the system remained unperturbed. The right panel, however, shows a system subject to decay from the excited to the ground state. This decay leads to strong damping of the Rabi oscillations which eventually fade out such that the system is attracted toward a steady state.

The damping of the coherent dynamics has caused experimentalists severe headaches over the years, and many different approaches have been trialled to increase the coherence time of the experiments. Many of them are based on ultracold setups and selection of (meta-)stable states as well as improving performance of the laser systems and field controls, though other avenues have been explored as well [22, 23].

### 2.1.2 THREE-LEVEL SYSTEM AND ELECTROMAGNETICALLY INDUCED TRANSPARENCY

When adding a third level to the system, one finds another remarkable quantum mechanical effect called electromagnetically induced transparency (EIT). The system can have any of the three configurations  $\Xi$ ,  $V$  or  $\Lambda$ , depending on the energetic configuration of the states [18]. Two states are coupled to the third via dipole coupling, and the decay rates have to be set as appropriate. Figure 2.2 (a) shows the schematic structure of a ladder ( $\Xi$ ) configuration of states where ground and excited state are coupled via the probe laser while the coupling laser drives the  $|e\rangle \leftrightarrow |r\rangle$  transition.

When monitoring the transmission of the probe laser through an ensemble of such three-level systems, one observes a sudden change in the probe transmission around two-photon resonance. This is caused by destructive interference of excitation pathways [18], resulting in reduced absorption of the probe laser. As a result, a so-called dark state forms which is completely

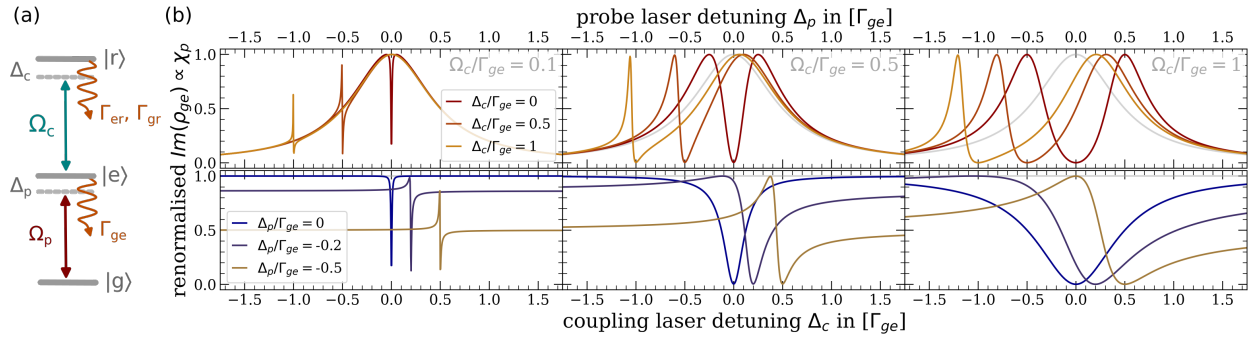


**Fig. 2.2: EIT and Autler-Townes splitting in a three-level ladder ( $\Xi$ ) system.** (a) shows a schematic representation of a three-level  $\Xi$  system including the relevant decay rates. (b) The resulting spectral response of the system is shown for different probe powers increasing towards the right. The upper row of panels shows a scan of the probe laser detuning for fixed coupling laser detunings  $\Delta_c$  while the lower row shows the corresponding scan of the coupling laser detuning for fixed  $\Delta_p$ . The other system parameters are set to  $\Omega_p/\Gamma_{ge} = 0.02$ ,  $\Gamma_{er}/\Gamma_{ge} = 10^{-3}$  and  $\Gamma_{gr} = 0$ , and no dephasing of the atomic populations or coherences was taken into account.

decoupled from the strongly decaying intermediate state  $|e\rangle$  and contains only the (meta-)stable states  $|g\rangle$  and  $|r\rangle$ . Figure 2.2 (b) shows the imaginary part of the electric susceptibility  $\chi_p$ , which is a measure for the absorption of the probe light by the vapour – and is therefore related to the vapour’s transmission.

The response of the vapour and the resulting shape of the EIT resonance depends strongly on the parameters of the system including decay rates, detunings, and coupling strengths. Increasing the coupling Rabi frequency leads to an initial change in EIT amplitude at low  $\Omega_c$  before the resonance begins to split as one enters the Autler-Townes split regime at high  $\Omega_c$ . In this regime, the spectral separation of the EIT peaks grows linearly with coupling Rabi frequency as is expected for a pair of dressed states. The strong dependence of the EIT resonance on the coupling field strengths and state dressing by additional resonant fields has been utilised in radiofrequency (rf) field measurement techniques [24] and atom-based broadband receivers [25, 26].

Another curious effect, namely that of slow and fast light [27], is linked to EIT since the medium displays a strongly varying refractive index<sup>4</sup> near two-photon resonance. Steep changes of the refractive index at a given frequency lead to extreme group velocities<sup>5</sup> at this frequency. This effect has been used to slow light down to 17 m/s [28] by inducing a delay to a light pulse with respect to one travelling outside the medium.

Such a continuous-wave (cw) scheme cannot, however, be used to stop light completely. If one wishes to do so, one needs to employ an adiabatically pulsed scheme [29] where the photon is converted into an atomic spin-wave excitation [30–32]. This strongly coupled atom-light

<sup>4</sup>The complex refractive index  $n$  of a medium is linked to the electric susceptibility  $\chi$  via  $n = \sqrt{1 + \chi}$ . The electric susceptibility is composed of the bulk properties of the medium determining the magnitude  $\chi_0$ , as well as the microscopic properties derived from the density matrix  $\rho$  which determine the shape of the resonance.

<sup>5</sup>The group velocity  $v_{gr}$  of the probe field at frequency  $\omega$  can be calculated from the real part of the probe refractive index  $n_p$  as  $v_{gr}(\omega) = c \cdot \left( n_p(\omega) + \omega \frac{dn_p}{d\omega} \right)^{-1}$ . See also e.g. [18] for further details.

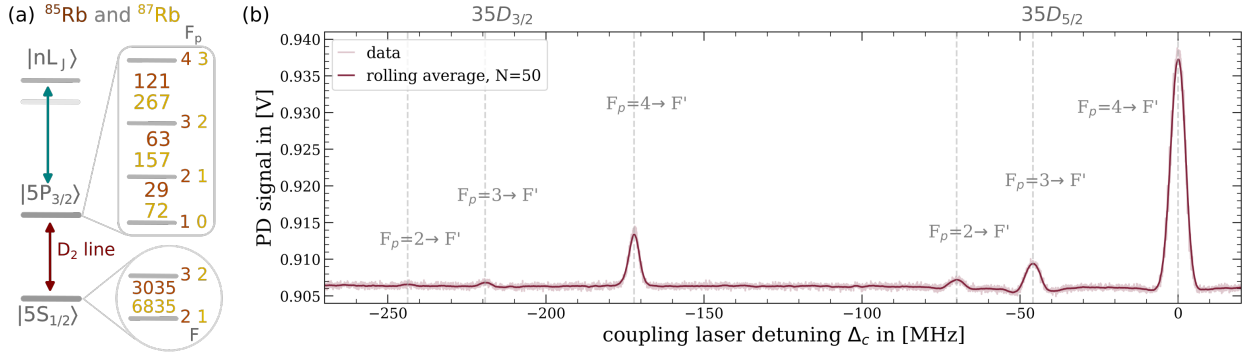


**Fig. 2.3: Fine- and hyperfine structure of rubidium in a typical  $\Xi$  Rydberg system.** The resolvable hyperfine levels of the  $|5S_{1/2}\rangle$  ground state and  $|5P_{3/2}\rangle$  on the  $D_2$  transition of rubidium at 780 nm are shown in (a). Hyperfine state energy splitting values are given in MHz for the  $^{85}\text{Rb}$  (dark orange) and  $^{87}\text{Rb}$  (light yellow) isotopes. The fine structure of the  $|nD\rangle$  series is resolved in standard experiments for  $n \leq 100$  [43] while the  $|nS\rangle$  state has just a single possible fine structure value  $j = 1/2$ . The hyperfine structure splitting of Rydberg states is usually  $< \text{MHz}$  and therefore not resolved in standard experiments. The transition to the  $|nL_J\rangle$  Rydberg states has a wavelength of around 480 nm. (b) shows an example coupling laser scan across the  $|35D\rangle$  states of the  $^{85}\text{Rb}$  isotope for a counterpropagating geometry. The spectrum reveals the fine-structure splitting of the Rydberg state, rescaled by  $\times(\lambda_c/\lambda_p)$  due to Doppler mismatch, as well as the hyperfine structure of the intermediate  $|5P_{3/2}\rangle$  state, rescaled by  $\times(1 - \lambda_c/\lambda_p)$  [43]. The probe laser was locked  $\Delta_p/2\pi = -140$  MHz below the  $|5S_{1/2}, F = 3\rangle \leftrightarrow |5P_{3/2}, F_p = 4\rangle$   $D_2$  line of  $^{85}\text{Rb}$ .

system forms a quasiparticle called polariton which inherits properties from both light and matter. Polaritons have been used for many applications, e.g. simulation of the Gross-Pitaevskii equation [33], Bose-Einstein condensation [34, 35] at room temperature [36] and in thermal equilibrium [37], coherent control of quantum states [38, 39], and the generation of an effective interaction between photons [40–42].

EIT can therefore be used as a spectroscopic technique to detect atomic states via two-photon resonance [43, 44], but can similarly be utilised as a tool in spatial imaging techniques [45]. Hot vapour EIT systems have been developed as useful tools for vector field measurements in electrometry [46, 47] and magnetometry [48, 49]. Equivalently, the EIT dark state is used to store and retrieve single photons on demand [50], thereby constituting the building block of a deterministic single photon source, or as a quantum memory [51, 52]. In the experimental part of this thesis, EIT is used as a spectroscopic method to coherently probe highly excited atomic states, so-called Rydberg states.

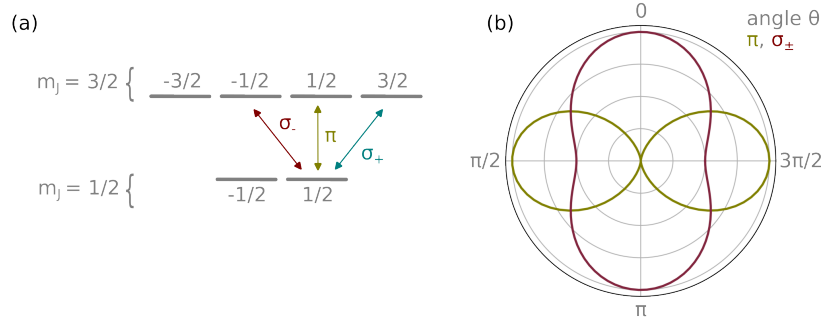


**Fig. 2.4: Electric dipole allowed transitions and intensity radiation patterns.** (a) shows the different dipole-allowed transitions with respective angular momentum state changes on the fine-structure level. The intensity radiation pattern of  $\pi$  (olive) and  $\sigma_{\pm}$  (red) electric dipole transitions is shown in (b). The angle  $\theta$  denotes the angle between quantisation axis and the observer, and the radiation patterns have the angular dependencies  $I_{\pi} \propto \sin^2(\theta)$  and  $I_{\sigma} \propto (1 + \cos^2(\theta))/2$ .

## 2.2 FINE- AND HYPERFINE STRUCTURE OF ATOMS

Experimentally, it may not be entirely straightforward to isolate  $n$  levels in an atomic system. The fine- and hyperfine splitting<sup>6</sup> of low-lying atomic states is comparably large, for instance the rubidium ground state  $|5S_{1/2}\rangle$  is split on the order of gigahertz<sup>7</sup> and the  $|5P_{3/2}\rangle$  state hyperfine splitting is still on the order of 100 MHz [54, 55]. However, this is not the case for highly excited Rydberg states where the hyperfine structure scales with the effective principal quantum number  $(n^*)^{-3}$  [56], and even the fine structure splitting cannot easily be resolved for very highly excited states.

Figure 2.3 shows an example three-level EIT spectrum of a scan across the  $|35D\rangle$  resonance of  $^{85}\text{Rb}$ . The hyperfine structure of the intermediate  $|5P_{3/2}, F_p\rangle$  state is resolved but rescaled by the Doppler mismatch of a counterpropagating geometry [43]. Only the fine structure of the Rydberg state is resolved because the hyperfine energy splitting is much lower than the EIT linewidth.

Applying external electric or magnetic fields lifts the degeneracy of the angular momentum manifold via Stark and Zeeman splitting, respectively. This allows to address the specific angular momentum states  $m_j$  via frequency and polarisation matched coupling fields [57]. The polarisation of the light field with respect to the quantisation axis determines the transition that is driven ( $\pi$ ,  $\sigma_{\pm}$ ). It therefore addresses only pairs of states with a matching difference in orbital angular momentum<sup>8</sup>, i.e.  $\Delta m_j = 0, \pm 1$  for electric dipole allowed transitions<sup>9</sup>. The different

<sup>6</sup>The atomic fine structure originates in spin-orbit coupling to a total orbital angular momentum  $\mathbf{J}$  while the hyperfine structure arises from an additional coupling with the nuclear angular momentum to the total angular momentum  $\mathbf{F}$ . More details on the coupling and limits of applicability of the different quantum numbers can be found in the literature, e.g. in [53].

<sup>7</sup> $^{85}\text{Rb}$  has a ground-state hyperfine splitting of 3.0 GHz and  $^{87}\text{Rb}$  of 6.8 GHz [54, 55].

<sup>8</sup>This assumes an electric dipole transition. Higher-order electric transitions like quadrupole, or magnetic transitions, can also be coupled but are usually much weaker and therefore neglected.

<sup>9</sup>The selection rules for electric dipole-allowed transitions state that  $\Delta l = \pm 1$ ,  $\Delta j = 0, \pm 1$ , and  $\Delta m_j = 0, \pm 1$  must be satisfied. Further conditions apply in certain cases, like e.g. ( $j = 0 \leftrightarrow j' = 0$ ) or ( $\Delta j = 0, \Delta m_j = 0$ ) are forbidden.

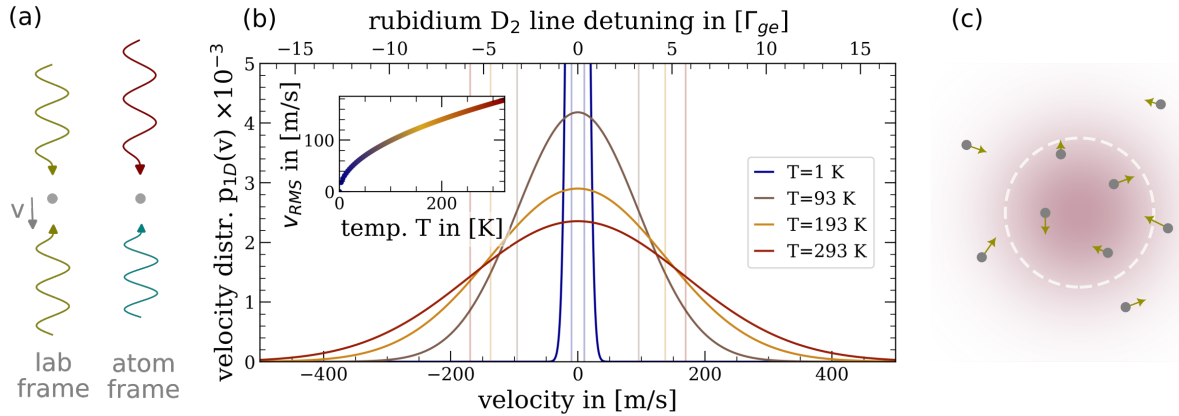


**Fig. 2.5: Motion-induced detuning and transit-time broadening in a hot vapour.** The motion-induced Doppler detuning is shown schematically in (a) and the resulting detuning of a thermal ensemble of rubidium atoms from the D<sub>2</sub> line in (b). The thin lines indicate the root mean square (rms) velocity at different temperatures and the inset shows  $v_{rms}$  for rubidium. In (c), the effect of transit-time broadening is shown. Excited atoms fly out of the beam volume while ground-state atoms move in, leading to an effective decay from every excited state level to the ground state. As shown in (c), the calculation of the transit-time decay rate  $\Gamma_{tt}$  is simplified by considering only the  $1/e^2$ -radius of the beam.

transitions have different spatial intensity radiation patterns with respect to the quantisation axis, as shown in Figure 2.4 (b). This property is relevant to keep in mind when e.g. designing imaging schemes for experiments or using optical pumping schemes.

The fine structure of atomic states as well as the angular dependency of the electric dipole allowed transitions will be relevant again in Chapter 3. In the experimental Chapter 5, EIT scans of a hot rubidium vapour akin to that in Fig. 2.3 will be shown, and the level structure of Rubidium is of relevance.

### 2.3 ADDITIONAL EFFECTS OCCURRING IN A HOT VAPOUR

The generic semiclassical  $n$ -level treatment seems to be fairly straightforward to use. One writes down the equations of motion following from consideration of all possible coupling and decay mechanisms, and then integrates or solves for the steady state. The fine- and hyperfine structure of the atoms complicates the situation a little as it introduces more levels that might have to be taken into account, depending on the polarisation-dependent coupling of states and possible state shifts due to electric or magnetic fields.

Nevertheless, the list of real-world complications is much longer. In a hot vapour, one additionally has to take the atomic motion into account which results in motion-induced detuning and dephasing, transit-time broadening, and collision-induced ionisation [21]. As a result, the response of a hot vapour looks significantly different to that of an ultracold ensemble at similar densities.

### *Motion-induced detuning and dephasing*

The Doppler effect is well-known from the perceived change in frequency of the horn of a passing ambulance. The very same effect occurs in a hot<sup>10</sup> ensemble of atoms with a spread in velocity relative to the direction of propagation of the light field. Due to the Doppler effect, the light is detuned by  $\Delta\nu = -\mathbf{k} \cdot \mathbf{v}$  for atoms moving with velocity  $\mathbf{v}$  with respect to the ones being stationary in the lab frame. The laser's wavevector  $\mathbf{k}$  encodes the wavelength  $\lambda$  of the laser via the relation  $|\mathbf{k}| = 2\pi/\lambda$ , and additionally the direction of propagation of the light field.

Doppler detuning either has to be incorporated in the experiment or avoided by techniques such as saturated absorption (Doppler-free) spectroscopy. Additionally, different forms of motion-induced dephasing have plagued experimentalists, e.g. in single-atom ultracold experiments with optical tweezers or for the storage of quantum information in hot vapours. The solutions to reduce the effect depend on the problem, cooling to the motional ground state can be implemented in tweezer setups [58] while hot vapour spin wave experiments can utilise zero-wavevector schemes [59]. Difficult to control, however, is the effect of collisional dephasing in hot vapours [21].

### *Transit-time broadening*

Another consequence of atomic motion in hot vapour experiments is that atoms simply move out of the interaction volume of the laser beam(s). This behaviour could be prevented by exciting only a narrow class of atoms centered around the stationary velocity class [60, 61]. Without employing such schemes, one has to take transit-time broadening into account. The resulting effective decay rate  $\Gamma_{tt}$  can be approximately calculated for atoms with a velocity  $v$  perpendicular to the laser's direction of propagation to be

$$\Gamma_{tt}(v) \approx \frac{v}{w_0} \quad (2.5)$$

[21], where  $w_0$  denotes the  $1/e^2$ -beam waist of the light field. To get an approximate value for the transit time broadening in a hot vapour, one can set the velocity  $v$  to the 2D RMS velocity  $v_{2D \text{ RMS}}$  and set  $\Gamma_{tt} = \Gamma_{tt}(v_{2D \text{ RMS}})$ . As an estimate for the order of magnitude, one finds that  $\Gamma_{tt} \sim \mathcal{O}(100\text{kHz})$  for a rubidium vapour at room temperature and a beam diameter of 1 mm.

### *Collision-induced ionisation*

It has been mentioned before that atomic collisions in hot vapours lead to dephasing of the atomic coherences. They can also facilitate collision-induced state changes [62] or even ionise highly-excited atomic states, so-called Rydberg states. This Rydberg to ground-state collisional

---

<sup>10</sup>As is well known, statistical mechanics links the velocity distribution of particles in an (ideal) gas to a temperature via the Maxwell-Boltzmann velocity distribution. In this framework, a *cold* ensemble is understood to have only a very narrow spread of velocities while a *hot* ensemble has a correspondingly large spread. As a consequence, the mean velocity of the ensemble is irrelevant for the definition of hot and cold – only the spread in velocities is relevant for the classification. The crossover between hot and cold arguably depends on the experimenter and their research, a (not so) useful rule of thumb is to speak of a hot ensemble when the motion-induced detuning leads to a sizeable change of the resulting dynamics.

cross section grows with the effective principal quantum number  $n^*$  to the power of four [63] and has been shown to lead to the build-up of a weak plasma in strongly-driven hot Rydberg vapours [63–65].

*Why, then, work in a hot vapour?*

The obvious solution to all the motion-induced problems is to go ultracold, such that the atoms have a very narrow velocity distribution and basically do whatever one wants<sup>11</sup>. Miniaturised cold atom sources have been developed [68], and the robustness of the devices has been increased such that they are routinely sent into space as GPS time sources, or to produce Bose-Einstein condensates (BECs) aboard the ISS [66]. The issue that remains, even for highly optimised and industrialised devices, is the need for an ultrahigh vacuum as well as cooling sequences. Practical factors additionally set limits on the maximum feasible vapour densities that can be achieved in such a setup. All in all, these ultracold machines are highly useful for science but presently tend to be rather too complicated and costly for everyday applications by low-end users.

In the last few years, the fields of quantum communication and quantum sensing based on atomic vapours have gained traction. This led to the development of many applications in the fields of electromagnetic field sensing [20, 24, 69], biomedical imaging [70], telecommunication [25, 26], and quantum state memories [29, 51, 52, 71]. All these technologies are currently, or soon will be, made available on a large scale for many users. And many of the technologies presently in transition to a large-scale user platform are built on hot vapour technologies. The reason being simply that hot vapour setups are easier to build and maintain, more cost- and resource-effective, and much more flexible to handle than their ultracold counterparts. The motion-induced effects are currently the price to pay for the advantages of a hot vapour setup.

Dissipation in itself is not a problem, nor are motion-induced effects. First and foremost they are simply just a property of the system, and not even necessarily detrimental to a purpose. Sometimes they do not matter very much unless one pushes an application towards limiting cases. But dissipation can even be made actively useful as in dissipation-stabilised phases of matter [72] like continuous dissipative time crystals [73].

One feature that many of the aforementioned hot vapour technologies have in common is that they utilise Rydberg states and their exaggerated properties. The next section therefore introduces Rydberg atoms with their extreme properties, and provides some example use cases to demonstrate the versatility of Rydberg atomic systems.

---

<sup>11</sup>They might not do everything one wants them to, and working in an ultracold environment poses its very own challenges. What one does win is an excellent control of the temperature of the atomic cloud with temperatures as cold as hundreds of pK [66], which is orders of magnitude below the temperature of the cosmic microwave background at 2.7 K [67].

## 3 | RYDBERG ATOMS

Rydberg atoms have been described as being the *gentle giants* of atomic physics [74], and this unconventional description is certainly not unjustified. Even though there is no general convention on when one speaks of an excited atom being in a Rydberg state, this name is typically used for atoms with principal quantum number  $n \geq 15$ . These highly excited atoms have spatially huge electronic wavefunctions such that the excited electron is, on average, far displaced from the nucleus which results in exaggerated atomic properties. Rydberg atoms are therefore being used for a variety of applications ranging from radiofrequency (rf) field sensing [20, 24, 69] and nonlinear optics [41, 75–78] to quantum computing [76, 79–81] and simulation [82, 83]. One key property of Rydberg atoms utilised in many of the aforementioned fields and technologies is the strong interaction between Rydberg atoms in close spatial proximity [84]. This interaction can also be used to generate effective interactions between photons when mapping them onto Rydberg polaritons [40, 41, 85], leading to curious new states of light like photonic molecules [86]. Ultimately, this approach could lead to the generation of photon-photon interactions on demand.

It is therefore safe to say that Rydberg atoms are highly useful due to their extreme properties, particularly the strong interactions. This chapter will therefore introduce some of the most notable properties of Rydberg atoms, with a focus on the interactions between Rydberg states, and demonstrate the versatility of Rydberg atoms by discussing some example applications.

### 3.1 GENERAL PROPERTIES AND SCALING LAWS

Highly excited Rydberg states are weakly bound with a state energy just below the ionisation threshold and the electron being on average far displaced from the atomic nucleus [74, 84]. The resulting exaggerated atomic properties can be computed particularly easily for hydrogen-like atoms with a single valence electron – i.e. the alkali atoms like rubidium, for instance. In these hydrogen-like atoms one finds that the binding energy of Rydberg states generally follows a power law in the principal quantum number  $n$  scaling as  $n_*^{-2}$ . The power law scaling is not perfect in  $n$ , so one uses the effective principal quantum number  $n_* = n - \delta_{n,l,j}$  where the energy defect<sup>1</sup>  $\delta_{n,l,j}$  has to be determined experimentally for the different angular momentum states [87–89].

---

<sup>1</sup>The energy defect arises from the excited electron of low angular momentum states penetrating the nucleus with a small likelihood. Analytic expressions for the energy defect exist but the modified Rydberg-Ritz coefficients have to be determined experimentally. Experimental values for rubidium can be found in references [87–89].

Rydberg states feature particularly long state lifetimes scaling with  $n_*^3$  for low angular momentum states and  $n_*^5$  for so-called circular states [84], i.e. Rydberg states with  $l = n - 1$  which have only a single spontaneous decay channel to energetically lower-lying states with  $n' = n - 1$ . This results in long radiative lifetimes of the Rydberg states up to  $\sim \mathcal{O}(100 \mu\text{s})$ . One therefore also speaks of metastable states since the radiative decay timescales are much longer than typical ultracold experimental sequences. However, particularly in hot vapour experiments one finds significant population redistribution due to blackbody radiation induced state changes [90, 91] and atomic collisions. This populates not only energetically lower-lying states but also nearby states higher up in the energy ladder and leads to additional dipole interactions in the vapour, as well as to a reduction of the state lifetime. These blackbody radiation induced effects have also been observed experimentally [92, 93].

The large spatial extent of the electronic wavefunction leads to an increased collisional cross section scaling with  $n_*^4$  [59, 63], as well as a strongly enhanced sensitivity to electromagnetic fields with the polarisability of Rydberg states scaling as  $n_*^7$  [84]. External electromagnetic fields therefore provide an additional control parameter for the Rydberg state since one can easily change the state energies by applying a field, and then e.g. tune transition wavelengths within a certain range. This enhanced sensitivity to electromagnetic fields is also used in rf field sensing and imaging techniques in the previously almost inaccessible terahertz (THz) region of the electromagnetic spectrum.

### 3.1.1 EXAMPLE APPLICATION: RF FIELD SENSING

Rydberg atoms have been used as sensors in rf vector electrometry [47] and magnetometry [48], thereby allowing a measurement of electric or magnetic rf fields including their magnitude and polarisations. These atom-based radiofrequency field measurements have been shown to detect THz radiation powers on the order of nW in hot vapour systems [20]. A recent preprint [94] claims to have approached the standard quantum limit up to a factor of 2.6 for detection of microwave fields at  $\sim 37$  GHz with an optically thin sample of ultracold atoms. Setups operated at room temperature greatly reduce the complexity and increases flexibility of the measurement devices as opposed to ultracold atomic setups.

These rf measurement detection methods often utilise a four-level scheme as shown in Figure 3.1 (a), where the two Rydberg states  $|r\rangle$  and  $|r'\rangle$  are dipole-coupled by the rf field. Low rf field strengths (low  $\Omega_{\text{rf}}$ ) induce a change in the amplitude and shape of EIT resonance while strong fields with high Rabi frequencies  $\Omega_{\text{rf}}$  lead to Autler-Townes (AT) splitting of the EIT resonance. This crossover from EIT into the AT regime with increasing  $\Omega_{\text{rf}}$  is shown in Figure 3.1 (b). Tuning the detuning  $\Delta_{\text{rf}}$  of a strong rf field across resonance, on the other hand, reveals the avoided crossing of the dressed states in the EIT spectra as shown in Figure 3.1 (c). Dipole transition strengths between Rydberg states with small differences in principal quantum number  $n$  tend to be large due to the large overlap of the radial wavefunctions. This leads to high Rabi frequencies even for low field strengths and thereby enhances the sensitivity of the detectors.

The Rydberg atom-based rf detection schemes are of particular relevance in the terahertz (THz) domain (0.3 - 3 THz), which is sandwiched between the range of electronic and optical sensors and currently lacks efficient detection schemes. This THz gap can be closed by atom-based sensors since a multitude of transitions between Rydberg states lies within the THz do-

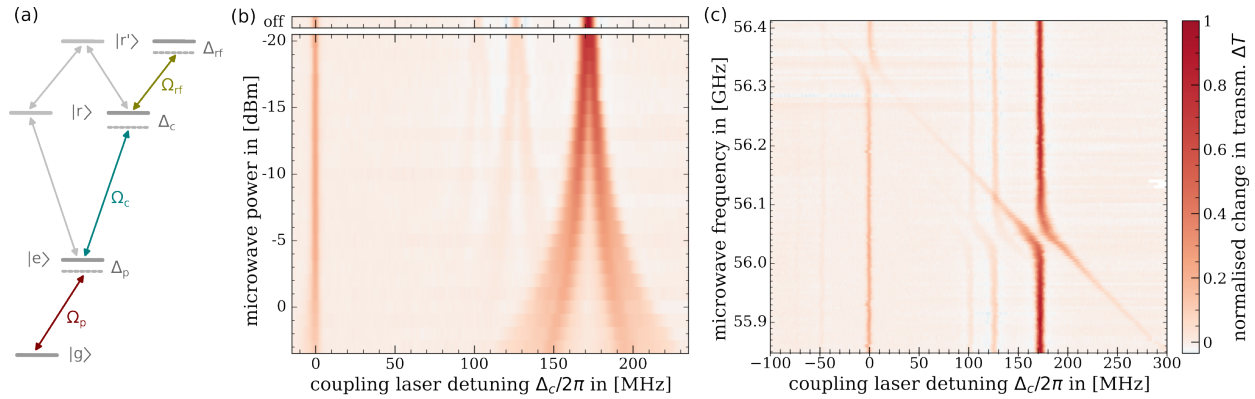


**Fig. 3.1: RF field detection via EIT spectroscopy in a four-level scheme.** For a four-level scheme, the relevant levels are shown in (a). Coloured arrows indicate the transitions driven in the examples shown in (b) and (c), where EIT was performed in a hot rubidium vapour with an additional microwave field coupling the Rydberg state  $|r\rangle = |35D_{5/2}\rangle$  to a second Rydberg state  $|r'\rangle = |34F\rangle$ . Furthermore, we have  $|g\rangle = |5S_{1/2}\rangle$  and  $|e\rangle = |5P_{3/2}\rangle$ . (b) shows the transition from EIT to Autler-Townes (AT) splitting when increasing the microwave power for the microwave driving to the  $j' = 7/2$  state. In the AT split regime in (c), one can see the avoided crossing of energy levels as the microwave frequency is swept across resonance with the  $|35D_{3/2}\rangle$  (left, at  $\Delta_c = 0$ ) and  $|35D_{5/2}\rangle$  (right) states. Data was taken with a microwave power set to  $P_{mw} = -3$  dBm, the corresponding electric field amplitude in the vapour can be calculated from the splitting of the states. One can nicely see the three  $|35D_{5/2}\rangle$  resonances split at the same microwave frequency, and the weaker  $|35D_{3/2}\rangle$  resonances split at their same respective frequencies. The colourbar applies to both (b) and (c).

main [59]. The THz frequencies accessible via two-photon detection schemes, as in 3.1 (a), are shown in Figure 3.2 for the two most commonly used alkalis, namely rubidium (red) and cesium (yellow). Recently, THz imaging schemes have been developed which utilise similar level schemes as in rf field detection [95].

## 3.2 RYDBERG-RYDBERG INTERACTIONS

Another notable property of Rydberg atoms is the strong interaction between pairs of Rydberg states in spatial proximity. The resulting interactions have been utilised in e.g. neutral atom quantum computing schemes to implement CNOT (controlled-NOT) gates [96], in quantum simulation to effectively implement Ising and Heisenberg spin Hamiltonians [82] or simulate the temporal evolution of systems governed by the Gross-Pitaevskii equation [33], and in quantum optics to create optical nonlinearities at the single-photon level [41, 78].

In experiments with excitation into a single Rydberg state  $|n, l, j\rangle$ , like in the experiments discussed in this thesis, one finds the interaction dominated by van der Waals interaction<sup>2</sup> between identical atoms. However, we will start with a brief discussion of the underlying mechanism to

<sup>2</sup>The blackbody radiation induced population redistribution, as well as collisional state changes, can admix certain amounts of other Rydberg states which might be dipole-coupled to the target Rydberg state. For simplicity, this effect will be assumed to be negligible.

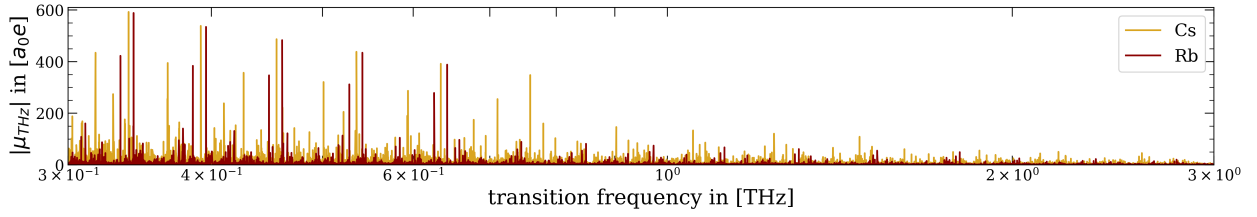


**Fig. 3.2: THz transitions accessible with two-photon schemes for Rb and Cs.** The THz transitions in Rb (red) and Cs (yellow), which are accessible with two-photon detection schemes as in 3.1 (a), are shown with their respective relative dipole matrix element  $|\mu_{THz}|$ .

explain the interactions on a fundamental level before the distance scaling of the interaction is considered for different regimes, and the resulting angular dependency is discussed in detail.

### 3.2.1 UNDERLYING MECHANISM: DIPOLE-DIPOLE INTERACTIONS

Rydberg atoms appear as electrically neutral at distances that are large compared to the spatial extent of their electronic wavefunction. This leads to a vanishing direct Coulomb interaction between two spatially separated Rydberg atoms. However, Rydberg atoms do interact with each other via dipole-dipole and weaker, higher-order electromagnetic interactions. They easily acquire a permanent electric dipole moment when subject to an external electric field due to the high polarisability of Rydberg states [97]. Additionally, when undergoing a state change an atom acquires a transient dipole moment for the duration of the transition between the states [16]. Two Rydberg atoms in spatial proximity can therefore interact via electromagnetic interactions, for which retardation effects of the fields are negligible while in the near field regime<sup>3</sup>. The resulting interaction can be calculated based on a multipole expansion [98, 99], which is well justified for non-overlapping charge distributions<sup>4</sup>. The leading term in the multipole expansion describes the interaction of two dipoles and is given by

$$\hat{V}_{\text{dd, cart}}^{(i,j)}(\mathbf{R}_{ij}) = \frac{1}{4\pi\epsilon_0 R_{ij}^3} \left[ \hat{\mathbf{d}}_i \cdot \hat{\mathbf{d}}_j - 3(\hat{\mathbf{d}}_i \cdot \mathbf{r}_{ij})(\hat{\mathbf{d}}_j \cdot \mathbf{r}_{ij}) \right] \quad (3.1)$$

with  $R_{ij} = |\mathbf{R}_{ij}|$  denoting the absolute distance between the atoms ( $i, j$ ) and  $\mathbf{r}_{ij} = \mathbf{R}_{ij}/R_{ij}$  the corresponding unit direction.  $\hat{\mathbf{d}}_i$  denotes the dipole operator acting on the  $i$ -th atom.

When performing a basis transformation from cartesian to spherical, with the quantisation

<sup>3</sup>With  $kR \ll 1$  where  $k$  denotes the wavevector of the respective transition and  $R$  the distance between the nuclei.

<sup>4</sup>The minimum interatomic distance required for a validity of the approach can be estimated from the spatial extent of the electronic wavefunctions and is given by the Le Roy radius  $r_{\text{LR}} = 2(\langle \hat{r}_1^2 \rangle + \langle \hat{r}_2^2 \rangle)$  [59, 100]. For states with non-vanishing angular momentum  $l \neq 0$ , however, it has been shown that the Le Roy radius may be an underestimate for the lower bound of the regime of applicability of the power-law scaling in interaction strength. An expression including the orientation of the orbital angular momenta has been proposed in [101].

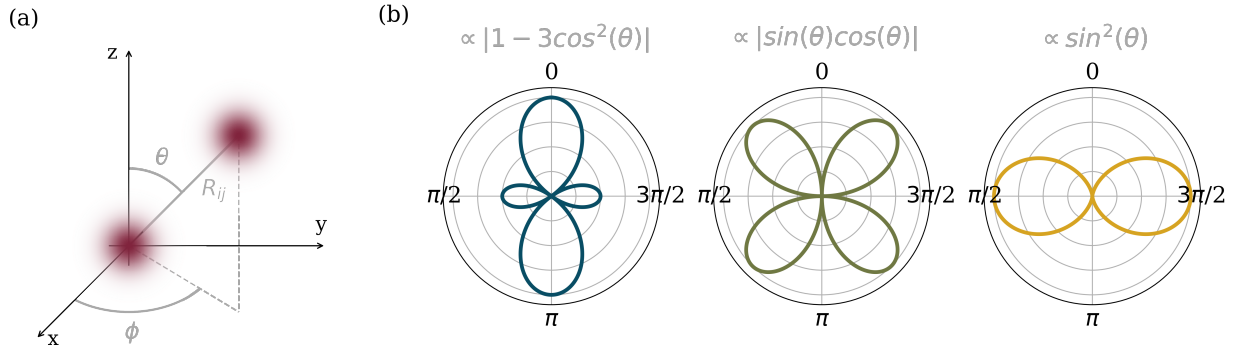


**Fig. 3.3: Angular dependency of dipole interaction operator  $\hat{V}_{dd}$ .** (a) shows the definition of the angles  $\theta$  and  $\phi$  for a two-atom system in the spherical basis. The atoms are indicated in red. (b) The absolute values of the angular dependencies of the dipole interaction operator  $\hat{V}_{dd}$  for different  $|\Delta M| = 0, 1, 2$  are shown in the spherical basis. One finds the angular dependencies  $V_{dd}(\Delta M = 0; \theta) \propto 1 - 3 \cos^2(\theta)$ ,  $V_{dd}(\Delta M = \pm 1; \theta) \propto \sin(\theta) \cos(\theta)$  and  $V_{dd}(\Delta M = \pm 2; \theta) \propto \sin^2(\theta)$ . The interaction is isotropic in  $\phi$  in the spherical basis, up to a global phase.

axis assumed to be parallel to the  $z$ -axis<sup>5</sup>, one finds the dipole operators to be defined as

$$\hat{d}_i^0 = \hat{d}_i^z \quad \text{and} \quad \hat{d}_i^\pm = \mp \frac{1}{\sqrt{2}} \left( \hat{d}_i^x \pm \hat{d}_i^y \right). \quad (3.2)$$

The  $\hat{d}_i^0$  dipole operator conserves the magnetic quantum number  $m_j$ <sup>6</sup> while the  $\hat{d}_i^\pm$  operators change it by  $\pm 1$ . The dipole operators are therefore associated with  $\pi$  and  $\sigma_\pm$  transitions, respectively, as is shown in Figure 2.4. This change to a spherical basis leads to the equivalent formulation of the dipole-dipole interaction operator  $\hat{V}_{dd}$  [102] as

$$\hat{V}_{dd, \text{sph}}^{(i,j)}(\mathbf{R}_{ij}) = \frac{1}{4\pi\epsilon_0 R_{ij}^3} \begin{bmatrix} (1 - 3 \cos^2(\theta)) \left[ \hat{d}_i^0 \hat{d}_j^0 + \frac{1}{2} (\hat{d}_i^+ \hat{d}_j^- + \hat{d}_i^- \hat{d}_j^+) \right] \\ -\frac{3}{\sqrt{2}} \sin(\theta) \cos(\theta) \left[ e^{i\phi} (\hat{d}_i^0 \hat{d}_j^- + \hat{d}_i^- \hat{d}_j^0) - e^{-i\phi} (\hat{d}_i^0 \hat{d}_j^+ + \hat{d}_i^+ \hat{d}_j^0) \right] \\ -\frac{3}{2} \sin^2(\theta) \left[ e^{2i\phi} \hat{d}_i^- \hat{d}_j^- + e^{-2i\phi} \hat{d}_i^+ \hat{d}_j^+ \right] \end{bmatrix}. \quad (3.3)$$

The terms in the upper row result in no change of the magnetic quantum number  $M = m_1 + m_2$  of the two-atom system, while the middle and lower row describe the processes leading to  $\Delta M = \pm 1$  and  $\Delta M = \pm 2$ , respectively. As one can see, the angular dependency of the interaction is determined by the resulting change in  $\Delta M$ , as is also shown in Figure 3.3 (b). The angles  $\theta, \phi$  are defined in Figure 3.3 (a) for clarity.

<sup>5</sup>The angle  $\theta$  is defined as the angle enclosed by the quantisation axis  $\mathbf{q}$  and the interatomic direction vector  $\mathbf{r}_{ij}$ , i.e.  $\theta = \angle(\mathbf{q}, \mathbf{r})$ . Secondly, externally applied electric and magnetic fields are assumed to be orientated along the  $z$ -axis for simplicity, i.e.  $\mathbf{E} = E_0 \epsilon_z$  and  $\mathbf{B} = B_0 \epsilon_z$ .

<sup>6</sup>In the fine-structure basis, the quantum state of an atom is characterised by the state vector  $|n, l, j, m_j\rangle$  where  $m_j$  denotes the orientation of the orbital angular momentum  $j$  with respect to the quantisation axis.

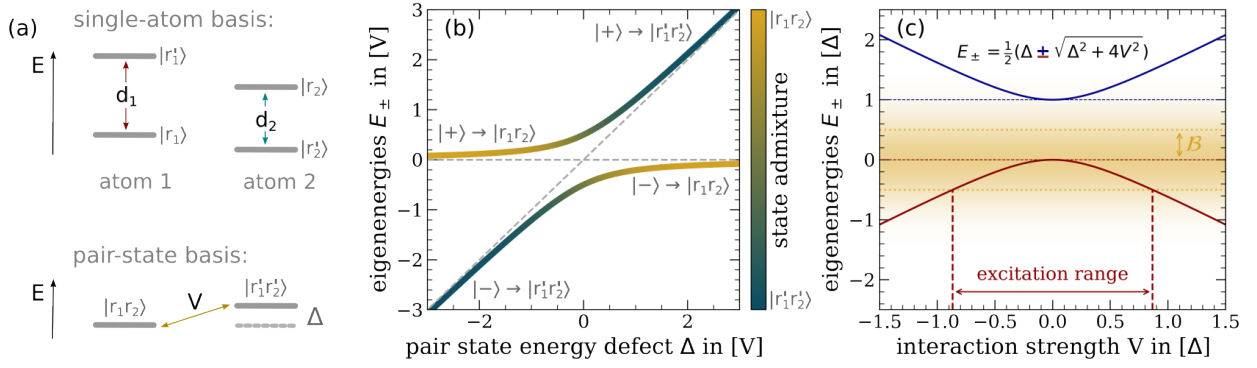


**Fig. 3.4: Coupled pair state system and coupling-induced shift of eigenstates from resonance.** (a) A schematic representation of the states  $|r_i\rangle$  and  $|r'_i\rangle$  with the relevant dipole coupling is shown. The resulting pair-state picture with the energy defect  $\Delta = E(r'_1, r'_2) - E(r_1, r_2)$  and coupling  $V$  is shown at the bottom. In (b), the energy eigenstates of the coupled pair-state system is shown and the relative state admixture indicated. For a coupling strength much weaker than the energy defect, i.e.  $|V| \ll |\Delta|$ , the eigenstates are only weakly admixed and are approximately equal to the bare pair states. These limiting cases are indicated as dashed lines. (c) The energy eigenvalues of the coupled pair-state system are shown for variation of the interaction strength  $V$  relative to the energy defect  $\Delta$ . The coupled pair state can be excited by a field of bandwidth  $B$  only within a certain range where  $|E_{\pm}| \leq B$  such that the coupled pair-state eigenenergy is not shifted out of the excitation range of the field.

Now, let's consider a pair of Rydberg atoms  $|r_1, r_2\rangle^7$  at distance  $R$ , with each atom dipole-coupled to another Rydberg state  $|r'_i\rangle$ . The pair state  $|r_1, r_2\rangle$  then interacts with the pair state  $|r'_1, r'_2\rangle$  via the dipole-dipole interaction  $V(\mathbf{R}) = \langle r'_1, r'_2 | \hat{V}_{dd}(\mathbf{R}) | r_1, r_2 \rangle = C_3/R^3$ . The pair states might be slightly off-resonant, such that an energy defect  $\Delta = E(r'_1, r'_2) - E(r_1, r_2)$  remains. In the pair-state basis  $\{|r_1, r_2\rangle, |r'_1, r'_2\rangle\}$  the dynamics of the two-atom system is then governed by the pair-interaction Hamiltonian<sup>8</sup>

$$\mathcal{H}_{dd}^{pair} = \begin{pmatrix} 0 & V(\mathbf{R}) \\ V(\mathbf{R}) & \Delta \end{pmatrix} \quad (3.4)$$

which results in an oscillation back and forth between the two pair-states for sufficiently strong coupling  $V(\mathbf{R})$  and small energy defects  $\Delta$ . The eigenenergies of the Hamiltonian are found to be  $E_{\pm} = (\Delta \pm \sqrt{\Delta^2 + 4V(\mathbf{R})^2})/2$  and the corresponding eigenstates are given by

$$|\epsilon_{\pm}\rangle = \frac{1}{\sqrt{\alpha_{\pm}^2 + 1}} (\alpha_{\pm} |r_1, r_2\rangle + |r'_1, r'_2\rangle)$$

with  $\alpha_{\pm} = -(\Delta \pm \sqrt{\Delta^2 + 4V(\mathbf{R})^2})/2V(\mathbf{R})$ . For  $\Delta = 0$  the eigenstates  $|\epsilon_{\pm}\rangle$  consist of a symmetric superposition of  $|r_1, r_2\rangle$  and  $|r'_1, r'_2\rangle$  up to a factor of  $\pm 1$ .

This Hamiltonian is similar to the two-level atom-light Hamiltonian discussed in Section 2.1.1, which gave rise to the dressed state picture with the resulting eigenstates shifted in energy

<sup>7</sup>In the following, we will use  $|r\rangle$  as a shorthand notation for the fine-structure state  $|n, l, j, m_j\rangle$ .

<sup>8</sup>In this chapter we have set  $\hbar = 1$  for simplicity.

around resonance for strong coupling fields  $\Omega$ . In the case of interacting pair states, the coupling strength between the near-resonant pair states is given by the dipole-dipole interaction  $V(\mathbf{R})$ , and the detuning from resonance by the energy difference  $\Delta$  between the pair states. In analogy to the dressed atom-light system, one also has to consider the eigenstates of the coupled pair-state system in the near-resonant and off-resonant limit cases.

For large energy defects compared to the pair-state coupling, i.e.  $|\Delta| \gg V(\mathbf{R})$ , the eigenstates are given by the bare pair states  $|r_1, r_2\rangle$  and  $|r'_1, r'_2\rangle$  with negligible state admixture, and the eigenenergies  $E_{\pm}$  correspond to the respective pair state energies. However, the situation changes drastically for the case of strong coupling relative to the pair-state energy defect, i.e. for  $V(\mathbf{R}) \gg |\Delta|$ . In this regime one finds strong state admixture, i.e. the Rydberg atoms oscillate back and forth between the pairs  $|r_1, r_2\rangle \leftrightarrow |r'_1, r'_2\rangle$ , and the eigenenergies of the coupled system change relative to the uncoupled case.

The dipole-dipole interaction therefore couples two Rydberg pair states  $|r_1, r_2\rangle$  and  $|r'_1, r'_2\rangle$  if  $|r_1\rangle \leftrightarrow |r'_1\rangle$  and  $|r_2\rangle \leftrightarrow |r'_2\rangle$  are each dipole-coupled. Depending on the energy defect  $\Delta$  and the coupling strength  $V(\mathbf{R})$  this may lead to the formation of dressed states with shifted eigenenergies relative to the initial bare state  $|r_1, r_2\rangle$ . As a consequence, resonant excitation of a second Rydberg state  $|r_2\rangle$  near  $|r_1\rangle$  may not be possible on the bare state resonance frequency if the pair-state interaction shifts the pair-state eigenenergies out of resonance with the excitation laser – an effect known as Rydberg blockade [103] and shown in Figure 3.4 (c).

Various interaction-induced effects occurring in the strongly coupled system have been observed experimentally [103, 104], e.g. the fast oscillations between the pair states  $|r_1, r_2\rangle$  and  $|r'_1, r'_2\rangle$  [102]. The general angular dependency of the dipole-dipole interaction has been shown [105] and the typical angular dependency  $\propto (1 - 3 \cos^2(\theta))$  for an isolated transition with  $\Delta M = 0$  has been demonstrated [102].

One can now apply the tool developed above to study the resulting interactions between Rydberg atoms. The states  $|r_1\rangle$  and  $|r_2\rangle$  might be directly dipole coupled such that  $|r'_1, r'_2\rangle = |r_2, r_1\rangle$  which results in a vanishing energy defect  $\Delta = 0$ . Such degenerate pair states with vanishing energy defect are said to be on Förster resonance. This resonant dipole-interaction induced coupling leads to long-range scaling of the interaction strength  $\propto 1/R^3$  and induces oscillations between the states  $|r_1, r_2\rangle \leftrightarrow |r_2, r_1\rangle$  with frequency  $V(\mathbf{R})$ . If, however, the atoms are coupled by  $\hat{V}_{dd}$  in a second-order process<sup>9</sup>, e.g. because they initially occupy the same Rydberg state, then one can find different regimes with  $\propto 1/R^3$  or  $\propto 1/R^6$  scalings in distance. Since the experiment reported in this thesis excites only to a single Rydberg state, these second-order interaction processes are dominant and we will proceed by having a closer look at those.

### 3.2.2 SECOND-ORDER INTERACTION PROCESSES

For two atoms with an orbital angular momentum difference  $\Delta l = |l_1 - l_2| \in \{0, 2\}$  the interaction mediated by  $\hat{V}_{dd}$  is of second order, e.g. for a pair of atoms initially in the same Rydberg states  $|r_1, r_2\rangle = |r, r\rangle$ . This means that the interaction process includes an intermediate, auxiliary dipole-coupled pair state  $|\tilde{r}_1, \tilde{r}_2\rangle$  as shown schematically in Figure 3.5 (a). The two-atom

<sup>9</sup>Higher-order electric coupling like e.g. dipole-quadrupole, or magnetic couplings between the two atoms are usually orders of magnitude weaker than a second-order dipole-dipole coupling process [106].

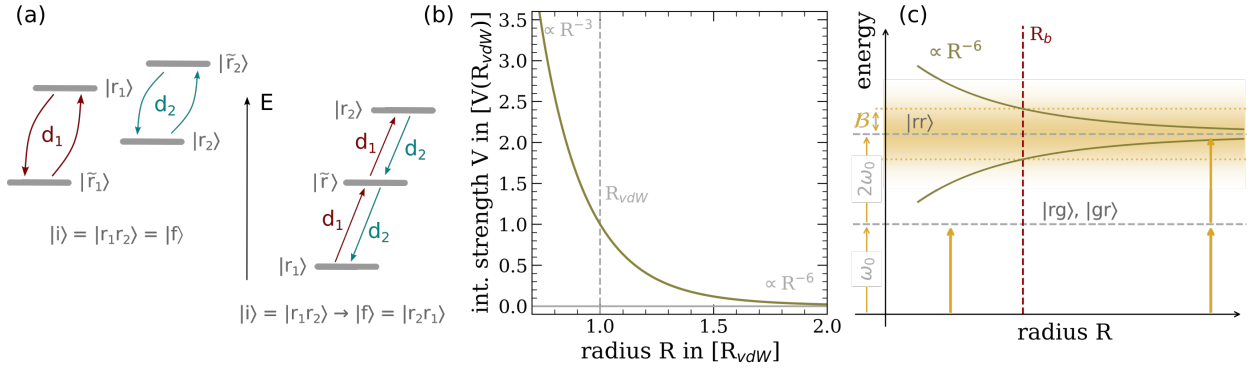


**Fig. 3.5: Second-order interaction in the van der Waals regime and Rydberg blockade effect.** The second order interaction process is shown schematically for the case of no state hopping, i.e. where  $|i\rangle = |f\rangle$ , in the top left and for the case of state hopping in the bottom right of panel (a). Both processes ensure that the state energy of initial and final state, i.e.  $E(|i\rangle)$  and  $E(|f\rangle)$ , are identical. The intermediate state may have an energy defect  $\Delta$ , though. Crossover of the second-order interaction scaling in distance from  $\propto R^{-3}$  to  $\propto R^{-6}$  for  $R \ll R_{vdW}$  and  $R \gg R_{vdW}$  respectively, is shown in (b). The resulting effect of Rydberg blockade is shown for the van der Waals regime in (c), but occurs equally in the other regimes. Coupling of the  $|r\rangle$  and  $|r'\rangle$  states leads to a distance-dependent shift of the  $|r_1, r_2\rangle$  pair state energy. For interatomic distances  $R < R_b$  below the blockade radius, the state energy is shifted out of the range covered by the excitation bandwidth  $\mathcal{B}$  associated with the transition. This prevents an excitation of an atom into the Rydberg state when being in close spatial proximity to another Rydberg atom.

system therefore undergoes the process<sup>10</sup>

$$|i\rangle = |r_1, r_2\rangle \xrightarrow{\hat{V}_{dd}} |\tilde{r}_1, \tilde{r}_2\rangle \xrightarrow{\hat{V}_{dd}} |r'_1, r'_2\rangle = |f\rangle. \quad (3.5)$$

The single-atom transitions  $|r_i\rangle \xrightarrow{d_i} |\tilde{r}_i\rangle \xrightarrow{d'_i} |r'_i\rangle$  occurring in this process all have to be dipole-allowed with  $d_i, d'_i$  representing the respective dipole transition matrix elements. When considering the resulting scaling of the interaction with atomic distance  $R$  one finds two different power law scalings for different distance regimes, separated by the van der Waals radius  $R_{vdW} = \sqrt[3]{|C_3/\Delta|}$  where the interaction-induced level shift  $V(\mathbf{R}) = C_3/R^3$  equals the pair state energy defect  $\Delta(r'_1, r'_2)$ . For shorter distances  $R \ll R_{vdW}$  the long-range interaction  $\propto V(\mathbf{R}) = C_3/R^3$  scales with  $n_*^4$  while  $R \gg R_{vdW}$  implies short-range interactions  $\propto C_6/R^6$  where  $C_6$  scales<sup>11</sup> with  $n_*^{11}$  [107].

Additionally, the interactions leads to the aforementioned Rydberg blockade effect – both in the van der Waals and the dipole-coupled regime, where the interactions scale as  $\propto R^{-n}$  with  $n = 6$  and  $n = 3$ , respectively. While the two atoms are further apart than the blockade radius

<sup>10</sup>For the following considerations the initial and final states do not necessarily have to be identical but could also be interchanged. I.e. for  $|i\rangle = |r_1, r_2\rangle$  one always has  $|f\rangle = |i\rangle$  and, if dipole coupled, also  $|f\rangle = |r_2, r_1\rangle$  as possible final states.

<sup>11</sup>The scalings of  $C_3$  and  $C_6$  with effective principal quantum number  $n_*$  can be estimated very easily. The dipole matrix elements  $d_{1,2}$  between two nearby Rydberg states grow as  $n_*^2$  while the corresponding energy defect scales as  $n_*^{-3}$ . Therefore,  $C_3 \propto d_1 d_2 \propto n_*^4$  and  $C_6 \propto (d_1 d'_1 d_2 d'_2)/\Delta \propto n_*^{11}$  [84].

$R_b = \sqrt[n]{C_n/\mathcal{B}}$ , the coupled pair-state eigenenergies lie within the range that can be excited by the coupling field of bandwidth  $\mathcal{B}$ <sup>12</sup>. Hence, both atoms can be excited into the Rydberg state  $|rr\rangle$ . As the atoms move closer, the spatial dependency of  $V(\mathbf{R}) \propto R^{-n}$  eventually shifts the pair state energy out of resonance with the excitation field, effectively inhibiting the excitation of a second Rydberg atom within the radius  $R \leq R_b$ . Only the states  $|rg\rangle, |gr\rangle$  will be populated in this scenario.

For a given initial pair state  $|r_1, r_2\rangle$  there is usually a number of intermediate pair states which are somewhere near resonance with the initial pair state, but with a non-vanishing energy defect  $\Delta$ . Therefore, many intermediate pair states will contribute to the dynamics of the interaction which is accounted for in the second-order interaction Hamiltonian by summing over all dipole-coupled intermediate pair states  $\{|\tilde{r}_1, \tilde{r}_2\rangle\}$  [106]

$$\hat{H}_{so}(\mathbf{R}) = \sum_{\{|\tilde{r}_1, \tilde{r}_2\rangle\}} \frac{\hat{V}_{dd}(\mathbf{R}) |\tilde{r}_1, \tilde{r}_2\rangle \langle \tilde{r}_1, \tilde{r}_2| \hat{V}_{dd}(\mathbf{R})}{\Delta(\tilde{r}_1, \tilde{r}_2)}. \quad (3.6)$$

The level shifts induced by this second-order interaction also lead to the Rydberg blockade effect [108, 109], see also Figure 3.5, and the resulting interaction has been shown to be anisotropic in general [106, 109, 110]. However, even though a direct evaluation of  $\hat{H}_{so}(\mathbf{R})$  is possible, it does not provide much intuition on the behaviour of the anisotropy. This spatial anisotropy can be understood when considering the angular momenta of the most significantly contributing intermediate pair states and the angular dependence of the dipole transitions involved in the process, as will be shown in the next section.

### 3.2.3 STRUCTURE OF THE $C_6$ INTERACTION COEFFICIENT

When being in the van der Waals regime with  $R \gg R_{vdW}$ , the interaction between two Rydberg atoms in the same state scales as  $C_6/R^6 \propto n_*^{11}$ . However, when calculating the interactions for two Rydberg atoms with different initial Rydberg states  $|n_1, l_1, j_1, m_{j_1}\rangle$  and  $|n_2, l_2, j_2, m_{j_2}\rangle$ , one finds that the 2D maps with varying  $(n_1, n_2)$  show very clear structures. This is shown in Figure 3.6 for the interaction of two P<sub>J</sub>-states in rubidium with different principal quantum numbers  $n_i$ . The angular dependency of the  $C_6$  coefficients has been discussed from a technical perspective in [106] for  $n_1 = n_2$ , based on a study of the dominant angular momentum channels. This section uses a similar angular momentum channel approach in order to provide an intuitive understanding of the angular dependency of the  $C_6$  coefficients but allowing for  $n_1 \neq n_2$ , and to explain the structure formation observed in [111]. The resulting understanding of the  $C_6$  interaction coefficients is then used to discuss interesting pairs of pair states for the generation of an on-demand effective interaction between two photons in Section 3.2.5.

For the readers interested in the details of the structures found in the interaction map, we present an extended analysis of the different contributions leading to the specific features in the interactions. The main results of this section are summarised in Subsection 3.2.3.4.

<sup>12</sup>For simplicity, one usually sets the bandwidth  $\mathcal{B}$  equal to the effective Rabi frequency  $\Omega_{\text{eff}}$  of the transition. However, significant line broadening and other effects may broaden the bandwidth beyond the limit given by  $\Omega_{\text{eff}}$ .

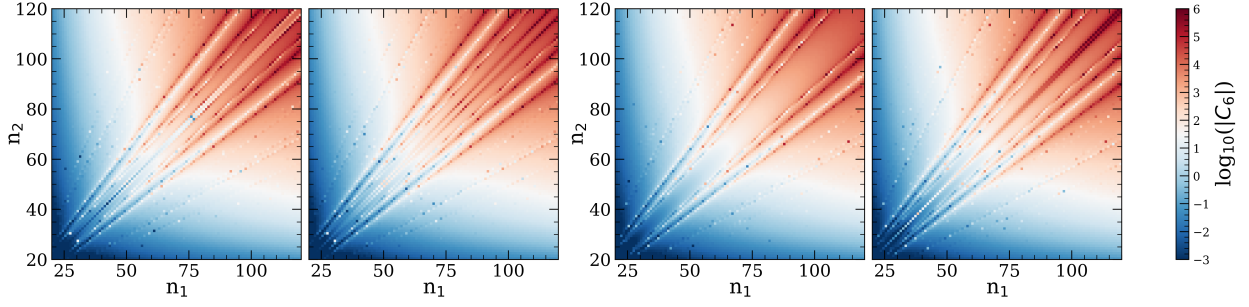


**Fig. 3.6: Structures in the  $C_6$  coefficients of  $P_J$ -states in rubidium.** The absolute values of the total interaction coefficient  $C_6$  for the interaction of two Rydberg atoms  $|r_1, r_2\rangle$  with  $|r_i\rangle = |n_i P_J, m_j = +J\rangle$ , i.e. with the same angular momentum quantum numbers  $l, j, m_j$  but varying principal quantum numbers  $n_i$ , is plotted.  $J = 1/2$  is shown in the left pair of plots and  $J = 3/2$  on the right, both at the angles  $\theta = 0, \pi/2$  (left, right subplot per pair). The colour-bar applies to all plots. One can clearly see a strong structuring of the  $C_6$  coefficients in form of lines of strong/weak interactions apparent in the log-plot. The angular dependence of  $|C_6|$  is also apparent. For identical angular quantum numbers the  $C_6$  coefficients are symmetric with respect to an exchange of  $n_1$  and  $n_2$ , as can also be seen in the symmetry of the plots with respect to the axis defined by  $n_1 = n_2$ .

When having a closer look at a single second-order interaction process in (3.5)<sup>13</sup>

$$|i\rangle = |r_1, r_2\rangle \xrightarrow{\hat{d}_1 \hat{d}_2} |\tilde{r}_1, \tilde{r}_2\rangle \xrightarrow{\hat{d}'_1 \hat{d}'_2} |r'_1, r'_2\rangle = |f\rangle, \quad (3.7)$$

one finds that the overall interaction strength is determined by the dipole matrix elements

$$d_i^\alpha = \langle n_i, l_i, j_i, m_{j,i} | \hat{d}_i^\alpha | n'_i, l'_i, j'_i, m'_{j,i} \rangle \quad (3.8)$$

of the specific transitions in equation (3.7).  $\alpha = 0, \pm 1$  relates to the electric field polarisations driving  $\pi, \sigma_\pm$  transitions, respectively. Further analysis of the dipole matrix element of an atomic transition reveals that it can be split into a radial and an angular part by use of the Wigner-Eckart theorem [112]. When suppressing the atom-index  $i$ , a dipole matrix element is given as

$$d^\alpha = \langle n', l', j', m'_{j'} | \hat{d}^\alpha | n, l, j, m_j \rangle = \mathcal{R}(n, l, j; n', l', j') \mathcal{D}^\alpha(j, m_j; j', m'_{j'}) \quad (3.9)$$

with the radial and angular parts [98, 106, 111]

$$\mathcal{R}(n, l; n', l') = (-1)^{l'} \sqrt{(2l+1)(2l'+1)} \begin{pmatrix} l & 1 & l' \\ 0 & 0 & 0 \end{pmatrix} \int_0^\infty R_{nl}(r) e r R_{n'l'}(r) r^2 dr \quad (3.10)$$

and

$$\begin{aligned} \mathcal{D}^\alpha(l, j, m_j; l', j', m'_{j'}) &= (-1)^{l+j+j'+s-m_j+1} \sqrt{(2j+1)(2j'+1)} \\ &\times \begin{Bmatrix} j & 1 & j' \\ l' & s & l \end{Bmatrix} \begin{pmatrix} j & 1 & j' \\ -m_j & -\alpha & m'_{j'} \end{pmatrix}. \end{aligned} \quad (3.11)$$

<sup>13</sup>The transition type  $\alpha = m'_j - m_j \in \{0, \pm 1\}$  corresponds to the  $\pi, \sigma_\pm$  transition driven by the field, and has been absorbed in  $d_i, d'_i$  for simplicity.

The above equations use  $(:::)$  to notate the Wigner-3j symbol and  $\{:::\}$  for the Wigner-6j symbol, while  $s$  denotes the electron spin.  $R_{nl}(r)$  denotes the radial wavefunction of the respective state and depends only on  $n$  and  $l$ <sup>14</sup>. The coupling strength between the states  $|r\rangle, |r'\rangle$  is mostly determined by the radial coupling strength  $\mathcal{R}$  while the angular coupling is absorbed in  $\mathcal{D}^\alpha$ .

Since the overall process described in equation (3.7) is of second order, the energy defect  $\Delta$  also plays a decisive role in shaping the resulting strength of the interaction. The interplay of these three ingredients - radial coupling strength, angular dependency, and energy defect – and the resulting structure in the  $C_6$  coefficients – are discussed in the following.

### 3.2.3.1 ANGULAR DEPENDENCY AND ANGULAR MOMENTUM CHANNELS

The angular dependency of the total second-order process described by equation (3.6) can be separated into several angular momentum channels characterised by the  $(l, j, m_j)$  quantum numbers of the six atomic states involved in the process, i.e. of all three pair states  $|i\rangle, |interm.\rangle, |f\rangle$ . Each of these angular momentum channels is characterised by its own angular dependency. All second-order processes with the same angular momentum pathway  $|l_1 j_1, l_2 j_2\rangle \rightarrow |\tilde{l}_1 \tilde{j}_1, \tilde{l}_2 \tilde{j}_2\rangle \rightarrow |l'_1 j'_1, l'_2 j'_2\rangle$  are combined into a single channel coefficient  $C_6^{(\tilde{l}_1 \tilde{j}_1, \tilde{l}_2 \tilde{j}_2)}$ , such that one finds the re-arranged second order interaction Hamiltonian to be given by

$$\begin{aligned} \hat{H}_{so}(R, \theta, \phi) &= \frac{1}{R^6} \sum_{\{\tilde{l}_i \tilde{j}_i\}} \left( \sum_{\{\tilde{n}_i\}} \frac{\mathcal{R}_1 \mathcal{R}_2 \mathcal{R}'_1 \mathcal{R}'_2}{\Delta(\tilde{n}_i, \tilde{l}_i, \tilde{j}_i)} \right) \hat{\mathcal{M}}(\tilde{l}_i, \tilde{j}_i) \\ &= \sum_{\{\tilde{l}_i \tilde{j}_i\}} \frac{C_6^{(\tilde{l}_i \tilde{j}_i)}}{R^6} \hat{\mathcal{M}}(\tilde{l}_i, \tilde{j}_i). \end{aligned} \quad (3.12)$$

The index  $i$  is used as shorthand notation to indicate a dependence of the respective value from both atoms, i.e.  $l_i = l_1 l_2$ . The abbreviations  $\mathcal{R}_1^{(l)}$  and  $\mathcal{R}_2^{(l)}$  have been used for the radial coupling strengths, where the prime indicates the  $|interm.\rangle \rightarrow |f\rangle$  process. The energy defect  $\Delta(\tilde{n}_i, \tilde{l}_i, \tilde{j}_i)$  is shorthand for

$$\Delta(n_i, l_i, j_i; \tilde{n}_i, \tilde{l}_i, \tilde{j}_i) = E(\tilde{n}_i, \tilde{l}_i, \tilde{j}_i) - E(n_i, l_i, j_i).$$

All angular dependency has been absorbed in the operator  $\hat{\mathcal{M}}(\tilde{l}_i, \tilde{j}_i)$ , which will be analysed in the next paragraph. This re-arrangement of the sums means that we can now study the angular dependency of the different angular channels, weighted by their respective channel's interaction strength  $C_6^{(\tilde{l}_i \tilde{j}_i)}$ . For example, in the case of  $|i\rangle = |f\rangle = |n_1 P_{1/2}, n_2 P_{1/2}\rangle$  one finds four angular momentum channels with

$$|interm.\rangle \in \{|\tilde{n}_1 S_{1/2}, \tilde{n}_2 S_{1/2}\rangle, |\tilde{n}_1 S_{1/2}, \tilde{n}_2 D_{3/2}\rangle, |\tilde{n}_1 D_{3/2}, \tilde{n}_2 S_{1/2}\rangle, |\tilde{n}_1 D_{3/2}, \tilde{n}_2 D_{3/2}\rangle\}.$$

The resulting coefficients  $C_6^{(\tilde{l}_i \tilde{j}_i)}$  constitute a sum over all possible intermediate state principal quantum numbers  $(\tilde{n}_1 \tilde{n}_2)$  and can easily be computed with the functions available in Python

<sup>14</sup>The radial wavefunction is completely characterised by the quantum numbers  $n$  and  $l$ , while the relative phase of the wavefunction at  $(\theta, \phi)$  depends on the angular quantum numbers.

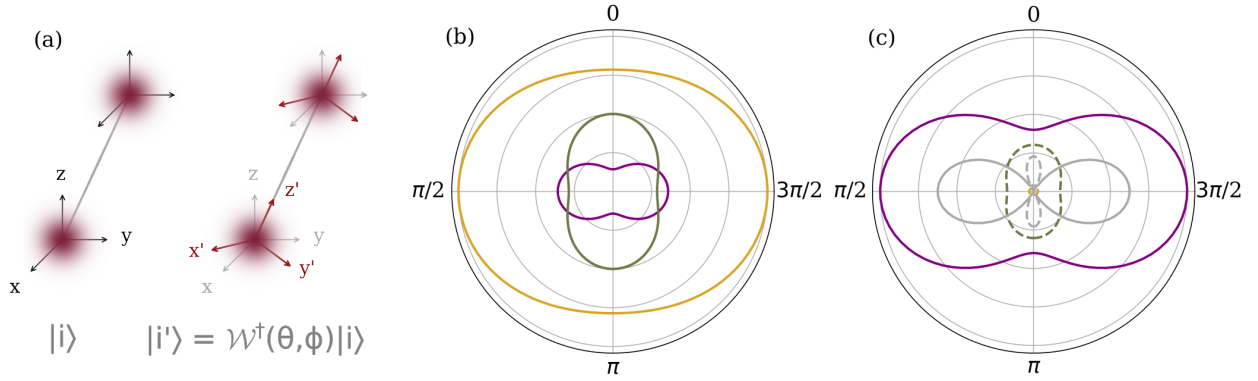


**Fig. 3.7: Basis rotation and angular dependency of  $|n_1P_{1/2}, n_2P_{1/2}\rangle$  angular momentum channels.** (a) shows the initial (unprimed, left) and rotated (primed, right) basis before and after rotation by  $\mathcal{W}^\dagger(\theta, \phi)$ . The dipole interaction takes its simplest form in the primed coordinate frame where the  $z'$ -axis and the internuclear axis align. The angular dependency of the four channels for the interaction of  $|n_1P_{1/2}, n_2P_{1/2}\rangle$  with  $m_{j1} = m_{j2} = +1/2$  is shown in (b). The intermediate states correspond to colour as follows:  $|\tilde{n}_1S_{1/2}, \tilde{n}_2S_{1/2}\rangle$  (purple),  $|\tilde{n}_1S_{1/2}, \tilde{n}_2D_{3/2}\rangle$  (green),  $|\tilde{n}_1D_{3/2}, \tilde{n}_2S_{1/2}\rangle$  (blue, identical to green),  $|\tilde{n}_1D_{3/2}, \tilde{n}_2D_{3/2}\rangle$  (yellow). The angle  $\theta$  is varied in range  $[0, 2\pi]$  while  $\phi = 0$  in plots (b) and (c). In (c), the angular dependency of the  $|110P_{1/2}, 110P_{1/2}, m_{j1} = m_{j2} = 1/2\rangle$  state of rubidium is shown. Dashed lines indicate negative values. The respective interaction coefficients  $C_6^{(\tilde{l}_i \tilde{j}_i)}$  are: 230.9 THz  $\mu\text{m}^6$  (purple), -49.9 THz  $\mu\text{m}^6$  (blue, green), and -2.4 THz  $\mu\text{m}^6$  (yellow), with the colours of the angular channels as in (b). The gray colour is the resulting angular dependency of  $|C_6|$  as  $\theta$  is varied. Note that the small lobes stretching towards  $\theta = 0, \pi$  have negative sign such that there exist angles  $\theta_0$  where  $C_6(\theta_0, \phi) = 0$ .

libraries such as ARC [98]. Structures of these coefficients, and their dependence on the radial coupling strength and energy defect, are discussed in the following two Subsections 3.2.3.2 and 3.2.3.3.

To get an understanding of the angular dependency of  $\hat{\mathcal{M}}$ , one has to take another look at the second-order process described by  $\hat{H}_{sq}(\mathbf{R})$ . It inherits the angular dependency of the interaction from the dipole-dipole interaction  $\hat{V}_{dd}$ , which shows a complex pattern for a general set of angles  $(\theta, \phi)$ . The effective action of  $\hat{V}_{dd}$  becomes clearer when rotating into the frame where the internuclear axis and the quantisation axis  $\mathbf{q}$  align in parallel. In this orientation, the dipole interaction term takes its simplest form since  $M = m_{j1} + m_{j2}$  is conserved at this angle, so that all terms in  $\hat{V}_{dd}$  with  $\Delta M > 0$  vanish.

A rotation of the atomic state  $|n, l, j, m_j\rangle$  between two coordinate systems  $X$  and  $\bar{X}$  is performed via the Wigner (uppercase) D-matrices<sup>15</sup>  $\hat{\mathcal{W}}(\theta, \phi)$  [106] such that  $|\bar{i}\rangle = \hat{\mathcal{W}}^\dagger(\theta, \phi)|i\rangle$ . Note that the Wigner D-matrices perform a rotation of the total orbital angular momentum basis and depend only on the angular quantum numbers  $j, m_j$ , and  $\bar{m}_j$ <sup>16</sup>. Having performed the basis ro-

<sup>15</sup>Note that the Wigner (uppercase) D-matrices allow for an arbitrary 3D rotation about the angles  $(\theta, \phi)$ . If the interaction were fixed in the  $xz$ -plane, then one would use the Wigner (lowercase) d-matrices which allow for rotation by a single degree of freedom  $\theta$  [99].

<sup>16</sup>The representation of the projection of the total orbital angular momentum  $m_j$  changes as we change the basis with respect to which we express the state. However, this transformation does not change the values  $n, l, j$ .

tation, one can calculate the effect of the second-order dipole interactions in its simplest form for  $\theta = 0$  where  $\Delta M > 0$  terms vanish, and then compute the projection of the resulting states onto the rotated final state  $\langle f | \hat{\mathcal{W}}(\theta, \phi) \rangle$ . Therefore,

$$\begin{aligned} C_6(\theta, \phi) &= \langle f | \hat{\mathcal{W}}(\theta, \phi) \hat{H}(R, \theta = 0, \phi) \hat{\mathcal{W}}^\dagger(\theta, \phi) | i \rangle \\ &= \sum_{\{(\tilde{l}_i, \tilde{j}_i)\}} \frac{C_6^{(\tilde{l}_i, \tilde{j}_i)}}{R^6} \langle f | \hat{\mathcal{W}}(\theta, \phi) \hat{D}(\tilde{l}_i, \tilde{j}_i) \hat{\mathcal{W}}^\dagger(\theta, \phi) | i \rangle \end{aligned} \quad (3.13)$$

$\hat{D}$  is independent of  $(\theta, \phi)$ , and is determined only by the angular momentum pathways  $m_j$  that are allowed by the dipole selection rules for a given set of intermediate state angular momentum quantum numbers  $(\tilde{l}_i, \tilde{j}_i)$ . The elements of  $\hat{D}$  are defined via the angular parts of the dipole transitions

$$\begin{aligned} &\langle l'_1 j'_1 m'_{j1}, l'_2 j'_2 m'_{j2} | \hat{D}(\tilde{l}_i, \tilde{j}_i) | l_1 j_1 m_{j1}, l_2 j_2 m_{j2} \rangle \\ &= \sum_{\{(\tilde{m}_{j1}, \tilde{m}_{j2})\}} \left( \sum_{\alpha \in \{0, \pm 1\}} C(\alpha) \mathcal{D}^\alpha(l_1 j_1 m_{j1}, \tilde{l}_1 \tilde{j}_1 \tilde{m}_{j1}) \mathcal{D}^{-\alpha}(l_2 j_2 m_{j2}, \tilde{l}_2 \tilde{j}_2 \tilde{m}_{j2}) \right) \\ &\quad \left( \sum_{\alpha' \in \{0, \pm 1\}} C(\alpha') \mathcal{D}^{\alpha'}(\tilde{l}_1 \tilde{j}_1 \tilde{m}_{j1}, l'_1 j'_1 m'_{j1}) \mathcal{D}^{-\alpha'}(\tilde{l}_2 \tilde{j}_2 \tilde{m}_{j2}, l'_2 j'_2 m'_{j2}) \right) \end{aligned} \quad (3.14)$$

with the different polarisation coupling weights of  $\hat{V}_{dd}(\theta = 0)$  implemented by

$$C(\beta) = \begin{cases} -2, & \beta = 0 \\ -1, & \beta = \pm 1 \end{cases}$$

as given in equation (3.3).

The angular dependency therefore boils down to the overlap of the rotated final state with the rotated initial state subject to the angular momentum channel's allowed  $m_j$  interaction pathways. These interaction pathways may differ between the angular momentum channels since e.g. the pathway  $|m_j = \pm 1/2\rangle \rightarrow |m_j = \pm 3/2\rangle \rightarrow |m_j = \pm 1/2\rangle$  is possible for an intermediate  $|D\rangle$  state, but not for an  $|S\rangle$  state. Figure 3.7 (a) shows the basis rotation protocol, and (b) the angular dependencies of the angular channels for  $|n_1 P_{1/2}, n_2 P_{1/2}\rangle$  states. An example for the resulting angular dependency of  $|110P_{1/2}, 110P_{1/2}, m_{j1} = m_{j2} = 1/2\rangle$  in rubidium is shown in (c).

### 3.2.3.2 RADIAL COUPLING STRENGTH

The order of magnitude of the radial coupling strength  $\mathcal{R}$  is determined by the integral in equation (3.10), which depends only on the principal and orbital momentum quantum numbers  $n$  and  $l$ . Generally, the radial overlap of two Rydberg states grows with increasing  $n$ ,  $n'$  and decreasing  $|\Delta n| = |n' - n|$ . The coupling strength of two nearby Rydberg states scales as  $n_*^2$  for  $l \ll n$  [84].

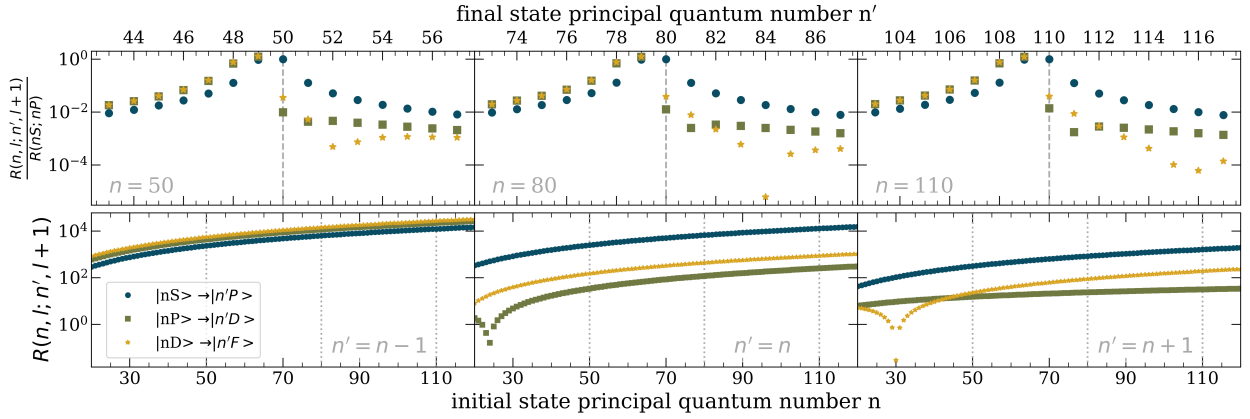


**Fig. 3.8: Radial coupling strength for low- $l$  dipole transitions in rubidium.** The upper row shows the value of the radial coupling strength for single-atom  $|nL\rangle \rightarrow |n'(L+1)\rangle$  transitions relative to the  $|nS\rangle \rightarrow |nP\rangle$  coupling strength in rubidium at three different values of  $n = 50, 80, 110$ . The value of the radial overlap integral is weighted towards  $\Delta n = n' - n < 0$ , rendering these transitions more likely than those with  $\Delta n \geq 0$ . In the lower row, the value of the radial overlap integral  $R(n, l; n', l')$  is shown for different  $\Delta n = 0, \pm 1$ . For  $\Delta n < 0$ , all channels follow the well-known  $n_*^2$  scaling law. However, for  $\Delta n = 0$  one can see a destructive resonance in the overlap integral value for the  $|nP\rangle \rightarrow |nD\rangle$  channel, and for  $\Delta n = +1$  in the  $|nD\rangle \rightarrow |nF\rangle$  channel. For higher  $\Delta n > 1$ , the destructive resonance in the coupling strength of the  $|nD\rangle \rightarrow |nF\rangle$  channel in rubidium moves to higher  $n$ . All values were calculated with ARC [98], which utilises the Numerov method for computation of the radial overlap integrals.

However, the situation is not as simple as that as Figure 3.8 shows. The upper row shows the relative radial overlap integral strength for  $|nL\rangle \rightarrow |n'(L+1)\rangle$  transitions with  $L \in \{S, P, D\}$ , and one can see that the overlap integral is weighted towards  $\Delta n < 0$  for all  $L$ . This behaviour can be understood from the properties of the radial wavefunction  $R_{nl}(r)$ . Each radial wavefunction has  $n - l - 1$  nodes with an associated sign change along  $r$  at each node. For positive  $\Delta n \geq 0$ , the resulting change in the sign and node structure of the radial wavefunction  $R_{n'l'}$  leads to destructive overlap of the two radial wavefunctions, and a lower integral value. Such transitions with  $\Delta n > 0$  are therefore weaker coupled than transitions with  $\Delta n < 0$ . The same effect is also visible in the lower row of Figure 3.8 where the reduced value of the radial overlap integral for  $\Delta n \geq 0$  can be seen in the destructive resonances of the data traces for  $L > 0$ . As a consequence, transitions with  $\Delta n < 0$  and small  $\Delta n \sim \mathcal{O}(1)$  generally have the strongest radial coupling strengths. The general scaling of the radial coupling strength, however, follows the well-known  $n_*^2$  scaling – but attention has to be paid to the reduced coupling strengths for  $\Delta n \geq 0$ .

Since the whole second-order process includes a total of four transitions, the interaction resulting from a given channel is strongest when all four dipole matrix elements, and therefore all radial coupling strengths  $\mathcal{R}_i^{(l)}$ , are large. The strongest interactions are hence found at pairs of transitions between states with high  $n$  and comparably small changes in principal quantum number  $\Delta n \sim \mathcal{O}(1)$ .

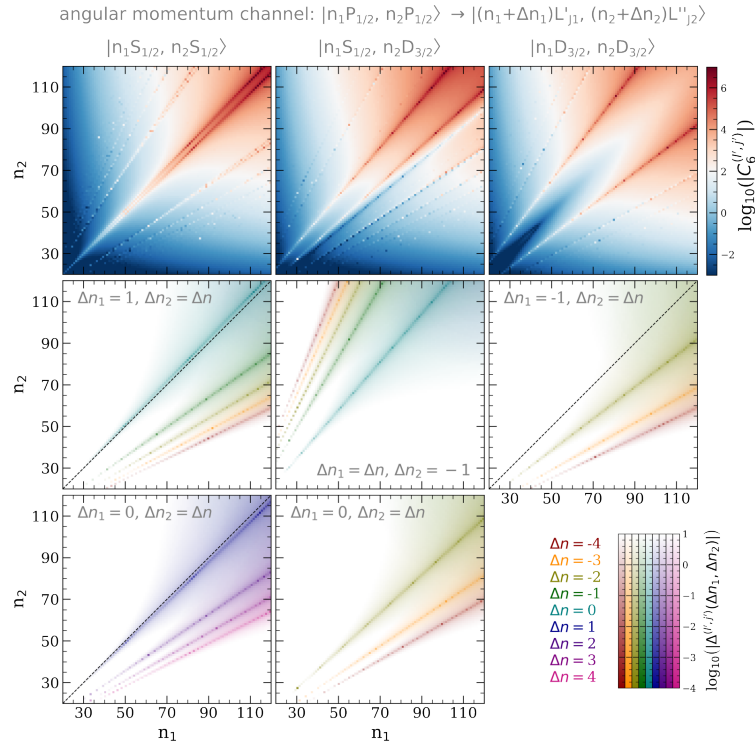


**Fig. 3.9: Förster resonances of the angular momentum channels coupled to  $|n_1P_{1/2}, n_2P_{1/2}\rangle$  in rubidium.** The different angular momentum channels coupled to the  $|i\rangle = |f\rangle = |n_1P_{1/2}, n_2P_{1/2}\rangle$  have their own respective Förster resonance structure, as shown in the three columns on the left. Different colours indicate the order  $\Delta n$  of the resonance, which is important with respect to the radial coupling strength of the transitions. To complete the Förster resonance structure, one has to consider the permuted case of  $|\tilde{r}_2, \tilde{r}_1\rangle$  which occurs equally and corresponds to a transposition of the plots at the  $n_1 = n_2$  axis. In the non-symmetric channel coupling via the  $|\tilde{n}_1S_{1/2}, \tilde{n}_2D_{3/2}\rangle$  states one can see a line of very weak interactions between the  $\Delta n_1 = 0, \Delta n_2 = -2, -3$  resonances. This occurs because the coefficient  $|C_6^{(\tilde{i}, \tilde{j}; i)}|$  changes sign across this line, which is not distinguishable in this absolute value plot. Absolute values of energy defects  $\Delta$  and interaction strengths are given in GHz, and the legend in log space.

### 3.2.3.3 ENERGY DEFECT

The strongest pair interactions occur on Förster resonance where two pair states  $|r_1, r_2\rangle$  and  $|r'_1, r'_2\rangle$  are (nearly) degenerate. This well-known effect has been used to identify strong Rydberg self-interactions for the case where  $|r_1\rangle = |r_2\rangle = |r\rangle$  [106]. However, Förster resonances also occur for  $n_1 \neq n_2$ , which is a case that might be particularly useful when selecting Rydberg states while subject to further experimental constraints.

The angular channels couple the initial state to different intermediate states, resulting in patterns of the Förster resonances since different  $(\Delta n_1, \Delta n_2)$  channels will be nearly resonant with the initial state. This is shown in Figure 3.9 for the three angular channels of the  $|n_1P_{1/2}, n_2P_{1/2}\rangle$  interaction that was already introduced in Figure 3.6. The three<sup>17</sup> angular channels are deter-

<sup>17</sup>The fourth channel with intermediate state  $|n'_1D_{3/2}, n'_2S_{1/2}\rangle$  can be derived from the  $|n'_1S_{1/2}, n'_2D_{3/2}\rangle$  channel

mined by the dipole selection rules, and in this case given by  $|n'_1 S_{1/2}, n'_2 S_{1/2}\rangle$ ,  $|n'_1 S_{1/2}, n'_2 D_{3/2}\rangle$ , and  $|n'_1 D_{3/2}, n'_2 D_{3/2}\rangle$ . For each of the three channels, the relevant Förster resonant intermediate pair states are shown in the lower rows of Figure 3.9. The coloured segments indicate the absolute value of the energy defect  $|\Delta|$  of the indicated order  $\Delta n_i$  for the respective near-resonant transitions.

In the case of the symmetric channels, one has to add the contribution of the case with permuted  $n_1$  and  $n_2$  to arrive at the full picture presented in the top row, which is indicated by the dashed black line in the respective panels. This is due to the symmetry of the energy defect under exchange of  $n_1$  and  $n_2$ . For the asymmetric channel coupling to one  $S$  and one  $D$  state, a permutation of states leads to the fourth' channel  $|n'_1 D_{3/2}, n'_2 S_{1/2}\rangle$  which corresponds to a transposition of the respective plot at the  $n_1 = n_2$  axis. The contributions from this permuted channel has to be taken into account as well when computing the total 2D map of interaction channel strengths, but is not shown here for simplicity.

Identifying the energy defect resonance curves in the  $(n_1, n_2)$ -plot allows to find regions of strong interactions also far away from the  $n_1 = n_2$  axis. This knowledge is useful if one wants to tune certain pair states into, or out of, resonance with the help of additional electromagnetic fields to fine-tune interaction strengths. However, the energy defect is not the only quantity that determines the interaction strengths. Different orders of  $\Delta n$ -channels have different radial coupling strengths due to changes in the radial overlap of the states, as discussed previously. Therefore, it is usually the channels with small changes in principal quantum numbers  $\Delta n_1$ ,  $\Delta n_2$  that contribute strongest to the interaction coefficients. It may additionally happen that a very strong Förster resonance occurs outside of the structure regions which leads to isolated incidences of strong second-order interactions. The sign of the energy defect  $\Delta$  determines the sign of the resulting interaction.

#### 3.2.3.4 STRUCTURES IN $C_6$ MAPS

As we have seen in equation (3.13), the angular dependency of the second order interaction depends on the interplay of the angular dependencies of the different angular momentum channels and their relative weighting. The relative weightings  $C_6^{(\tilde{l}_i \tilde{j}_i)}$  are a function of the radial coupling strengths  $\mathcal{R}_j^{(l)}$  of the atomic transitions and the energy defect of the intermediate pair state  $\Delta$ , as can also be seen in equation (3.12). The structures arising in the 2D map 3.6 for any spatial orientation  $(\theta, \phi)$  therefore depend on the structures in the  $C_6^{(\tilde{l}_i \tilde{j}_i)}$  coefficients and their interplay at any given set of angles. This interplay between the channels is determined by the angular dependency of each channel, which can, on a conceptual level, be reduced to the overlap of initial and final  $m_j$  states subject to the second-order interaction.

Strong anisotropy of the interactions therefore occurs when a single angular momentum channel dominates the interaction dynamics, but a cancellation of the angular dependency occurs if the different channels balance another. Strong domination of a single channel occurs on Förster resonance of the given channel, as shown in Figure 3.10, though the resulting interaction strength also crucially depends on the radial coupling of the single-atom transitions  $\mathcal{R}_j^{(l)}$ . The 2D interaction maps can therefore be understood when considering the interplay of the key

---

by permutation of the states and is therefore not counted separately here.

ingredients: angular dependency of the angular momentum channels, and Förster resonant pair states with their respective radial coupling strengths.

Furthermore, the sign of the interaction coefficient, i.e. whether the interaction is attractive or repulsive, is determined by the sign of the energy defect. Changes in sign of the energy defect  $\Delta$  occur near the Förster resonance lines and allow a further tailoring of the interaction.

State hopping, where the second-order interaction leads to (partial) exchange of quantum numbers between the two atoms, is possible whenever the initial and final state quantum numbers are dipole-coupled. In generic situations the probability to find the atoms with (partially) exchanged quantum numbers is orders of magnitude lower than the process  $|i\rangle \rightarrow |f\rangle = |i\rangle$ . But in some situations where the respective radial coupling is strong, like e.g. for similar principal quantum numbers  $n_1 \approx n_2$ , state hopping may contribute significantly to the pair-state dynamics. While being on Förster resonance with any particular intermediate state, the second-order process is not virtual but the intermediate state is actually populated. This leads to additional dipole-dipole interactions between the initial and intermediate pair states. These interactions are not present in the van der Waals regime where the second-order process is virtual and the intermediate state is not (significantly) populated due to the large energy defect  $\Delta$ .

### 3.2.3.5 FÖRSTER ZERO STATES IN DEGENERATE MANIFOLDS

An interesting case that deserves special mention due to its relevance for applications is that of so-called Förster zero states [113] which can occur in degenerate manifolds of  $|m_j\rangle$  states. In this case one finds that initial states, which might constitute of a superposition of  $|m_{j1}, m_{j2}\rangle$  sublevels, couple only weakly to some angular momentum channels. These states were termed Förster zero states and will be denoted as  $\{|F_j^0\rangle\}_j$ . For a given initial state  $|i\rangle$ , the overlap of  $|\bar{i}\rangle = \hat{\mathcal{W}}^\dagger(\theta, \phi) |i\rangle$  with the Förster zero state(s) depends on the spatial orientation of the atoms  $(\theta, \phi)$ . There might be sets of angles for which the overlap with the zero state(s) is large while it is small for other angles. Förster zero states do not occur if the intermediate state fulfills  $\tilde{j}_i > j_i$  for both atoms, but for any other channels there may be at least one Förster zero state [106]. If one seeks to avoid these (near) zeros in  $C_6(\theta, \phi)$  for any set of angles, then one has to choose an interaction that is dominated by the angular momentum channel satisfying  $\tilde{j}_i > j_i$  for  $i = 1, 2$ .

The presence of Förster zero states in any angular momentum channel can be detected by studying the eigenvalues of  $\hat{\mathcal{D}}(\tilde{l}_i, \tilde{j}_i)$ . For the near-zero eigenvalues, one has a corresponding number of Förster zero states which are given by the respective eigenvectors. A potential change in sign of  $C_6$  can equally be detected from the eigenvalues, but this time of the full interaction  $\sum_{(\tilde{l}_i, \tilde{j}_i)} C_6(\tilde{l}_i, \tilde{j}_i) \hat{\mathcal{D}}(\tilde{l}_i, \tilde{j}_i)$ . If eigenvalues of both signs exist, then there might be a change in sign of  $C_6$  at angles  $\{(\theta_j^0, \phi_j^0)\}_j$ , conditional on the overlap of the initial state  $|i\rangle$  with the respective eigenstates as the angles  $(\theta, \phi)$  are changed. An example for such a case with zero interaction and a change in sign of  $C_6$  is shown in Figure 3.7 (c) for the  $|110P_{1/2}, 110P_{1/2}, m_{j1} = m_{j2} = +1/2\rangle$  state, which is dominated by the intermediate state channel coupling to  $|\tilde{n}_1S_{1/2}\tilde{n}_2S_{1/2}\rangle$ .

This effect is of practical relevance since it results in varying  $C_6$  interaction strengths for ensembles with varying spatial orientations. For such ensembles, the Rydberg blockade radius is therefore inconsistent and is determined by the weakest interaction. For experiments with large clouds and randomly orientated atoms this effect has to be taken into account since Förster zero states can crucially change the interaction dynamics. If one seeks reliable blockade, one is

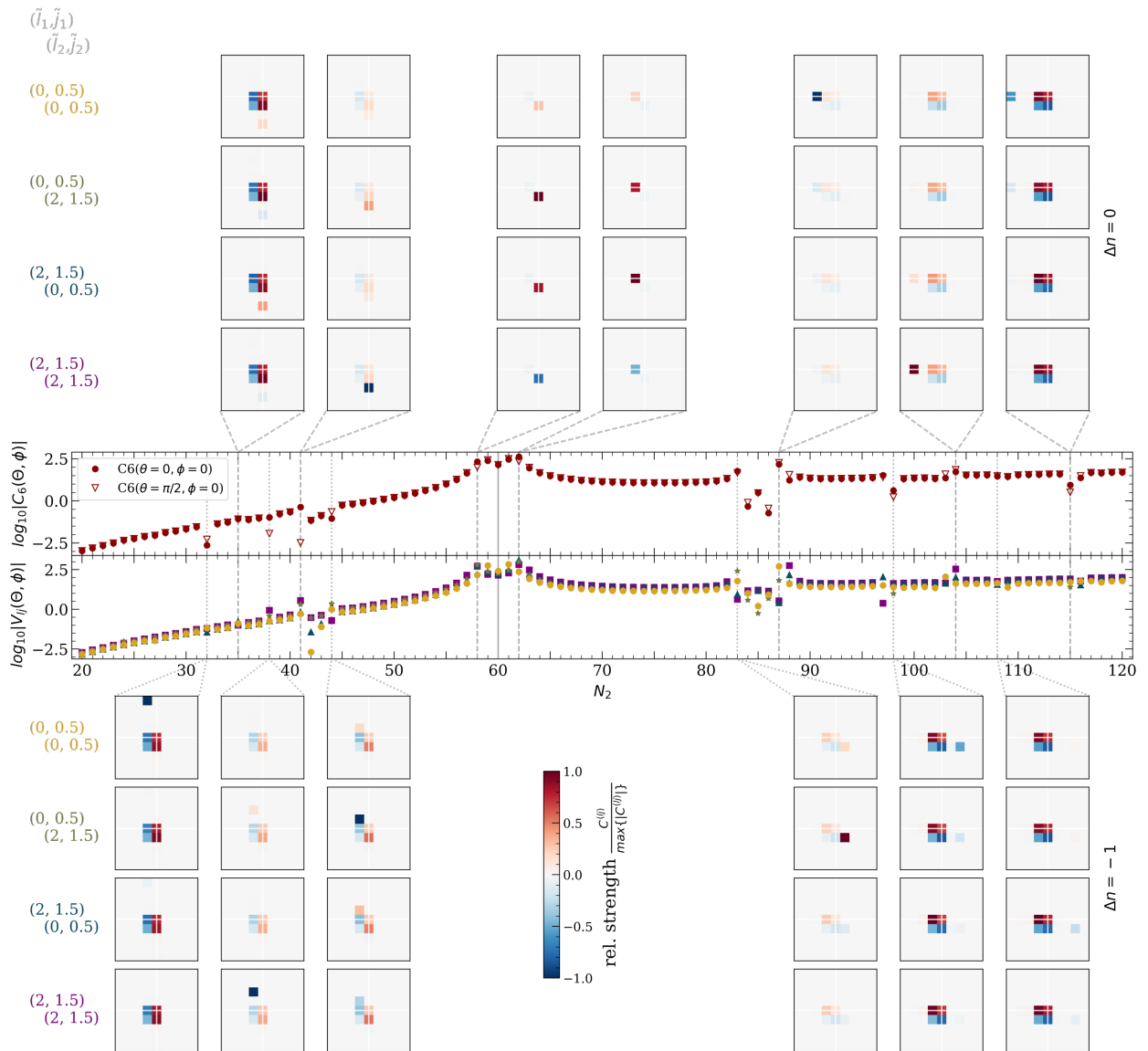


**Fig. 3.10: Förster resonance structure and resulting angular dependency of  $C_6(60S_{1/2}, n_2S_{1/2})$  in rubidium.**  $C_6(60S_{1/2}, n_2S_{1/2})$  values are plotted in the upper central panel for  $m_{j1} = m_{j2} = +1/2$  and  $\theta = 0$  (closed dot),  $\theta = \pi/2$  (open triangle). The corresponding values  $|C_6^{(\tilde{l}_i, \tilde{j}_i)}|$  of the angular momentum channels are plotted below and colour-coded as specified by the coloured labels of the inset rows. The insets show the total radial coupling strength divided by energy defect, resolved by intermediate state principal quantum numbers  $\tilde{n}_1$  and  $\tilde{n}_2$ , for the four angular channels separately. White lines indicate the values for which  $\Delta n_i = 0$ , with the insets orientated such that  $\tilde{n}_1$  on the horizontal and  $\tilde{n}_2$  on the vertical. The magnitude and sign of the respective  $(\tilde{n}_1, \tilde{n}_2)$  contributions are encoded in the colourbar. The Förster resonances with  $\Delta n_i = -1, 0$  and varying orders of  $\Delta n_j$  are visible in the insets and correspond to strong angular dependencies of  $C_6$ . This is easily understood when considering the spread in angular momentum channel contributions on the resonances.

therefore advised to choose states with the interactions dominated by the angular momentum channel satisfying  $\tilde{j}_i > j_i$  for  $i = 1, 2$ . This channel is free of Förster zeros and therefore provides the required reliability of the blockade. Alternatively, one can get rid of the Förster zero conditions by lifting the  $m_j$  degeneracy through application of electromagnetic fields.

### 3.2.4 TUNABILITY OF INTERACTIONS WITH ELECTRIC AND MAGNETIC FIELDS

It has been mentioned before that the strongest interactions occur on Förster resonance where two degenerate pair states  $|r_1, r_2\rangle$  and  $|r'_1, r'_2\rangle$  are resonantly coupled via dipole interactions mediated by  $\hat{V}_{dd}(\mathbf{R})$ . In this case, the interaction strength was shown to scale as  $\propto 1/R^3$  in distance, which leads to long-range interactions. However, for any given initial pair state there is usually only a very small number of state combinations that is (nearly) on Förster resonance. If one is restricted to the use of certain initial pair states for experimental reasons, one can still try to arrive at Förster resonance with a second pair state by applying additional electric or magnetic fields. These fields do two important things at once – firstly, they lift the degeneracy of the  $|n, l, j\rangle$  state manifold by adding an  $m_j$ -dependent level shift. Secondly, these level shifts can be used to fine-tune the residual energy defect between the  $|r_1, r_2\rangle$  and  $|r'_1, r'_2\rangle$  pair states by making use of differential Stark- or Zeeman shifts of the different  $m_j$  states. This has been used in e.g. [102] to isolate a single pair-state transition on the  $m_j$  fine-structure level.

For sufficiently weak fields such that  $(n, l, j)$  are still good quantum numbers, one can then proceed in the calculation of the interaction strengths by taking the field-induced level shifts of the  $m_j$  states into account. One consequently finds the Förster resonances and extrema in the interaction strength dependent on the  $m_j$  state and field strengths – different  $m_j$  states will have their strongest interactions at different field strengths. This tunability of the interaction strength provides another tool to engineer interactions between neutral atoms on demand by simply changing the strength and/or orientation of the externally applied electric or magnetic fields.

### 3.2.5 EXAMPLE APPLICATION: PHOTON-PHOTON INTERACTION ON DEMAND

A fundamental understanding of the second-order interaction processes can be utilised in many different ways. For instance, it might be the case that one has to use certain Rydberg states due to other experimental constraints, but the interactions are not particularly suitable for the purpose. An analysis of the contributing interaction channels and mapping out potentially accessible Förster resonances allows to fine-tune and tailor the resulting Rydberg-Rydberg interactions with externally applied electromagnetic fields. This can be used to enhance the interactions by bringing a particular pair state into resonance, but it obviously works in the reverse way as well by reducing resonant energy transfer when detuning a pair state from Förster resonance. Certain angular dependencies of the interaction can also be engineered in this fashion, which can then be exploited by use of appropriate spatial geometries. For example, a strong angular dependency could be used for fast switching of the interaction strength in a 1D chain of atoms by fast changes of the orientation of the quantisation axis.

Lastly, the 2D interaction maps with their inherent resonances can also be used in a different fashion. By looking at the structure in e.g. Figure 3.6 one can identify pairs of pair states with re-

spective interaction strengths varying by orders of magnitude<sup>18</sup>. Driving between such pairs of pair states is therefore an alternative way to generate a rapid change in interaction strength. This scheme could be used to generate an effective on-demand interaction between two photons. It has been mentioned in Chapter 2.1.2 that two photons effectively do not interact with another, but when transferring a photon into a quasiparticle called polariton it inherits some properties of matter. One of these inherited properties is the strong interaction between Rydberg atomic states. Putting one and one together then provides a protocol to generate an effective interaction between two photons on demand: Initially, the two photons are transferred into Rydberg polaritons with two distinct Rydberg states that interact only weakly. To induce the effective interaction between the two photons one then transfers the Rydberg polaritons into a strongly interacting pair state by application of a suitable coupling field to each polariton. Since this driving between the strongly and weakly interacting pair states occurs on demand one has obtained all necessary ingredients and control tools required for the task. Eventually, the polaritons can be released from their host medium and recovered in the form of photons.

---

<sup>18</sup>This is particularly pronounced for some pair states on higher-order resonances away from the  $n_1 = n_2$  axis.

## 4 | THEORETICAL MODEL

As shown in the previous chapters, Rydberg atomic systems are known to have exceptional properties due to the scaling of the Rydberg-Rydberg interaction with principal quantum number  $n$ . Interestingly, they also show behavior that is not naïvely expected for such systems. For instance, optical bistability has been observed in hot Rydberg vapors [114]. Different theoretical models have been employed to explain the origin of the bistability and the resulting hysteresis effects. Notably, both Rydberg-Rydberg interactions [115, 116] and plasma formation of ionised Rydberg atoms [63] have been shown, theoretically, to lead to optical bistability in the response of a vapour. In essence, both approaches have in common a non-linear interaction mechanism which causes a change in the stability of the system and produces multiple steady state solutions for a single set of external driving parameters.

There is recent experimental evidence showing that plasma formation occurs in a hot Rydberg vapour in the strong driving regime [63, 117] and can account for much of the resulting lineshapes [63]. The underlying effect is a line broadening due to Stark shifts of the atomic levels, caused by the surrounding ions. Due to the locally different electric fields for every atom in the vapour and the different Doppler detunings due to atomic motion, simulations of such a vapour become tedious and evade analytical solutions.

Based on the optical Bloch equations, we have set up a model including a generic nonlinear Rydberg-density dependent level shift of the Rydberg state. We were aiming for simplicity of the model to eventually gain further insight into the role that Rydberg interactions and ion-induced level shifts play in the dynamics and response of a continuously driven hot vapour in the strong driving regime. Therefore, we have not merely reproduced the methodology of the plasma formation approach [63] but set up a simpler model which allows for a more intuitive understanding of the resulting dynamics of the system.

The resulting model is first presented for an effective two-level system in Section 4.2.1 due to the existence of partially analytical solutions for the resulting equations, and then extended to a three-level model in Section 4.2.3. This treatment of a single velocity class is then extended to a simulation of a hot vapour in Section 4.4. The chapter is completed by establishing links to well-known phenomena such as ergodicity breaking and time crystals, but also to famous models like the Kuramoto model, in Section 4.5.

The sections on stability of steady states, Hopf bifurcation, and synchronisation put an emphasis on the mathematical aspects of those phenomena within the framework of the theory of dynamical systems and can be omitted by readers familiar with the mathematical background.

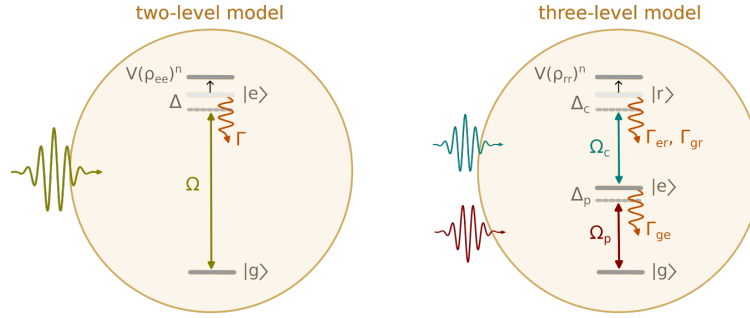


**Fig. 4.1: Level schemes for 2-level and 3-level model.** The two-level model consists of an atom with ground state  $|g\rangle$  and excited state  $|e\rangle$ , coupled by a field with Rabi frequency  $\Omega$  and a detuning  $\Delta$  from resonance. The decay  $\Gamma$  represents a decay mode from  $|e\rangle \rightarrow |g\rangle$ , i.e. it is assumed that there is no decay out of the basis states. In the three-level model, this assumption is also made which leads to decay channels  $\Gamma_{ge}$ ,  $\Gamma_{er}$  and  $\Gamma_{gr}$  between the basis states  $\{|g\rangle, |e\rangle, |r\rangle\}$ . The states  $|g\rangle$  and  $|e\rangle$  ( $|e\rangle$  and  $|r\rangle$ ) are coupled via a probe (coupling) field of Rabi frequency  $\Omega_p$  ( $\Omega_c$ ). In both models, the additional level shift due to a power law interaction in  $V(\rho_{ee})^n$  and  $V(\rho_{rr})^n$  is indicated by the arrow and shifted state energy.

## 4.1 INTRODUCTION TO THE MODEL SYSTEMS

Based on the optical Bloch equations, one can set up the equations of motion for an  $n$ -level system. This captures the coherent atom-light interaction processes, but does not account for incoherent processes like dephasing or population decay. In a hot vapour, these mechanisms play a significant role and so does the Doppler-shift induced level detuning. These incoherent processes are included in the model by adding dissipation and dephasing terms, and calculating the equations of motion via the quantum Liouville (Lindblad) equation (2.4). The incoherent decay and dephasing<sup>1</sup> rates originate from atomic state decay, collisional dephasing and decay, transit time broadening, and dephasing due to laser noise. Further effects such as power broadening [118] could also be taken into account.

Furthermore, our model contains an additional Rydberg-population dependent level shift given by  $V\rho_{ee}^n$  and  $V\rho_{rr}^n$  for the two- and three-level model, respectively. The choices one makes for the coupling strength  $V$  and the power law scaling  $n$  determine the model. This allows to model Rydberg-Rydberg interaction in the vapour and to approximate the plasma formation model.

Without specifying these parameters any further one can find expressions determining the steady state solutions of the model systems. For the sake of generality, those solutions will be derived before further detailing and specifying the model by fixing the power law  $n$  and interaction parameter  $V$ . A discussion of the choice of those parameters is therefore deferred until Section 4.3.

<sup>1</sup>The models as presented here do not include dephasing of the coherences with rates  $\gamma_{ij}$ , hence those are not indicated in Figure 4.1. At the relevant positions in the text it is mentioned how one can easily extend the model to include dephasing.

## 4.2 STEADY STATE SOLUTIONS FOR A SINGLE VELOCITY CLASS

The time evolution of our dissipative  $n$ -level model system is governed by the quantum Liouville (Lindblad) equation, as described in Chapter 2. The steady state solutions for a single velocity class<sup>2</sup>  $\mathbf{v}_i$  can be found by setting the left-hand side of equation (2.4) to zero, i.e.  $\dot{\rho} = 0$  for the  $n$ -level density matrix  $\rho$ . Without further specification of the physical parameters, one can study the steady state properties of the effective 2-level and the 3-level model. In some parameter regimes, the resulting behavior will turn out to be qualitatively very different for the 2- and 3-level models.

The effective 2-level model will be studied first as an introduction to the approach and methodology – and because it has partially analytical solutions, which makes it very instructive to study. For the three-level model, the presented approach no longer leads to (partially) analytical solutions<sup>3</sup> since there is no general expression for the roots of a polynomial of order  $> 4$  in terms of radicals, as stated by the Abel-Ruffini theorem [121, 122]. However, the presented approach leads to a much more efficient calculation of the steady states of the system via the roots of a polynomial, as opposed to a numeric integration of the system until a steady state is reached. Additionally, the three-level model shows self-oscillation in certain parameter regimes, which is one manifestation of the nonlinearity of the system for  $n \neq 0$ .

### 4.2.1 EFFECTIVE 2-LEVEL MODEL

The effective two-level model, shown in Figure 4.1, is governed by the coherent atom-light Hamiltonian  $\mathcal{H}_{\text{AL}}$ , the excited state population dependent level shift  $\mathcal{H}_{\text{shift}}$

$$\mathcal{H} = \mathcal{H}_{\text{AL}} + \mathcal{H}_{\text{shift}} = \frac{\hbar}{2} \begin{pmatrix} 0 & \Omega \\ \Omega & -2\tilde{\Delta} \end{pmatrix} + \hbar \begin{pmatrix} 0 & 0 \\ 0 & V\rho_{ee}^n \end{pmatrix} \quad (4.1)$$

where the  $\rho_{ee}^n$  in the Hamiltonian  $\mathcal{H}_{\text{shift}}$  represents the expectation value, not an operator, and the Lindblad term  $\mathcal{D}(\rho)$

$$\mathcal{D}(\rho) = \begin{pmatrix} \Gamma\rho_{ee} & -\frac{1}{2}\Gamma\rho_{ge} \\ -\frac{1}{2}\Gamma\rho_{eg} & -\Gamma\rho_{ee} \end{pmatrix}. \quad (4.2)$$

$\tilde{\Delta}$  includes the Doppler detuning of velocity class  $\mathbf{v}_i$ , i.e. is the effective detuning of this velocity class from resonance, and  $\Gamma$  denotes the decay from  $|e\rangle \rightarrow |g\rangle$ . The resulting equations of motion for the system follow from equation (2.4) as

$$\dot{\rho}_{gg} = -\Omega_p \text{Im}(\rho_{ge}) + \Gamma\rho_{ee}, \quad (4.3a)$$

$$\dot{\rho}_{ee} = +\Omega_p \text{Im}(\rho_{ge}) - \Gamma\rho_{ee}, \quad (4.3b)$$

$$\dot{\rho}_{ge} = -\frac{i}{2}\Omega(\rho_{ee} - \rho_{gg}) - \frac{1}{2}\Gamma\rho_{ge} - i\left(\tilde{\Delta} - V\rho_{ee}^n\right)\rho_{ge}. \quad (4.3c)$$

<sup>2</sup>For any single velocity class  $\mathbf{v}_i$  of atoms moving along the direction of propagation of a light field, the respective transition is Doppler shifted to  $\tilde{\Delta}_x = \Delta_x - \mathbf{k}_x \cdot \mathbf{v}_i$ , where  $\Delta_x$  denotes the transition detuning for atoms stationary in the lab frame and  $\mathbf{k}_x$  the wave vector of the respective laser  $x$ .

<sup>3</sup>Analytical expressions exist for three-level EIT models without the additional Rydberg-population dependent level shift. Further details on EIT in three-level systems can be found in the initial proposal and experimental paper [119, 120], and e.g. in this review on EIT [18].

When finding the steady state solutions, i.e. after setting the time derivative on the left-hand side to zero, it is straightforward to reduce the above system of equations by reformulating the populations<sup>4</sup> in terms of real and imaginary part of the coherence  $\rho_{ge}$ . We also make use of the trace condition  $1 = \sum_j \rho_{jj}$  which enshrines the conservation of population – and therefore probability – over time for any  $n$ -level system. The steady state equations corresponding to system (4.3) therefore boil down to two equations in  $\mathbb{R}$ , one each for real and imaginary part of the coherence<sup>5</sup>  $\rho_{ge}$ . These remaining two equations give the steady state solutions of system (4.3) via

$$\rho_{gg}^i = \rho_{ee}^i = 0, \quad (4.4a)$$

$$\rho_{gg}^r = 1 - \rho_{ee}^r = 1 - \frac{\Omega}{\Gamma} \rho_{ge}^i, \quad (4.4b)$$

$$\rho_{ee}^r = \frac{\Omega}{\Gamma} \rho_{ge}^i, \quad (4.4c)$$

$$\rho_{ge}^r = \frac{2}{\Gamma} \left[ \tilde{\Delta} - V \left( \frac{\Omega}{\Gamma} \rho_{ge}^i \right)^n \right] \rho_{ge}^i, \quad (4.4d)$$

$$0 = (\rho_{ge}^i)^{2n+1} \left[ \frac{2}{\Gamma} V^2 \left( \frac{\Omega}{\Gamma} \right)^{2n} \right] - (\rho_{ge}^i)^{n+1} \left[ \frac{4}{\Gamma} V \tilde{\Delta} \left( \frac{\Omega}{\Gamma} \right)^n \right] + \rho_{ge}^i \left[ \frac{\Omega^2 + 2\tilde{\Delta}^2}{\Gamma} + \frac{\Gamma}{2} \right] - \frac{\Omega}{2}. \quad (4.4e)$$

The roots of the polynomial (4.4e) in  $\rho_{ge}^i$  determine the steady state solutions of system (4.3) uniquely. A polynomial of order  $k$  with real coefficients, as the one above, has  $k$  solutions in  $\mathbb{C}$  – this follows from the Fundamental Theorem of Algebra [123, 124], also known as d’Alembert’s theorem.

However, since real and imaginary part of the coherence were treated separately, we expect a physical solution to be a real solution of equation (4.4e). Also, not every real solution is necessarily a physical solution. Having made use of the trace condition guarantees that all populations sum up to one for all possible solutions, but say a negative ground state population and a correspondingly large excited state population would also sum up to one. This would be very unphysical in light of our interpretation of the populations as being the probability of finding the system in a given state upon measurement, i.e.

$$P(|i\rangle) = \langle i | \rho | i \rangle = \rho_{ii}. \quad (4.5)$$

It is shown in Appendix A.1 that all real solutions of equation (4.4e) lie in the interval  $[0, \frac{\Gamma}{\Omega}]$  which implies that the interpretation of those real solutions as state probabilities are always valid.

Without actually finding the roots of the polynomial we can already give a statement on the maximum number of real solutions that we could expect to find. For the trivial case of a constant level shift of the excited state, i.e.  $V \neq 0$  and  $n = 0$ , one finds the steady state solution for

<sup>4</sup>The imaginary part of the populations is always zero since the density matrix is hermitian, i.e.  $\rho^\dagger = \rho \Rightarrow \text{Im}(\rho_{ii}) = 0 \forall i \in [1, n]$  for any  $n$ -level system described by  $\rho$ .

<sup>5</sup>We will use the notation  $\text{Re}(\rho_{kl}) = \rho_{kl}^r$  and  $\text{Im}(\rho_{kl}) = \rho_{kl}^i$  throughout the thesis.

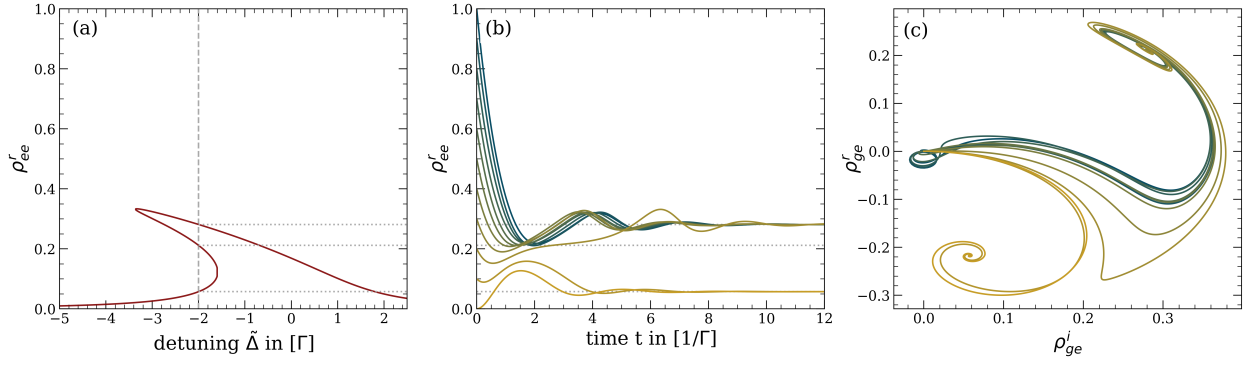


**Fig. 4.2: Bistability in the 2-level model.** (a) shows the steady state population in the excited state for  $\Omega/\Gamma = 1$ ,  $V/\Gamma = -30$  and  $n = 2$ . In (b), the dynamical evolution of system (4.3) towards the stable steady states is shown for initial states  $|\Psi\rangle_{t=0} = (1-x)|g\rangle + x|e\rangle$  with  $x \in [0, 1]$ . The detuning  $\tilde{\Delta} = -2$  is chosen such that the system has three steady states, two of which are attractive and one repulsive, and is indicated with the gray dashed line in (a). In (c), real and imaginary part of the coherence  $\rho_{ge}$  are shown for the time traces in (b).

$\rho_{ge}^i$  to be analytical with always exactly one solution to equation (4.4e) for all sets of external parameters. In this case, the response of the system is just shifted in energy by a fixed value, but otherwise remains identical to the unperturbed case.

$$n = 0 : \quad \rho_{ge}^i = \frac{\Omega/2}{\frac{\Omega^2 + 2(\tilde{\Delta} - V)^2}{\Gamma} + \frac{\Gamma}{2}}. \quad (4.6)$$

When assuming a level shift of the excited state linearly in  $\rho_{ee}$ , i.e. when setting  $n = 1$ , the situation changes fundamentally. The leading term of the polynomial (4.4e) is cubic with well-known expressions for the roots. One now finds either one or three real solutions for a single set of external parameters  $\{\Omega, \tilde{\Delta}, \Gamma, V\}$ . When having three real solutions, then all of them are physical in the sense that they allow for an interpretation of the populations as state probabilities. However, not all three of the steady state solutions are stable.

Figure 4.2 (a) shows an example for such a case of multiple steady states in the 2-level system, the middle branch in the region of three solutions is unstable. This means that the system would never dynamically develop into this steady state, unless it was initialised exactly in that state. Any tiny deviation from the unstable steady state would lead to a dynamical evolution further away from that state - towards a stable steady state, if that exists. Panel (b) in Figure 4.2 shows how the different initial states  $|\Psi\rangle_{t=0} = (1-x)|g\rangle + x|e\rangle$  develop towards one of the two stable steady states over time for the set of initial parameters marked by the gray dashed line in (a). The time traces of (b) are plotted again in (c), but now in the space spanned by the coherence  $\rho_{ge}$ . The system always starts in  $\rho_{ge} = 0$  but is attracted towards two separate steady state values, depending on the initial state of the system at  $t = 0$ .

A further point to note is that those sets of external parameters  $\{\Omega, \tilde{\Delta}, \Gamma, V\}$ , where the number – or nature – of the steady state solutions of a dynamical system changes, is called a bifurcation point. The mathematical field of bifurcation theory has led to a rich and varied study of bifurcations in dynamical systems, and this thesis uses some of the results and findings of the

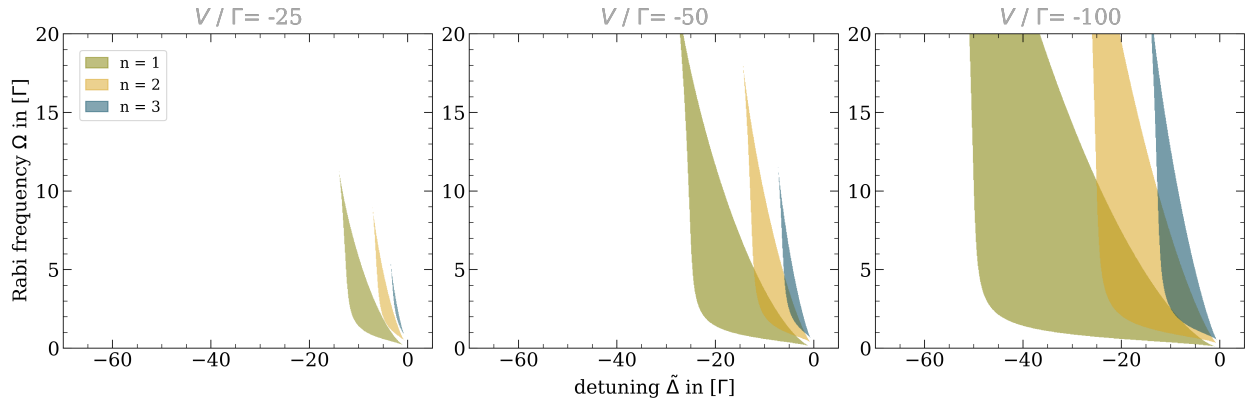


**Fig. 4.3: Scaling of the bistable region in the 2-level model.** The bistable region is shown for a range of detunings  $\tilde{\Delta}/\Gamma$ , Rabi frequencies  $\Omega/\Gamma$ , interaction strengths  $V/\Gamma$ , and  $n$ . A general increase in the size of the bistable region with increasing interaction strength  $V$  and decreasing power  $n$  is apparent.

field. However, for ease of reading a more mathematical treatment is deferred until the following Section 4.2.2 on the stability analysis of steady states.

For any  $n > 1$ , i.e. for a scaling of the excited state level shift beyond linear in the excited state population, one finds that the polynomial (4.4e) does not have a general analytical solution. However, we can still state that there is a maximum of three steady state solutions of system (4.3) for any given set of external parameters. This follows from Descartes' rule of signs [125, 126] which states that a polynomial

$$\mathcal{P}(\lambda) = \alpha_k \lambda^k + \dots + \alpha_1 \lambda + \alpha_0$$

of degree  $k$  over  $\mathbb{R}$  has at maximum  $l \leq k$  positive real roots with  $l$  being the number of sign flips in the sequence of coefficients  $\{\alpha_j \mid \alpha_j \in \mathbb{R} \text{ for } 0 \leq j \leq k\}$ <sup>6</sup>. Additionally, one always has a minimum of one steady state solution since the polynomial is of an odd order. Figure 4.3 shows the scaling of the bistable region with  $n \in \{1, 2, 3\}$  and  $\Omega/\Gamma \in [0, 20]$  for different values of the interaction strength  $V/\Gamma$ . The detuning  $\tilde{\Delta}/\Gamma$  is the so-called bifurcation parameter since this parameter is varied and the system's response is observed for any fixed set of  $\{\Omega, V, \Gamma, n\}$ .

Computationally, it is considerably more efficient to find the roots of the polynomial via numerical methods than integrating system (4.3) until a steady state is reached. However, finding all real roots of a polynomial can be tricky as common root finding algorithms do not guarantee to find all real roots. There are algorithms based on Descartes' rule of signs or Sturm's theorem which are complete insofar as they return all real roots of a polynomial. For reasons of computation time and ease of implementation, we have used an alternative method to find all real roots of the polynomial based on the companion matrix [124] of a polynomial has all roots of the polynomial in  $\mathbb{C}$  as eigenvalues, and therefore also all the real ones. In Python, the eigenvalues of a matrix can be computed efficiently using numpy<sup>7</sup>.

<sup>6</sup>A corollary of this theorem can be applied to find the maximum possible number of negative real roots by counting the number of sign changes of the sequence when multiplying the odd coefficients with  $-1$ .

<sup>7</sup>The numerical results have turned out to be stable and accurate within the parameter regimes of relevance for

### 4.2.2 STABILITY ANALYSIS OF STEADY STATES IN DYNAMICAL SYSTEMS

Having established the number of possible steady state solutions of the effective two-level system, we can now study the stability of those solutions. In a physical sense this is synonymous to the question of whether or not the system will approach a steady state for a given initial state - and which one, in case of several steady states. Here, we do not present the concepts in a mathematically rigorous fashion but give a brief overview of the tools required for the stability analysis of the steady states. A sound mathematical treatment of the problem can be found in e.g. [127, 128].

When the time evolution of the state  $x$  of a dynamical system is given by a differential equation

$$\frac{dx}{dt} = X_\mu(x) \quad (4.7)$$

then the steady states<sup>8</sup> of the system are those  $x_0 \in U$  such that

$$X_\mu(x_0) = 0. \quad (4.8)$$

Here, the set  $U$  is a suitable subset of the phase space of the system and the subscript  $\mu$  denotes the other parameters which the system may depend on. The differential equation (4.7) is a set of equations of motion that do not explicitly depend on time  $t$  on the right-hand side.

For instance, when considering a dissipative system defined via

$$\dot{\rho} = -\frac{i}{\hbar} [\mathcal{H}, \rho] + \mathcal{D}(\rho)$$

then setting the left hand side to zero, i.e.  $\dot{\rho} = 0$ , and solving for  $\rho$  results exactly in the set of steady states of the system. Those are the set of points for which the corresponding flow  $\Phi_\mu^t$  maps the points onto themselves, i.e.  $\Phi_\mu^t(x_0) = x_0 \forall t \in \mathbb{R}$ .

A steady state  $x_0$  of the differential equation (4.7) can generally either be stable or unstable. Broadly speaking,  $x_0$  is Lyapunov stable if there exists a neighborhood around  $x_0$  such that all trajectories starting in this neighborhood always remain within a finite distance  $\epsilon > 0$  to  $x_0$  for all  $t > 0$ . This means, effectively, that every trajectory starting near the equilibrium point  $x_0$  remains near the equilibrium for all time. A different, stronger notion of stability is called asymptotic stability. It refers to the situation where a sufficiently small perturbation  $\delta$  from the equilibrium point decays away as time evolves and the system returns to its equilibrium state for  $t \rightarrow \infty$ . Lyapunov stability is not as strict as asymptotic stability since it does not require convergence of the trajectory towards the equilibrium  $x_0$  in time, but it contains asymptotic stability and can still be a useful concept since  $\epsilon$  can be chosen very small. An unstable steady state, then, is one where for an arbitrary neighborhood of  $x_0$  one finds at least one trajectory that evolves away out of the neighborhood and does not return.

---

this thesis.

<sup>8</sup>We will use the terms steady state and equilibrium point interchangeably as they refer to the same state  $x_0$ . A fixed point of the corresponding flow  $\Phi_\mu^t$  is equally a steady state of  $X_\mu$ , but the reverse implication does not necessarily hold.

The stability of a steady state can be studied by considering the linearisation<sup>9</sup> of the map  $X_\mu$  around the critical point  $x_0$ . A steady state is asymptotically stable if the real part of all eigenvalues  $\lambda_j$  of the linearisation around  $x_0$  are negative. The steady state is unstable if at least one eigenvalue satisfies  $Re(\lambda_j) > 0$ <sup>10</sup>.

The linearisation of  $X_\mu$  at  $x_0$  is given by the Jacobi  $J_\mu$  evaluated at  $x = x_0$

$$J[X](x_0) = D_x X_\mu|_{x=x_0} \quad (4.9)$$

Finding the eigenvalues of  $J_\mu$  is equivalent to finding the roots of the characteristic polynomial  $\chi_\mu[J_\mu](\lambda)$ . It can be useful to study the characteristic polynomial  $\chi_\mu$  instead of the Jacobi  $J_\mu$ . Reason being that several theorems on the roots of polynomials exist that may be of help for deriving general statements on the stability of  $x_0$  without actually having to calculate the roots.

Using these tools one can now calculate the steady states  $x_0$  of a system and determine their stability. In many measurements, physicists are not concerned with the dynamical evolution of a system after initial stimulus but are rather interested in the steady states approached by the system after some time  $t$ . The system will then be observed in the steady state it was attracted to, given its initial conditions<sup>11</sup>. This dependence on the initial state of the system is also shown in Figure 4.2 (b) and (c).

We have used the two-level approach as an introduction to the required mathematical tools and as an illustration of the chosen approach to study the behavior of a single velocity class  $\mathbf{v}_i$  for a given set of external parameters.

The effective 2-level approach has an analytical solution for the characteristic polynomial of the linearisation, which permits an analytical study of the stability properties of the system. A further discussion of the stability of the steady state solutions for this model can be found in the Appendix A.1 but will not be discussed any further here as it does not produce time-periodic solutions<sup>12</sup> via Hopf bifurcation. The corresponding three-level model, however, leads to a very different type of steady state solutions since it undergoes Hopf bifurcation and produces said time-periodic orbits. We will therefore now look at the three-level model and its properties.

### 4.2.3 3-LEVEL MODEL

In the two-level model presented above we have simplified the often encountered situation of a two-photon transition by assuming a large detuning  $\Delta_p$  from the intermediate state. This allows to neglect the population dynamics of the intermediate state  $|e\rangle$  and justifies the use of a two-level system with effective Rabi frequency  $\Omega_{\text{eff}} \propto \Omega_p \Omega_c / \Delta_p$ .

<sup>9</sup>The Hartman-Grobman theorem [129] is applicable here and states that the stability of a hyperbolic equilibrium point of a nonlinear system is locally the same as that of its linearisation around the equilibrium point. An equilibrium point is hyperbolic if no eigenvalue of the linearisation evaluated at the equilibrium has a real part equal to zero.

<sup>10</sup>If there exists at least one eigenvalue with  $Re(\lambda) = 0$ , then stability of the steady state cannot be determined by use of the linearisation.

<sup>11</sup>Though it is technically possible to initialise a system in an unstable steady state, it will not be observed in that state after some time  $t$  given that any small deviation from the state leads to the system evolving away from it - and some degree of parameter fluctuations occurs even in the best experiments.

<sup>12</sup>This is shown in Appendix A.1.

In a hot vapour, however, the Doppler detuning of the different velocity classes can become very large and easily reaches the same order of magnitude as typical detunings  $\Delta_p$  from the intermediate state. A full three-level treatment of the system is therefore required in order to also include the population dynamics of the intermediate state.

The three-level model shown in Figure 4.1 is described by the coherent atom-light interaction of probe and coupling field, encoded in  $\mathcal{H}_{AL}$ , as well as the additional Rydberg-population dependent detuning encapsulated by  $\mathcal{H}_{shift}$

$$\mathcal{H} = \mathcal{H}_{AL} + \mathcal{H}_{shift} = \frac{\hbar}{2} \begin{pmatrix} 0 & \Omega_p & 0 \\ \Omega_p & -2\tilde{\Delta}_p & \Omega_c \\ 0 & \Omega_c & -2(\tilde{\Delta}_p + \tilde{\Delta}_c) \end{pmatrix} + \hbar \begin{pmatrix} 0 & 0 & 0 \\ 0 & 0 & 0 \\ 0 & 0 & V\rho_{rr}^n \end{pmatrix}, \quad (4.10)$$

where  $\rho_{rr}^n$  in  $\mathcal{H}_{shift}$  is again an expectation value, not an operator, and the incoherent processes, resulting in

$$\mathcal{D}_{tot.}(\rho) = \begin{pmatrix} \Gamma_{ge}\rho_{ee} + \Gamma_{gr}\rho_{rr} & -\frac{\Gamma_{ge}}{2}\rho_{ge} & -\frac{\Gamma_{gr} + \Gamma_{er}}{2}\rho_{gr} \\ -\frac{\Gamma_{ge}}{2}\rho_{eg} & -\Gamma_{ge}\rho_{ee} + \Gamma_{er}\rho_{rr} & -\frac{\Gamma_{ge} + \Gamma_{er} + \Gamma_{gr}}{2}\rho_{er} \\ -\frac{\Gamma_{gr} + \Gamma_{er}}{2}\rho_{rg} & -\frac{\Gamma_{ge} + \Gamma_{er} + \Gamma_{gr}}{2}\rho_{re} & -(\Gamma_{gr} + \Gamma_{er})\rho_{rr} \end{pmatrix}. \quad (4.11)$$

If the model is to be extended to include additional dephasing of the coherences  $\gamma_{ij}$ , then those are simply added to the respective incoherent terms via  $(\mathcal{D}_{tot.})_{(i,j)} \rightarrow (\mathcal{D}_{tot.})_{(i,j)} + \gamma_{ij}\rho_{ij}$ . In this notation,  $\tilde{\Delta}_x$  again denotes the effective detuning of the velocity class of interest, i.e. including the motion-induced Doppler detuning. The resulting equations of motion follow as

$$\dot{\rho}_{gg} = -\Omega_p \text{Im}(\rho_{ge}) + \Gamma_{ge}\rho_{ee} + \Gamma_{gr}\rho_{rr}, \quad (4.12a)$$

$$\dot{\rho}_{ee} = +\Omega_p \text{Im}(\rho_{ge}) - \Omega_c \text{Im}(\rho_{er}) - \Gamma_{ge}\rho_{ee} + \Gamma_{er}\rho_{rr}, \quad (4.12b)$$

$$\dot{\rho}_{rr} = +\Omega_c \text{Im}(\rho_{er}) - (\Gamma_{gr} + \Gamma_{er})\rho_{rr}, \quad (4.12c)$$

$$\dot{\rho}_{ge} = -\frac{i}{2}\Omega_p(\rho_{ee} - \rho_{gg}) + \frac{i}{2}\Omega_c\rho_{gr} - i\tilde{\Delta}_p\rho_{ge} - \frac{\Gamma_{ge}}{2}\rho_{ge}, \quad (4.12d)$$

$$\dot{\rho}_{er} = -\frac{i}{2}\Omega_c(\rho_{rr} - \rho_{ee}) - \frac{i}{2}\Omega_p\rho_{gr} - i(\tilde{\Delta}_c - V(\rho_{rr})^n)\rho_{er} - \frac{\Gamma_{ge} + \Gamma_{er} + \Gamma_{gr}}{2}\rho_{er}, \quad (4.12e)$$

$$\dot{\rho}_{gr} = -\frac{i}{2}\Omega_p\rho_{er} + \frac{i}{2}\Omega_c\rho_{ge} - \frac{\Gamma_{gr} + \Gamma_{er}}{2}\rho_{gr} - i(\tilde{\Delta}_p + \tilde{\Delta}_c - V(\rho_{rr})^n)\rho_{rg}. \quad (4.12f)$$

As in the two-level case, one can define the steady state solutions of system (4.12) via the roots of a polynomial in the imaginary part of the coherence  $\rho_{er}$  by using the trace condition and hermiticity of the density matrix  $\rho$ . The resulting expressions are rather longish and complicated, a summary and description of the necessary steps as well as a complete expression of the results are therefore given in in the Appendix A.2.

However, a brief look at the general form of the polynomial defining the steady state values is of interest here. For a Rydberg-population induced detuning scaling to the power of  $n$ , i.e.  $V(\rho_{rr})^n$ , one finds that the resulting polynomial  $\mathcal{P}(\rho_{er}^i)$  is of the form

$$\mathcal{P}(\rho_{er}^i) = \sum_{k \in X} \alpha_k (\rho_{er}^i)^k \quad (4.13)$$

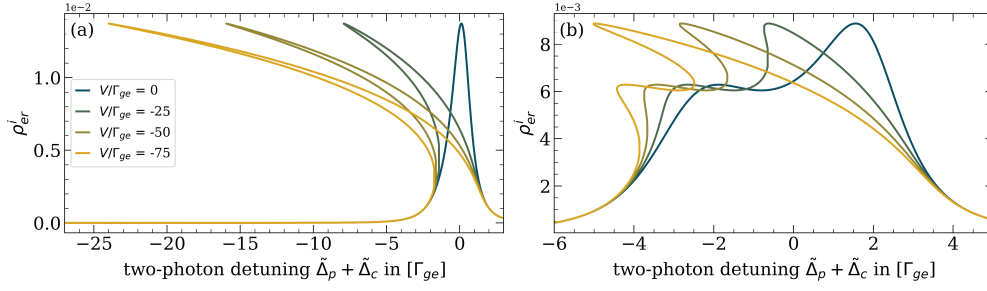


**Fig. 4.4: Multiple bifurcations in the 3-level model.** For both panels, the system parameters were set to  $\Omega_c/\Gamma_{ge} = 0.5$ ,  $\tilde{\Delta}_p/\Gamma_{ge} = -0.75$ ,  $\Gamma_{er}/\Gamma_{ge} = 10^{-5}$ ,  $\Gamma_{gr}/\Gamma_{ge} = 10^{-2}$  and  $n = 3$ . The probe Rabi frequencies are  $\Omega_p/\Gamma_{ge} = 2$  in (a) and  $\Omega_p/\Gamma_{ge} = 5$  in (b) while the interaction strength  $V/\Gamma_{ge}$  is varied identically between 0 and -75 in both plots. In (b), the strong probe Rabi frequency leads to dressed states but with different weights due to the intermediate state detuning  $\tilde{\Delta}_p \neq 0$ .

with  $X = \{4n + 1, 3n + 1, 2n + 1, 2n, n + 1, n, 1, 0\}$ . Due to the complexity of the expressions defining the coefficients  $\alpha_k$  we have calculated the steady states of system 4.12 numerically by finding the roots of  $\mathcal{P}(\rho_{er}^i) = 0$  via the companion matrix. For all parameter regimes tested, there has always been a minimum of one real, positive solution. Additionally, all steady state solutions obtained from the polynomial (4.13) have satisfied the requirement  $0 \leq \rho_{gg}^r, \rho_{ee}^r, \rho_{rr}^r \leq 1$ . The resulting steady state solutions can therefore be interpreted as physical and the populations  $\rho_{jj}$  as state probabilities since the trace condition was initially used as a constraint on the system.

In the parameter regimes that have been studied numerically, we can therefore state that this approach always returns at least one physical solution and, applying Descartes' rule of signs, we can additionally state that the number of real, positive solutions cannot exceed seven. The case  $n = 0$  obviously returns a single steady state solution for any set of external parameters. For other values of  $n \in \mathbb{N}_+$ , up to five steady states have been observed for certain values of the system parameters  $\{\Omega_x, \Delta_x, V, \Gamma_{ij}\}$ .

An example for the onset of bistability with increasing interaction strength  $V$  is shown in Figure 4.4 (a). The steady states for the same parameters but with a stronger probe Rabi frequency  $\Omega_p$  is shown in Figure 4.4 (b). Here, the strong probe leads to formation of dressed states as one can see in the steady state response of system (4.12). For large interaction strengths  $V$ , this can produce up to five steady states for one set of external parameters  $\{\Omega_x, \Delta_x, V, \Gamma_{ij}\}$ .

The observation of bifurcations in the model immediately invokes the question of the stability of the resulting steady states. When studying the two-level model we had observed that regions of multiple steady states produce stable and unstable solutions. A similar behaviour is observed in the three-level model, but the stability of the steady states now shows a more complex behaviour.

Figure 4.5 shows two situations where bifurcations occur. For the set of system parameters chosen in 4.5 (a), the resulting bifurcation leads to the central steady state being unstable since one eigenvalue has a positive real part. This is also the case for the set of parameters chosen for 4.5 (b). However, the 'upper' steady state undergoes an additional bifurcation where a complex conjugate pair of eigenvalues crosses the imaginary axis upon change of the bifur-

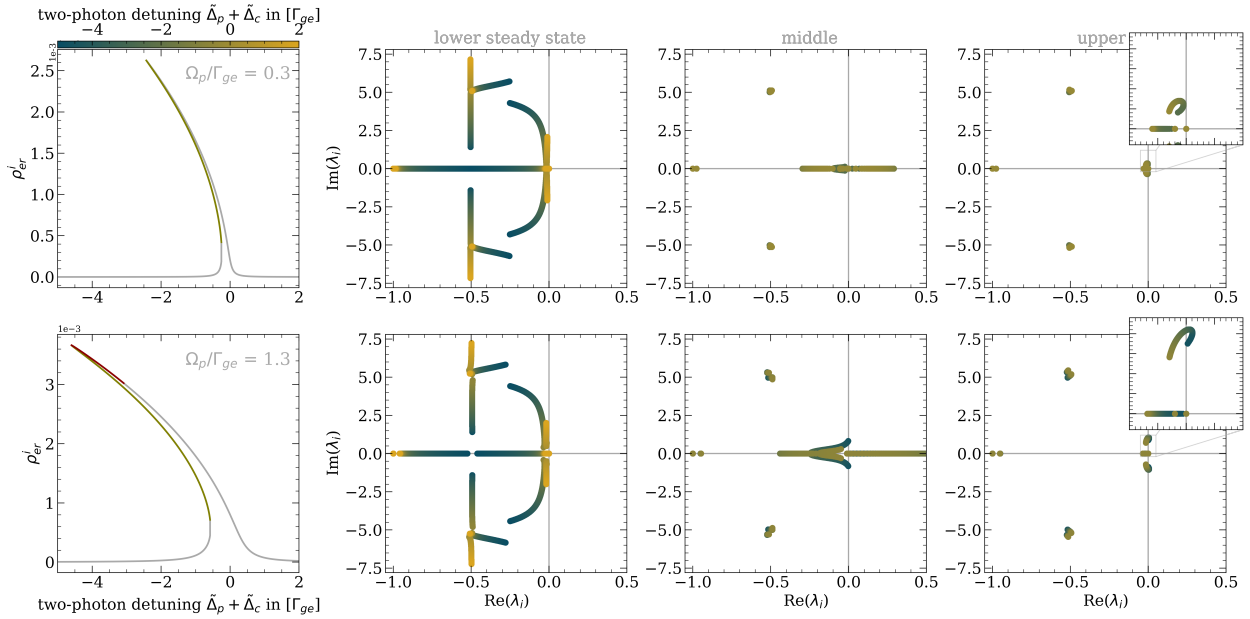


**Fig. 4.5: Hopf bifurcation in the 3-level model.** The steady states and corresponding eigenvalues  $\lambda_i$  of the three-level system are shown for  $\Omega_c/\Gamma_{ge} = 1.5$ ,  $\tilde{\Delta}_p/\Gamma_{ge} = -5$ ,  $V/\Gamma_{ge} = -15$ ,  $\Gamma_{er}/\Gamma_{ge} = 10^{-5}$ ,  $\Gamma_{gr}/\Gamma_{ge} = 10^{-2}$  and  $n = 2$ . The top row corresponds to  $\Omega_p/\Gamma_{ge} = 0.3$  while the bottom row shows the situation for  $\Omega_p/\Gamma_{ge} = 1.3$ . In the spectra shown in the left column, the unstable (middle) steady state is indicated in olive while the limit cycle region is marked in dark red. The three panels on the right show the eigenvalues of the linearisation corresponding to the respective steady states.

cation parameter  $\tilde{\Delta}_c$ . Such a type of bifurcation is known as a Hopf bifurcation which can lead to the formation of limit cycles, giving rise to curious dynamics of the system. An example for such a case where system (4.12) is globally attracted to a stable limit cycle for any initial state  $|\Psi\rangle_{t=0} = (1-x)|g\rangle + x|r\rangle$  is shown in Figure 4.6.

It is a well-known result from theoretical research in the context of (open) quantum systems that nonlinear systems can approach limit cycles [130, 131] within certain parameter regimes. These self-oscillations are nowadays understood as a possible manifestation of the nonlinearity of a system. Famous examples for the occurrence of limit cycles in very different contexts are the Lotka-Volterra model [132, 133] and the van der Pol oscillator [134]. Other interesting objects, such as the Mandelbrot set, are also connected to bifurcation theory.

#### 4.2.4 HOPF BIFURCATION

As mentioned before, a bifurcation occurs when the number or nature of the steady state solutions change upon variation of the bifurcation parameter. In the two-level model, we have encountered saddle-node bifurcations which occurred when the number of steady state solutions changed between one and three. Such bifurcations are often encountered in systems displaying hysteresis effects. Saddle-node bifurcations also occur in the three-level model, as can be seen in the figures above and is also shown explicitly in Figure 4.8.

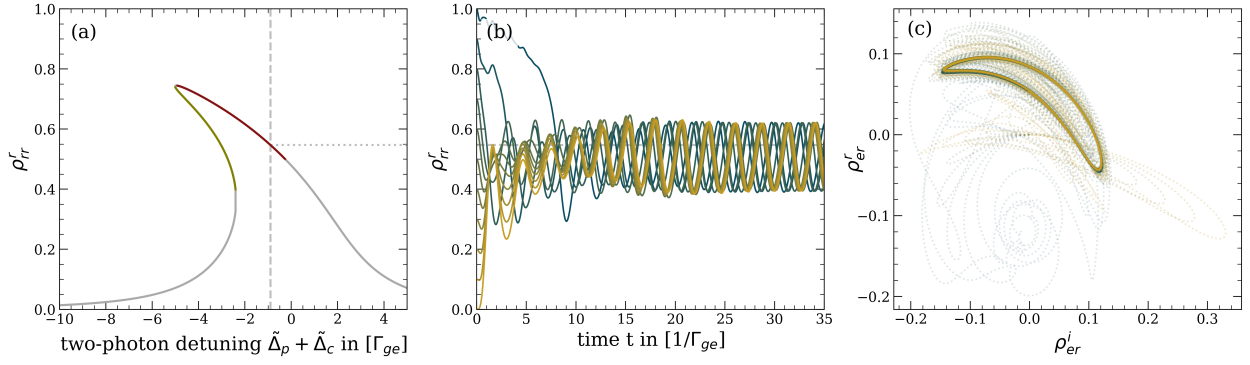


**Fig. 4.6: Limit cycles in the 3-level model.** The spectrum in (a) shows the unstable steady state in olive and the limit cycle region in dark red. (b) shows the attraction of the system towards the limit cycle for the two-photon detuning  $\tilde{\Delta}/\Gamma_{ge} = -0.9$  and different initial state preparations  $|\Psi\rangle_{t=0} = (1-x)|g\rangle + x|r\rangle$  with  $x \in [0, 1]$ . The coherence  $\rho_{er}$  corresponding to the time traces from (b) is shown in (c). All traces approach the same limit cycle after a short time, though with a relative offset in time. The system parameters are set to  $\Omega_p/\Gamma_{ge} = 3.8$ ,  $\Omega_c/\Gamma_{ge} = 2$ ,  $\tilde{\Delta}_p/\Gamma_{ge} = 0$ ,  $\Gamma_{er}/\Gamma_{ge} = 10^{-5}$  and  $\Gamma_{gr}/\Gamma_{ge} = 10^{-2}$ ,  $V/\Gamma_{ge} = -12$  and  $n = 3$ .

However, the interesting additional feature of the three-level system is that one also finds a different type of bifurcation in the model, the aforementioned Hopf bifurcation. Such a Hopf bifurcation features a complex conjugate pair of eigenvalues  $\lambda_j$  of the linearisation<sup>13</sup>  $J_\mu$  crossing the imaginary axis<sup>14</sup> upon variation of the bifurcation parameter, as shown in Figure 4.5. This immediately implies that the corresponding steady state becomes unstable, but the limit cycle branching off at a Hopf bifurcation point may be stable or unstable. In the case of limit cycles, stable means that all trajectories within a neighbourhood of the limit cycle stay in the neighbourhood of the limit cycle as time tends towards infinity, or even converge to it. Therefore, a stable limit cycle is yet another example for an attractor in a dynamical system - similar to a Lyapunov stable steady state. One can depict the unstable limit cycle as repelling trajectories in its neighborhood. This is not the mathematical definition of unstable limit cycles but it serves as an intuitive picture. The stability of a limit cycle can be determined by looking at the sign of the first Lyapunov coefficient, the reader is referred to e.g. [135, 136] for further details.

An example for the limit cycle changing in size and shape upon variation of the bifurcation parameter  $\tilde{\Delta} = \tilde{\Delta}_p + \tilde{\Delta}_c$  is shown in Figure 4.7. The size of the limit cycle increases with growing distance to the bifurcation point  $\zeta_0$ , which lies at that end of the limit cycle region closer to two-photon resonance<sup>15</sup> (yellow). At the far end (blue) of the region indicated in the steady state plot, the limit cycle becomes very large and eventually loses stability. In the bistable region of

<sup>13</sup>The linearisation  $J_\mu$  evaluated at the equilibrium point  $x_0(\zeta)$ , which depends continuously on the bifurcation parameter  $\zeta$ .

<sup>14</sup>The Hartman-Grobman theorem is not applicable at the Hopf bifurcation point itself. However, except for the set of Hopf bifurcation points the theorem applies and one can study the stability of the linearisation to give statements on the stability of the nonlinear system in a neighbourhood of the equilibrium point.

<sup>15</sup>This is one of many indicators that the Hopf bifurcations are subcritical for  $V < 0$ . One can further determine whether a Hopf bifurcation is sub- or supercritical by considering a quantity called the first Lyapunov coefficient [136].

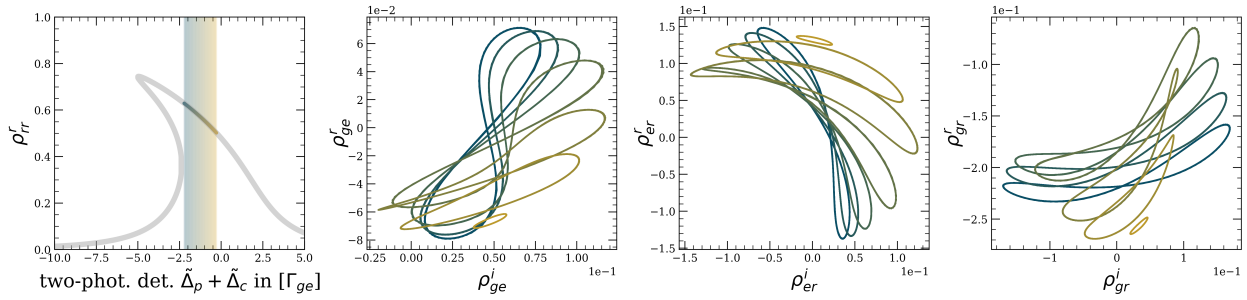


**Fig. 4.7: Shape of limit cycles for variation of the bifurcation parameter.** The limit cycles approached by system (4.12) is shown in slices of the system's phase space for different two-photon detunings  $\tilde{\Delta}/\Gamma_{ge}$ . The spectrum on the left shows the steady state solutions in gray and the limit cycle region shaded by colour. For different detunings, coded by colour as in the spectrum, the limit cycles are shown in phase space slices for the coherences  $\rho_{ge}$ ,  $\rho_{er}$  and  $\rho_{gr}$ . The system parameters are the same as in Figure 4.6.

this example, the lower steady states are asymptotically stable, the middle branch consists of unstable steady states and the upper branch is similarly unstable, including the corresponding limit cycles. However, it is not always the case that the limit cycles are unstable within the bistable/multistable region of the model.

It should be stressed that a limit cycle is not in any form an oscillation between the stable steady states of a system for multiple steady states. Instead, for a limit cycle to occur, a steady state must lose stability and from this steady state value a limit cycle branches off at the bifurcation point. The limit cycle is separate from any other steady states in the system, which is also why globally attractive limit cycles can exist as the only attractors in a system.

Physically, a limit cycle corresponds to self-oscillations of a system without an external, periodic drive. Only by virtue of the system's nonlinearity it is attracted toward a time-periodic orbit that is robust to small fluctuations of the system parameters<sup>16</sup>. The important point to highlight here is the absence of periodicity in the drive, so the time-periodic response of the system is not enforced on the system from the outside by an applied force but emerges fundamentally from the nonlinearity of the system.

Hopf bifurcations are the mechanism behind the emergence of self-oscillations in the three-level model. In the next section, the behavior of the limit cycle region and the resulting orbits is presented in some detail.

#### 4.2.5 BEHAVIOR OF THE LIMIT CYCLE REGION IN THE 3-LEVEL MODEL

As we have seen in the previous sections, the 3-level model shows interesting behavior and has properties which the simplified, effective 2-level model does not have. Due to the lack of analytical expressions for the 3-level approach, no equations were derived for the onset of the bistable or limit cycle regions. However, some interesting properties of the 3-level model will be shown to motivate a further study of this model.

<sup>16</sup>This robustness to small fluctuations in the system parameters is highly relevant for actual experimental observations of self-oscillations in the response of a system!

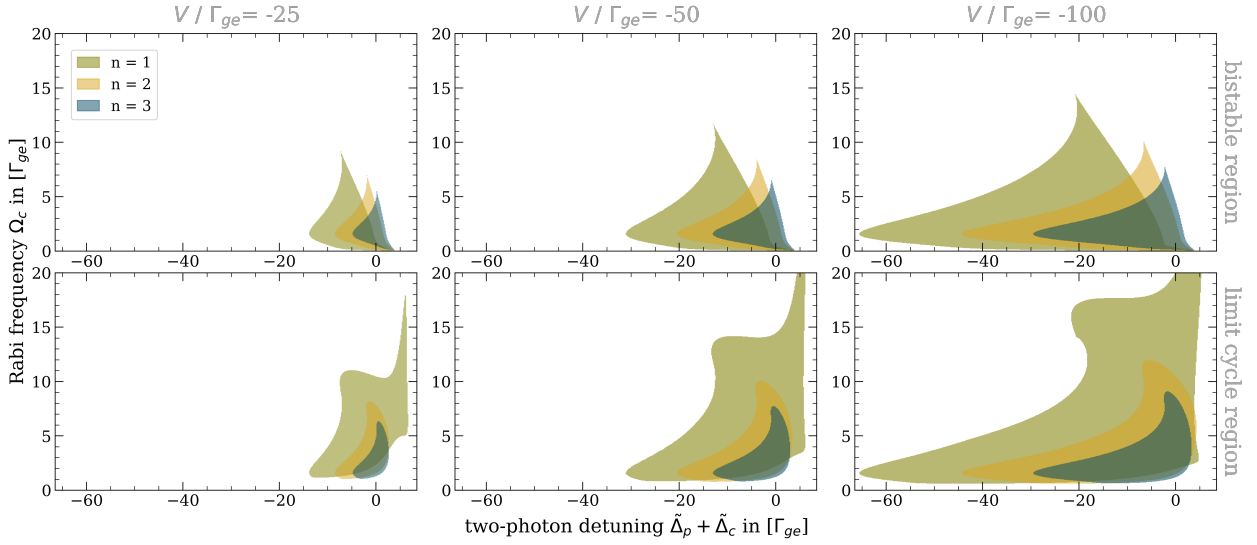


**Fig. 4.8: Scaling of bistable and limit cycle regions in the 3-level model.** For increasing coupling Rabi frequencies  $\Omega_c$ , the bistable/multistable region (top row) and limit cycle region (bottom row) is shown for power law scalings  $n \in [1, 2, 3]$  and interaction strengths  $V/\Gamma_{ge} \in [-25, -50, -100]$ . The remaining system parameters are set to  $\Omega_p/\Gamma_{ge} = 3$ ,  $\tilde{\Delta}_p/\Gamma_{ge} = -3.5$ ,  $\Gamma_{er}/\Gamma_{ge} = 10^{-5}$  and  $\Gamma_{gr}/\Gamma_{ge} = 10^{-2}$ .

Firstly, it is interesting to have a look at the onset of the bistable and the limit cycle regions, respectively. Figure 4.8 exemplarily shows the scaling of those regions for various interaction strengths, with all other parameters held constant. One can see that both regions grow in size with increasing interaction strength  $V/\Gamma_{ge}$ , but remain somewhat similar in shape. The onset of bistability and limit cycles depends on the interaction strength. For increasing  $V$  the onset of either bifurcation is observed at lower coupling Rabi frequencies  $\Omega_c$  for fixed probe Rabi frequencies  $\Omega_p$ . Additionally, the onset of bistability occurs for lower coupling Rabi frequencies than the onset of limit cycle formation. These two observations have been made throughout for every set of system parameters that were tested<sup>17</sup>.

Furthermore, it has been observed that the limit cycle is stable and globally attractive where the limit cycle region does not overlap with the multistable region. In case of an overlap of the two bifurcations, the limit cycle is no longer globally attractive and tends to loose stability further away from the Hopf bifurcation point. Also, the size of the limit cycle grows and its period reduces with increasing distance to the bifurcation point  $\zeta_0$ .

It was also found that several Hopf bifurcations can occur upon variation of the bifurcation parameter  $\tilde{\Delta}_c$ . An example for such a scenario is shown in Figure 4.9 where the steady state values for  $\rho_{rr}^x$  are shown in (a). The eigenvalues, plotted in panel (b), show very clearly that the two Hopf bifurcations on the lower branch (teal) are caused by different pairs of eigenvalues crossing the imaginary axis. Only the set of limit cycles closer to zero detuning is stable. The

<sup>17</sup>It should be noted that the model was investigated only for  $n \in \mathbb{N}_+$  for reasons of implementation of the root-finding algorithm for the polynomial defining the steady states of the system. The behavior of the model for non-integer power law scalings in  $n$  or, more interestingly, for negative  $n$ , may be quite different.

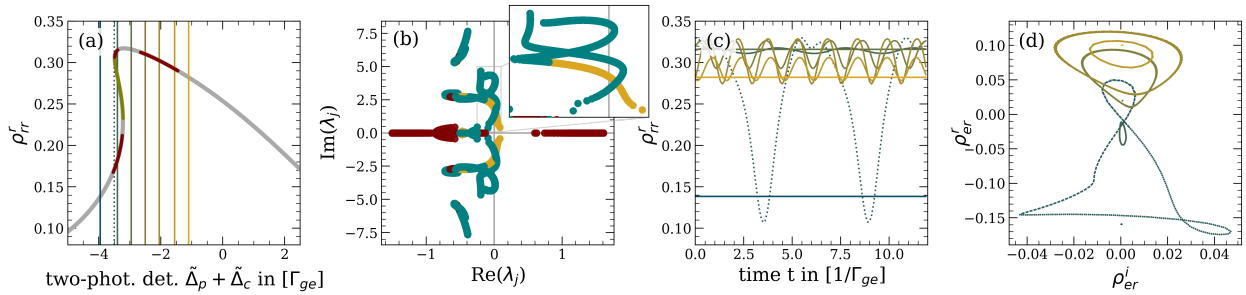


**Fig. 4.9: Two separate spectral regions with globally attractive limit cycles.** The steady state values for  $\rho_{rr}^r$  are shown in (a), red indicates limit cycle regions and olive an unstable steady state. The eigenvalues of the linearisation corresponding to the lower (teal), middle (red) and upper (yellow) branch are shown in (b). Panel (c) shows the long-term trajectories of the system for the detunings  $\tilde{\Delta} = \tilde{\Delta}_p + \tilde{\Delta}_c$  indicated in (a). The same trajectories are represented in (d) in the space spanned by the coherence  $\rho_{er}$ . The system parameters are set to  $\Omega_p/\Gamma_{ge} = 3$ ,  $\Omega_c/\Gamma_{ge} = 4.4$ ,  $\tilde{\Delta}_p/\Gamma_{ge} = 0$ ,  $V/\Gamma_{ge} = -100$ ,  $n = 3$ ,  $\Gamma_{er}/\Gamma_{ge} = 10^{-5}$  and  $\Gamma_{gr}/\Gamma_{ge} = 10^{-2}$ .

limit cycle branching off where the eigenvalues shown in yellow cross the imaginary axis are stable as well. The time traces in (c) also show that both separate limit cycle regions are stable, and in this example even globally attractive at their respective detunings  $\tilde{\Delta}$ . Here, the third limit cycle region on the lower branch is unstable. The dotted line shows a trace from the limit of the region of stable orbits for the second stable limit cycle region.

This example shows that for different detunings  $\tilde{\Delta}$  one can obtain spectrally separate regions of globally attractive limit cycles for certain system parameters. However, in most cases with several limit cycle regions it has been observed that at most one region produces stable limit cycles.

Lastly, it is interesting to have a closer look at the limit cycles themselves. Figure 4.10 shows how the period of the limit cycle, as well as their shape, changes across the region of stable limit cycles. Near the Hopf bifurcation, the trajectory is smaller and the period is shorter as expected from bifurcation theory [127]. As can also be seen in Figure 4.9, the limit cycles become more complicated and take on complex shapes before they lose stability, which can be seen in the orbit shapes as well as in the time-dependent behavior of the coherences.

### 4.3 SCALING OF INTERACTION TERM

So far, the models have been studied as they are, i.e. without justifying a particular choice for the power law scaling  $n$  of the population-dependent detuning<sup>18</sup>  $V \cdot (\rho_{xx}^n$ . We aim at modelling a system that is known to interact via Rydberg-Rydberg interactions and may be ionised such that a plasma forms around the atoms, causing a Stark shift-induced backaction on the Rydberg state.

<sup>18</sup>With  $\rho_{xx}$  we denote the population of the level highest in the ladder, i.e.  $x = e$  for the two-level model and  $x = r$  for the three-level model. In this section we will describe the three-level model - but the interaction scaling approximation works identical for the two-level model.

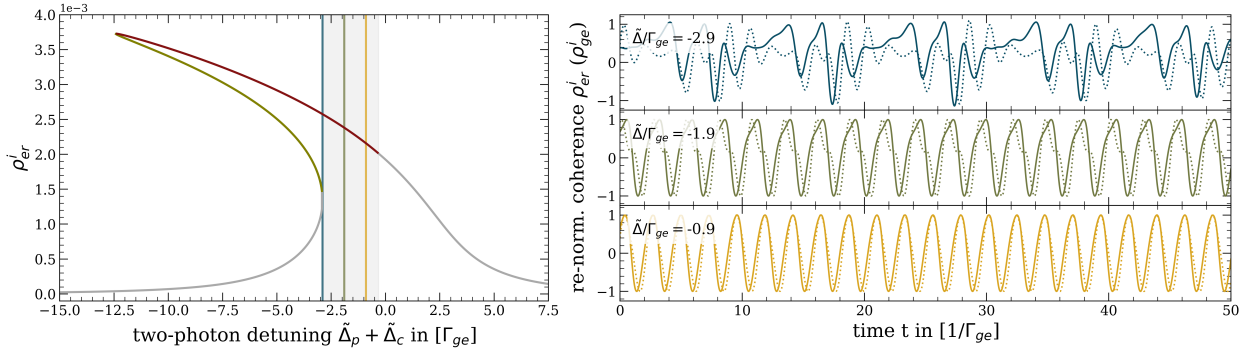


**Fig. 4.10: Temporal shape of limit cycle at different detunings.** The temporal shape of the limit cycles approached by system (4.12) is shown for different two-photon detunings  $\tilde{\Delta}/\Gamma_{ge}$ . The spectrum on the left shows the unstable steady state in olive and the limit cycle region in dark red. The region shaded in gray is the spectral region where the limit cycles are stable. For the three detunings indicated in the spectrum, the renormalised coherence  $\rho_{er}^i$  (solid) and  $\rho_{ge}^i$  (dotted) are plotted over time. The system parameters are set to  $\Omega_p/\Gamma_{ge} = 3.8$ ,  $\Omega_c/\Gamma_{ge} = 2$ ,  $\tilde{\Delta}_p/\Gamma_{ge} = 0$ ,  $V/\Gamma_{ge} = -30$ ,  $n = 3$ ,  $\Gamma_{er}/\Gamma_{ge} = 10^{-5}$  and  $\Gamma_{gr}/\Gamma_{ge} = 10^{-2}$ .

We will start by considering Rydberg-Rydberg interactions in the van der Waals regime. The corresponding many-body interaction Hamiltonian features an atom-atom interaction scaling with interatomic distance as  $r_{kl}^{-6}$  for a pair of atoms  $(k, l)$ , and is given by

$$\mathcal{H}_{int.}^{(k)} = -\frac{\hbar}{2} \sum_{l \neq k} \frac{C_6^{(k,l)}}{r_{kl}^6} |r\rangle_{kk} \langle r| \otimes |r\rangle_{ll} \langle r|. \quad (4.14)$$

From the derivation presented in Appendix B we know that the interaction Hamiltonian can be approximated<sup>19</sup> by the expression

$$\mathcal{H}_{int.}^{vdW} = -\frac{4\pi\rho_v}{3} I_{(\theta,\phi)} \sqrt{\hbar\Omega C_6} \rho_{rr}^2 |r\rangle \langle r| \quad (4.15)$$

to arrive at effective single-body equations of motion.

Therefore, to model van der Waals interactions between Rydberg atoms in the vapour, one sets  $n = 2$  and  $V = \frac{4\pi\rho_v}{3} I_{(\theta,\phi)} \sqrt{\hbar\Omega C_6}$ . For simplicity, one can assume the Rydberg-Rydberg interaction to be isotropic which sets  $I_{(\theta,\phi)} = 4\pi$ . The three-level model then follows directly from the above approximation of the many-body Hamiltonian for van der Waals interactions.

If, on the other hand, the dynamics of the level shifts in the vapour are dominated by Stark shifts of the Rydberg state due to collisional ionisation of Rydberg atoms, the power law scaling was shown in Appendix C to be given by  $n = 4/3$  for sufficiently low Rydberg populations. The Stark shift results in a scaling  $V \propto -\alpha \mathcal{N}_{tot}^{4/3} (\rho_{rr}^r)^{4/3}$ .

<sup>19</sup>The assumptions made in the approximation in Appendix B are that of a mean field model, therefore neglecting direct two-body correlations or entanglement, and secondly the assumption of similarity of all atoms, meaning that - statistically - the situation will be the same for whichever atom in the ensemble, allowing to reduce the many-body case to a set of single-body equations of motion.

With these motivations for a  $\rho_{rr}$ -dependent power law scaling of the Rydberg state detuning, we can now consider the additional complications arising from the motion of the atoms. This leads us to a full hot vapour simulation of the Rydberg system.

#### 4.4 HOT VAPOUR SIMULATION FOR ALL VELOCITY CLASSES

So far, we have been looking at a single velocity class  $\mathbf{v}_i$  and how the atoms within this velocity class interact with one another via Rydberg density-dependent interactions. The resulting dynamics within this velocity class strongly depend on the detuning of the atoms from the intermediate and Rydberg states, as well as on the other system parameters.

However, assuming only a single velocity class must fail in the description of a hot vapour. As an example, the thermal energy of a rubidium atom at 1 K corresponds to a kinetic energy which is equivalent to  $v \approx 14$  m/s. At 780 nm - the wavelength of the Rb  $D_2$  line - this is equal to a detuning of  $\Delta \approx 18$  MHz, which is roughly half the natural linewidth of the transition. This is very much.

Therefore, if one wants to simulate a hot vapour it becomes necessary to take the full range of velocity classes of the atoms in the vapour into account. Furthermore, one has to deal with the additional complication that all velocity classes interact with one another through the shared Rydberg-Rydberg interaction and all feel the same plasma bath. Single velocity classes can no longer be treated as separate entities but have to be regarded as part of one vapour composed of many different velocity classes, all acting under the influence of a shared Rydberg atom density. To include this shared interaction, it does not suffice to just look at many velocity classes and sum over their weighted response over time. An analytical treatment of the problem now results in a set of integro-differential equations which are harder to deal with as compared to standard ODEs. The system is therefore studied numerically with an adapted integration scheme. In order to account for the resulting dynamics of the entire vapour one has to include the Rydberg-density dependent level shift in every integration step. This implies that standard integration schemes are unsuitable and have to be modified for this purpose.

To this end, we have implemented a stepwise Runge-Kutta integrator<sup>20</sup> in a matrix-based fashion in python. The equations of motion (4.12) were written in the form

$$\rho_{\{v_i\}}(t_{j+1}) = \mathcal{M}_{\{v_i\}}(\rho_{\{v_i\}}(t_j)) \cdot \rho_{\{v_i\}}(t_j)$$

with  $\mathcal{M}_{\{v_i\}}(\rho_{\{v_i\}}(t_j)) \in \mathbb{R}^{(9,9,N_{vel})}$  and  $\rho_{\{v_i\}}(t_j) \in \mathbb{R}^{(9,N_{vel})}$ <sup>21</sup>.  $N_{vel}$  denotes the number of velocity classes in the velocity class<sup>22</sup> partition  $\{v_i\}_i$  with respective velocity class weights  $\{p(v_i)\}_i$  and bin width  $\{\Delta v_i\}_i$ . The matrix  $\mathcal{M}_{\{v_i\}}(\rho(t_j))$  depends on the detunings specific for every velocity class  $v_k \in \{v_i\}_i$  and on the weighted Rydberg state population in the vapour at time  $t_j$ , and therefore has to be updated for every time step  $t_j \rightarrow t_{j+1}$ . For  $N_{vel}$  velocity classes the Rydberg-density dependent level shift  $\Delta_{shift}(t_j)$  has to be adjusted by taking the weighted sum over all velocity classes.

<sup>20</sup>Runge-Kutta 4 (rk4), [137].

<sup>21</sup>This uses the fact that  $\rho_{jj}^i = 0$ . An implementation including the imaginary part of the populations is also possible, but unnecessary and computationally more expensive.

<sup>22</sup>Throughout the remainder of the thesis we will assume that probe and coupling laser are propagating in one dimension, i.e. are co- or counterpropagating, such that only one spatial degree of freedom is of relevance.

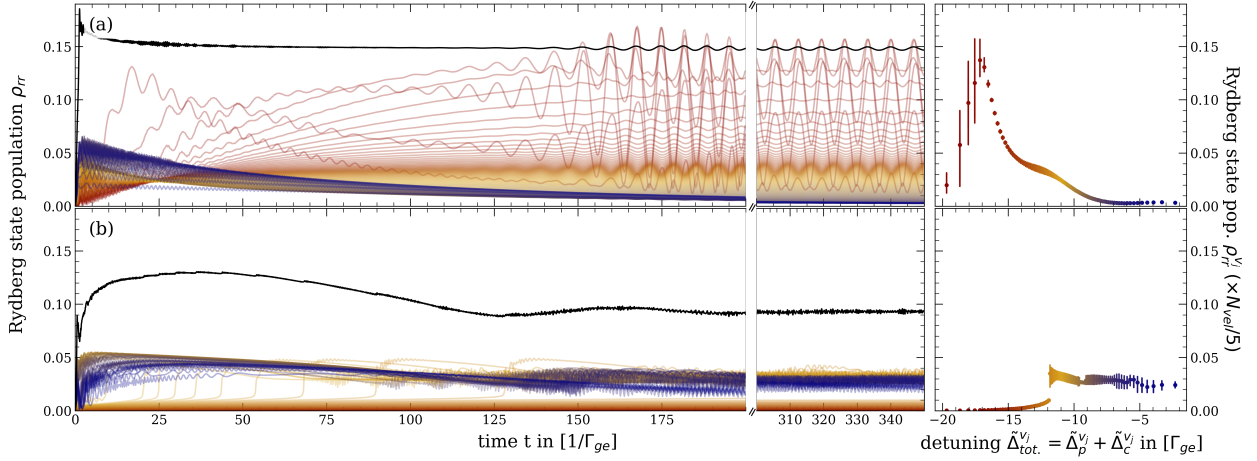


**Fig. 4.11: Thermal vapour simulation leading to time-periodic response.** The time evolution of a system initially in  $|g\rangle^{\otimes N_{vel}}$  is shown for the case of a vapour with velocity classes interacting via the shared Rydberg atom density (upper row, a) and a vapour composed of self-interacting velocity classes (lower row, b). The system parameters are  $\Omega_p = 6\Gamma_{ge}$ ,  $\Omega_c = 4\Gamma_{ge}$ ,  $\Delta_p = 0$ ,  $\Delta_c = -11\Gamma_{ge}$ ,  $\Gamma_{er} = 10^{-6}\Gamma_{ge}$ ,  $\Gamma_{gr} = 10^{-3}\Gamma_{ge}$  and  $n = 2$ . The velocity class detunings correspond to a Rb gas at  $T = 48^\circ\text{C}$  with counterpropagating probe and coupling beams at  $\lambda_p = 780$  nm and  $\lambda_c = 480$  nm. The simulation uses  $N_{vel} = 101$  velocity classes with equal population weight, shown in colour in all plots and rescaling by  $(\times N_{vel}/5)$ . The solid black line shows the total vapour response.

As a result, one obtains the time evolution of the  $9 \times N_{vel}$ -dimensional state vector  $\rho_{\{v_i\}}(t_j)$  which encodes the state vector  $\rho_{\{v_i\}}(t_j)$  for all velocity classes simultaneously<sup>23</sup>.

Figure 4.11 shows an example for an interacting (a) and a noninteracting (b) sample. Noninteracting here means that every velocity class evolves under its own interaction but does not experience the Rydberg density of the other velocity classes. The black solid lines in each panel shows the resulting Rydberg state population integrated over all velocity classes. As one can see, the resulting behavior of the two cases is significantly different. In the noninteracting case, some velocity class approach limit cycles, but each with its own frequency and phase. The re-

<sup>23</sup>This integration scheme is slow for large numbers of velocity classes and long timescales, making it a bit inconvenient to use. To properly simulate a thermal vapour,  $N_{vel} \sim \mathcal{O}(100)$  are usually required. For a linear spacing of velocity classes in  $\{v_i\}$  and large probe and coupling Rabi frequencies on the order of  $\Gamma_{ge}$ , around  $N_{vel} \approx 300 - 500$  velocity classes are required. If one chooses a spacing linear in the velocity class populations  $\{p(v)\}$ , this number reduces to  $N_{vel} \approx 100 - 200$ . To further speed up the code, one can employ additional tricks such as the introduction of a cutoff weighted Rydberg state population at cutoff time  $t_c$ . All velocity classes with weighted Rydberg populations below the bar are regarded as contributing insignificantly and taken to be constant for future integration steps. This reduces the computational costs of a single integration step and is effective particularly for cases of many noncontributing velocity classes. Overall, the time required to run a single integration can be sped up by more than one order of magnitude, bringing computation times down to  $\ll 1$  minute per run while keeping deviations from the full thermal vapour integration negligibly small. An implementation of adaptive step size Runge-Kutta integrations with Fehlberg (RK45) [138] and Dormand-Prince (RKDP) [139] pairs has been trialled as well. However, the additional function evaluations and calculations required for the error estimate have slowed the evaluations more than an adaption of step size has sped it up for the parameter range of interest.

sulting Rydberg state population of the vapour therefore does not show any distinctive oscillatory feature due to the averaging over all velocity classes.

If the velocity classes interact with one another through the shared Rydberg density as in Figure 4.11 (a), one observes a very different behavior. Some velocity classes initially begin to oscillate at their own frequencies, but after some time the velocity classes eventually oscillate in lockstep with each other at a single frequency. This behaviour is known as synchronisation and is briefly discussed in Section 4.4.1 below. It is noteworthy that the frequency of the resulting oscillations are orders of magnitude different than the laser Rabi frequencies or interaction strength. In this example, the oscillation frequency  $\omega_{osc}$  is smaller than  $\Gamma_{ge}$ , but it holds that  $\Omega_p, \Omega_c > \Gamma_{ge}$  and  $V \gg \Gamma_{ge}$ . It is therefore very obvious that the oscillation phenomenon arises fundamentally from the system properties rather than being imprinted on the system by some external drive or force.

#### 4.4.1 SYNCHRONISATION

It has been observed in Figure 4.11 (a) that some velocity classes initially begin to oscillate at their own natural frequency  $\omega(\mathbf{v}_j)$ . After a transient phase the populations begin to oscillate in lockstep with a fixed phase relation to each other, leading to macroscopic oscillations in the hot vapour's bulk quantities. This effect can be understood in the framework of synchronisation, which is described in detail in e.g. [140].

Synchronisation is a process that can occur between self-oscillating systems<sup>24</sup> where the phase, frequency and/or amplitude of the self-sustained oscillators are adjusted towards synchrony. Mechanisms for synchronisation can either be a direct coupling between self-oscillating systems or coupling via an external force, e.g. the day-night cycle on planet earth forcing most people to adapt a 24 h rhythm even though individual circadian rhythms vary. The nature and directionality of this coupling may vary, which leads to the observation of different forms of synchronisation.

In systems like the hot vapour model considered above, one finds a scenario where many self-sustained phase oscillators with slightly different natural frequencies  $\omega(\mathbf{v}_j)$  are coupled via a global<sup>25</sup> mean field. This mean field is, of course, the total Rydberg atom population  $\rho_{rr}^r$  of the vapour and is composed of the Rydberg populations of all velocity classes. It leads to backaction on the Rydberg state by Rydberg population-dependent level shifts. The oscillation of the mean field therefore arises from the oscillation in Rydberg population due to some velocity classes being attracted towards limit cycles, i.e. self-oscillating states. It maintains the periodicity by enforcing a synchronisation of the oscillations within the ensemble of velocity classes via global coupling by a periodic shift in Rydberg state energy.

<sup>24</sup>It is crucial here that the system is self-oscillating rather than driven by an external force. If the system were driven externally, then the phase of the system (i.e. the position on the limit cycle at a given time  $t$ ) is locked onto the phase of the external drive. This makes phase synchronisation impossible as two driven oscillators cannot adjust their phases to oscillate in synchrony. Self-oscillating systems, on the other hand, are not forced into any given phase on the limit cycle at a given time such that the phase can easily be adjusted by a coupling or a force. It should also be mentioned, again, that self-oscillation is a feature of some nonlinear systems.

<sup>25</sup>Since the atoms in the different velocity classes should, on average, be distributed uniformly across the vapour one may assume that the contribution of a single velocity class to the mean field depends only on the amplitude of the velocity class's population and is global.

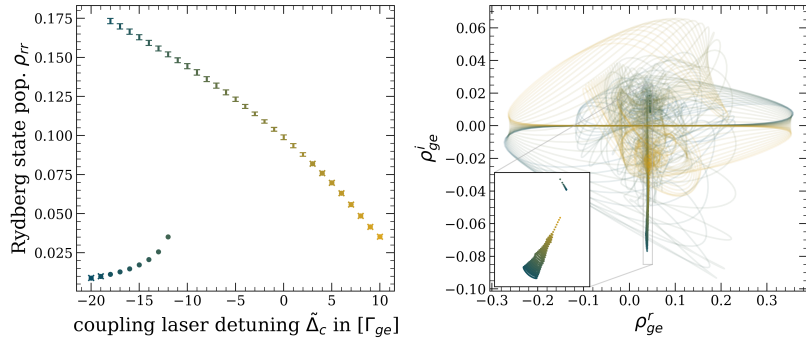


**Fig. 4.12: Local and global attractiveness of the hot vapour system.** The steady states and limit cycles approached by the thermal vapour system are shown for the initial states  $|g\rangle^{\otimes N_{vel}}(\cdot)$  and  $|e\rangle^{\otimes N_{vel}}(\mathbf{x})$ . Error bars indicate the oscillation amplitude. The time evolution of the hot vapour system is shown in the  $\rho_{ge}$ -space in the right panel and the resulting limit cycles in the inset. System parameters are the same as in Figure 4.11, except for the coupling laser detuning  $\Delta_c/\Gamma_{ge}$  being varied in the range  $[-20, 10]$ .

Examples of globally coupled phase oscillators have been studied in abundance in recent years, starting with the works of Winfree [11] and Kuramoto [12]. The list of systems stretches from coupled laser arrays [141–143] and Josephson junctions [144] to the synchronous flashing of fireflies [3] and the synchronisation of the chirps of snowy tree crickets [145].

Interesting to note is that several other effects can take place within the framework of synchronisation. For instance, in certain parameter regimes it is possible that only a subset of phase oscillators synchronises, which is known as partial synchronisation [4, 5, 146]. Also, for inhomogeneous global coupling where the coupling strength depends on e.g. the spatial separation between oscillators, clustering of synchronised oscillators can occur. This means that the oscillators within a cluster are synchronised, but the different clusters may have different oscillation frequencies [140].

Therefore, the naïvely rather unexpected occurrence of macroscopic oscillations in the hot vapour simulation arises from synchronisation of the initially independent oscillations of the Rydberg population of some velocity classes, mediated via global coupling through the vapour’s Rydberg atom density. Certain conditions must be met for the occurrence of synchronisation [4, 140]. This leads to the onset of a self-sustained oscillatory phase in the vapour without external periodic forcing or driving. Important is the realisation that the synchronised oscillations do not decay away in time but would continue perpetually.

#### 4.4.2 BEHAVIOUR OF THE LIMIT CYCLE REGION IN HOT VAPOUR SIMULATIONS

Using the full hot vapour integration scheme, one can now study the resulting behavior of the system<sup>26</sup>, from lineshapes to the occurrence of pronounced population oscillations.

<sup>26</sup>It tends to be a little difficult to find an oscillation regime in the hot vapour when not knowing where to look. It turned out that the hot vapour simulation tends to be in a synchronised phase if the stationary single velocity class model with the effective interaction  $V_{eff} = V \cdot (\rho_{rr}^r)^{n-1}$  is in an oscillatory regime. Here,  $\rho_{rr}^r$  denotes the total vapour Rydberg density and has to be estimated.

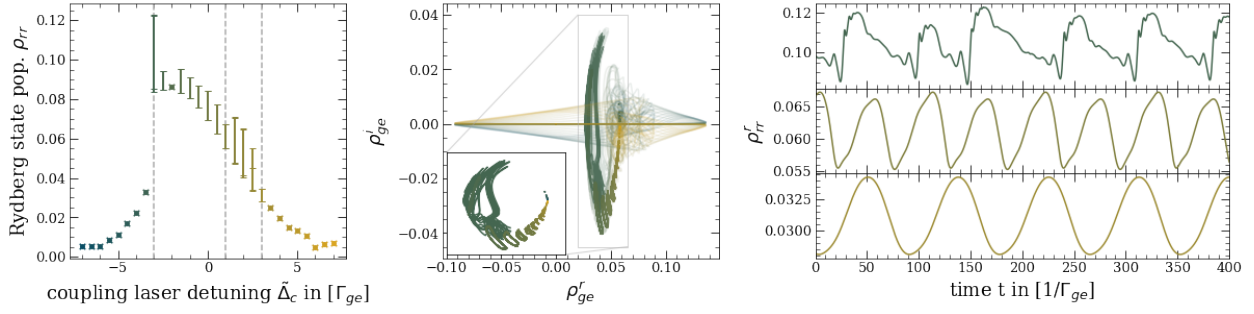


**Fig. 4.13: Example limit cycle shapes in hot vapour system.** The limit cycles approached by the system are shown for the values indicated with gray dashed lines in the spectrum (left). The central plot inset shows the phase space approached by the system for  $t > 4000\Gamma_{ge}^{-1}$ , with the system not approaching either limit cycle or steady state for  $\Delta_c = -3\Gamma_{ge}$  within this integration time. One can clearly see different shapes of the oscillations and also that the oscillation region is interrupted at  $\Delta_c = -2\Gamma_{ge}$ . The system parameters are  $\Omega_p = 1.5\Gamma_{ge}$ ,  $\Omega_c = 1\Gamma_{ge}$ ,  $\Delta_p = 0$ ,  $\Delta_c/\Gamma_{ge} \in [-7, 7]$ ,  $\Gamma_{er} = 10^{-6}\Gamma_{ge}$ ,  $\Gamma_{gr} = 10^{-3}\Gamma_{ge}$ ,  $V = -300$  and  $n = 2$ . The velocity class detunings correspond to a Rb gas at  $T = 48^\circ\text{C}$  with counterpropagating probe and coupling beams at  $\lambda_p = 780\text{ nm}$  and  $\lambda_c = 480\text{ nm}$ . The simulation uses  $N_{vel} = 101$  velocity classes with equal population weight.

The first point to note is that the full hot vapour system equally knows locally and globally attractive solutions, as shown in Figure 4.12. The left panel shows the spectrum when varying the coupling laser detuning across resonance, once with the initial state being  $|g\rangle^{\otimes N_{vel}}$  ( $\cdot$ ) and once for  $|e\rangle^{\otimes N_{vel}}$  ( $\times$ ). The bars indicate the magnitude of the oscillations in Rydberg state population  $\rho_{rr}^r$ , if present. The corresponding temporal evolution towards the steady state or limit cycles is shown in the right plot in the space spanned by  $\rho_{ge}^r$  and  $\rho_{ge}^i$ . The existence of locally and globally attractive states is relevant for modelling experimental sequences such as a coupling laser scan, or when giving statements on the presence of limit cycles at given system parameters.

Similar to the single-velocity case displayed in Figure 4.10, the frequency and shape of the limit cycle in the synchronised state change as one changes the bifurcation parameter  $\tilde{\Delta}_c$ . This is shown in Figure 4.13 where the Rydberg population is shown in time for the three detunings indicated in the spectrum. Additionally, one can see that the limit cycle region is interrupted at  $\tilde{\Delta}_c/\Gamma_{ge} = -1.5$  and does not approach a closed orbit within  $t\Gamma_{ge} < 5000$  for  $\tilde{\Delta}_c/\Gamma_{ge} = -2.5$ . This case is reminiscent of a system near a strange attractor, the orbits are each somewhat similar and appear periodic, but are not perfectly so.

For the same system parameters, Figure 4.14 (a) shows in detail which velocity classes contribute to the oscillations. The colour of the velocity class corresponds to the total detuning from two-photon resonance of the respective velocity class (red: red detuned, yellow: on resonance, blue: blue detuned). One can see that the spectral region where frequency entrainment leads to large relative oscillation amplitudes of the individual velocity classes is very narrow and changes with detuning  $\Delta_c$ . This explains the different limit cycle shapes and frequencies observed in Figure 4.13. In (b), it is shown that for fixed detuning  $\Delta_c/\Gamma_{ge} = 1$  the width of this entrainment region depends on the interaction strength and forms a triangular shape reminiscent of an Arnold tongue. Additionally, the full hot vapour system also preserves ‘knowledge’ of

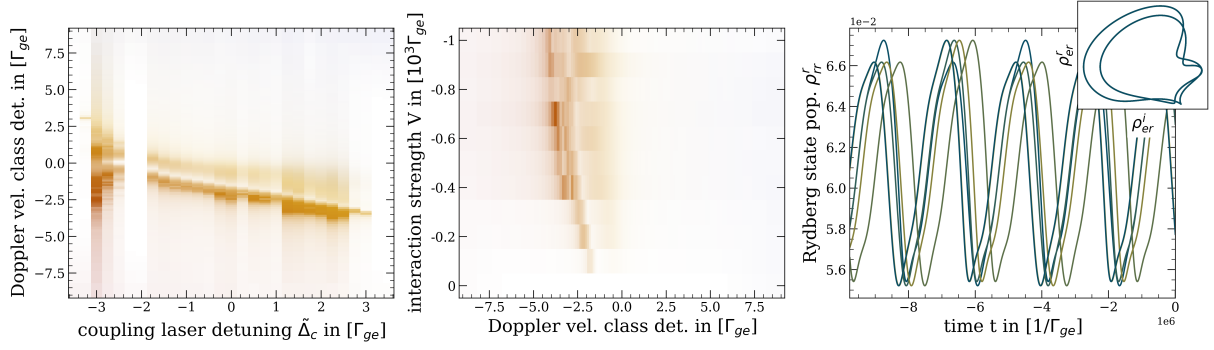


**Fig. 4.14: Contributing velocity classes, oscillation frequency entrainment, and phase freedom in limit cycle of thermal vapour system.** For the same model parameters as in Figure 4.13, the amplitude of the entrained velocity classes relative to the mean value is shown in (a) for the oscillation region. The central plot (b) shows the relative amplitudes of the velocity classes at fixed detuning  $\Delta_c/\Gamma_{ge} = 1$  for varying interaction strengths  $V/\Gamma_{ge} \in [0, -1000]$ . The increase in width of the frequency entrainment region with increasing  $V$  is visible. At the same detuning, (c) shows the limit cycle in  $\rho_{rr}^r$  and in  $\rho_{er}^r$ -space (inset) for different initial  $|\Psi\rangle_{t=0} = (1-x)|g\rangle^{\otimes N_{vel}} + x|e\rangle^{\otimes N_{vel}}$ , demonstrating that the phase in the limit cycle depends on the initial state of the system. ( $x=0$  : blue,  $x=1$  : green)

the initial state as shown in (c) since the phase of the system in the limit cycle depends on the initial state of the system. This behavior is typical for self-oscillating and synchronising systems.

Generally, it was observed that the oscillation frequency increases with increasing Rabi frequencies, and depends rather weakly on the interaction strength  $V$ . No oscillations occur for large ratios of decay rates to Rabi frequencies, i.e. the decay must be sufficiently small to facilitate an oscillation regime. Also, a minimum coupling Rabi frequency must be given for oscillations to occur but this critical value depends on the other system parameters. Synchronisation can occur in regions with equal and different signs of  $V$  and  $\Delta_c$  though the contributing velocity classes, and therefore the amplitude of the oscillations, vary.

Concluding this brief study of the thermal vapour approach it should be noted that the behavior of the system depends strongly on the external parameters<sup>27</sup> as well as on the initial state of the system. Numerical investigations of this system is feasible on standard computers when minimising the computational requirements of the code, allowing an exploration of the system's behavior. It has been shown that the three-level model and the thermal vapour system display rich nonlinear dynamics. We will therefore now turn our attention to the connection of these model systems to already established models and phenomena.

<sup>27</sup>For comparison, in our thermal vapour experiment we routinely work in the following regime:

$\Delta_p = -2\pi \times (140 \text{ MHz})$  [147],  $\Delta_c \in 2\pi \times ([-250, 100] \text{ MHz})$ , peak Rabi frequencies  $\Omega_p \in 2\pi \times ([90, 200] \text{ MHz})$  and  $\Omega_c \in 2\pi \times ([0, 24] \text{ MHz})$  [98] which results in effective 2-photon Rabi frequencies up to  $\Omega_{eff}^{max.} = 2\pi \times (16.4 \text{ MHz})$ .  $\Gamma_{ge} = 2\pi \times (6.07 \text{ MHz})$  [55] is the  $D_2$  line decay rate of  $^{87}\text{Rb}$ ,  $\Gamma_{er} \leq 2\pi \times (5 \text{ kHz})$  due to radiative decay [98], and the decay  $\Gamma_{gr} \approx 2\pi \times (643 \text{ kHz})$  is the sum of Rydberg state lifetime and transit time induced broadening [21]. Temperatures vary in ranges of 35 - 60 deg. Celsius, the van der Waals coefficient  $|C_6| \in [15, 4037] \text{ GHz} (\mu\text{m})^6$  [98] and resulting blockade radii in range  $r_b \in [3.9, 9.5] \mu\text{m}$ . The Rydberg atom fraction  $f_{Ryd.}$  was around the saturation threshold. The coupling laser scan rate is of order 10 GHz/s.

## 4.5 RELATION TO OTHER MODELS, EFFECTS, AND PHENOMENA

The three-level and thermal vapour model, as presented above, and the effects occurring therein, namely self-sustained oscillation and synchronisation, are very interesting to study in their own rights. Additionally, these connect the models to well established phenomena which will briefly be mentioned below. The breaking of ergodicity by multistable classical systems is discussed in Section 4.5.1 and the transition from an equilibrium state to a synchronised state in the hot vapour system is related to generalised Kuramoto models and the nonequilibrium synchronisation transition occurring therein in Section 4.5.3. The closely related phenomenon of time crystals is briefly mentioned in Section 4.5.2.

### 4.5.1 ERGODICITY BREAKING

The ergodic hypothesis, i.e. the assumption that equivalence holds between the time average of a typical trajectory and the ensemble average of the system, is a cornerstone of statistical physics. However, the notion of ergodicity breaking has received much attention since the unexpected finding of Fermi, Pasta, Ulam and Tsinghou (FPUT) in 1955 that a system of a few nonlinearly coupled oscillators on a 1D chain with fixed boundary conditions did not equilibrate within the accessible timescales [148]. On the contrary, the chain showed almost perfect recurrence to the initial state, i.e. (quasi-) periodic motion. This result raised questions on ergodicity and thermalisation in their model, i.e. the relaxation of a far-from-equilibrium state towards equilibrium and the equipartition of energy between the normal modes of the system<sup>28</sup>.

Returning to ergodicity, since the FPUT simulations it has been found that ergodicity breaking occurs in a significant number of classical nonlinear systems [151]. For a classical system with two different attractive equilibrium states<sup>29</sup>, ergodicity breaking is very easily established [151]. Compare two (typical) trajectories, one from each basin of attraction of the two equilibria. One finds that the time average of the two necessarily differs - and those are each different to the ensemble average in thermal equilibrium<sup>30</sup>.

It is therefore straightforward to construct ergodicity breaking systems in the classical case, one basically just needs a sufficiently nonlinear system with a bistable phase [151]. In the quantum regime, the question is mostly studied through the lens of the eigenstate thermalisation hypothesis (ETH) and is still a matter of active research [152, 153].

The bi- or multistable regions of the 2- and 3-level model for a single velocity class therefore imply ergodicity breaking by the system, and similarly so for the bistable regions in the hot vapour model with a finite number of velocity classes  $N_{vel}$ .

<sup>28</sup>Later, it has been established that the FPUT model indeed thermalises for their initial conditions, just on timescales much longer than they had studied [149–151].

<sup>29</sup>As a reminder, in the context of dynamical systems an equilibrium state is defined as a steady state and the system will develop in time towards the attractive ones.

<sup>30</sup>...given that each basin of attraction has a nonzero measure. The ergodic hypothesis is formulated for a dynamical system, i.e. the triplet  $(\Gamma, \mu, \Phi^t)$  with the system's phase space  $\Gamma$ , measure  $\mu$  defined on  $\Gamma$  and time evolution map  $\Phi$  at time  $t$ . For a more detailed definition of each, see e.g. [151].

### 4.5.2 TIME CRYSTALS

In 2012, the question has been raised whether time translation symmetry (TTS) could be broken in a classical [154] or a quantum mechanical [155] framework, and the quantum version was put on a more solid theoretical footing in 2016 [156, 157]. Such systems were coined time crystals, in analogy to spatially periodic structures called crystals, and were to possess a time-periodic structure. Soon after, the first reports of the experimental observation of discrete, i.e. periodically driven, Floquet time crystals emerged [158, 159].

Generally, one can distinguish different types of time crystals [160, 161]. Discrete time crystals arise in periodically driven systems where the system responds at an integer multiple of the drive period, thereby being both periodic in time and breaking discrete TTS. This type of time crystal is predicted to occur in some many-body localised systems [157]. The first two experimental reports of time crystals used closed quantum systems and were of this discrete kind.

Initially, it was thought that one had to carefully avoid dissipative channels in the system in order to find time crystalline states. However, this had been disproved theoretically [162] and experimentally [73, 163]. Additionally, it has been found that dissipative systems also allow for breaking of continuous TTS [164, 165], and first experimental realisations of a continuous dissipative time crystal have been reported in 2022 [166, 167]. In April this year (2023), a continuous time crystalline state has been observed at room temperature via periodic changes in the transmission of an optical metamaterial [168] and a preprint reports time crystalline behavior in the response of a semiconductor [169].

Following the strict definition of a time crystal as a "*stable, conservative, macroscopic clock*" given in [170], we cannot speak of a time crystalline phase occurring in the 3-level model or the hot vapour system. Others have relaxed the requirements for time crystals to also include open [171] and finite-body [172] systems. It therefore remains for the reader to decide whether or not they classify the 3-level model, or its hot vapour extension, as a time crystal. In any way, the phenomena are closely related and a thorough investigation of the hot vapour system in the limit  $N_{vel} \rightarrow \infty$  is of interest. The discussion of boundary time crystals [173] and their subsequent classification as genuine many-body phases of matter [174] are also of particular interest with respect to the system presented in this work.

### 4.5.3 KURAMOTO MODEL AND NONEQUILIBRIUM PHASE TRANSITIONS

The Kuramoto model describes the synchronisation of self-sustained oscillators with different natural frequencies  $\omega_j$ , interacting via global coupling [12]. For the Kuramoto model itself, the mechanism leading to self-oscillations is of no concern but it is taken to be a natural property of each oscillator. Of relevance is only the existence of a global mean field that each oscillator couples to and is influenced by. As a result, the oscillators begin to synchronise within a certain range of natural frequencies, which has been found to depend crucially on the coupling strength  $V$  between the oscillators, such that Arnold tongues form. This onset of synchronisation is regarded to be a nonequilibrium phase transition [175–177] from an equilibrium state to a (partially) synchronised, nonequilibrium state. The case of partial synchronisation occurs even for self-sustained oscillators with the same natural frequency  $\omega_0$  if the coupling is sufficiently nonlinear, and is sometimes also referred to as self-organisation [146].

Though the original model assumes a certain form of coupling between the individual oscillators, generalisations of the Kuramoto model have been proposed and their ability to produce (partially) synchronised states has been shown [4, 5, 177, 178]. Experimentally, the first- [179] and second-order [8] phase transitions to a synchronised state have been demonstrated, and for entrainment of two [180] and many [8] coupled oscillators, the formation of an Arnold tongue has been observed. Synchronisation of an ensemble of quantum oscillators has also been predicted [181].

The hot vapour system described in Section 4.4 shows the prerequisites of a generalised Kuramoto model: In certain parameter regimes, it produces self-sustained oscillators (the different velocity classes  $\mathbf{v}_j$ ) with a certain spread of natural frequencies  $\omega_j$ , which are globally coupled via a mean field (the total Rydberg atom density  $\rho_{rr}^r$  of the vapour). Similar to the nonequilibrium phase transition in the Kuramoto model, a transition to a synchronised state is observed upon variation of the bifurcation parameter  $\Delta_c$ . The similarities between the thermal vapour system of this work and generalised Kuramoto models are strikingly clear.

## 4.6 CLOSING REMARKS

In a hot Rydberg vapour, many processes happen at once that complicate an intuitive understanding of the system. Motion-induced detuning leads to a wide range of dynamics within the vapour even for fixed laser detunings. Rydberg interactions as well as collision-induced ionisation processes cause even richer dynamics in such a system by introducing strong nonlinearities. It is therefore difficult to develop an understanding of this complex system and intuit its response to external driving.

To this end, we have provided a simplified description of a hot Rydberg vapour based on the optical Bloch equations, with the assumptions that many-body correlations can be neglected in this environment due to the many sources of incoherence. The resulting steady state solutions for a single velocity class can be computed via the roots of a polynomial, which provides a fast and efficient method to find the steady state solutions of the system.

We have shown that an effective two-level system may possess a bistable phase where two attractive steady state solutions exist. In the three-level model, one additionally finds the system to be attracted towards limit cycles for certain conditions where a Hopf bifurcation occurs. These limit cycles arise fundamentally from the nonlinearity of the system, but equally require dissipative processes for their occurrence and maintenance.

To take into account the prevalence of many different velocity classes in a hot vapour, the three-level model was extended to a full hot vapour simulation. In this process, the different velocity classes are originally attracted towards different limit cycles. The global coupling of the velocity classes through a shared Rydberg density eventually leads to frequency and phase entrainment of the limit cycles, and synchronisation emerges in the system. This leads to the remarkable result that a single, clear and robust oscillation of the vapour's bulk quantities is predicted by this model.

These oscillations are connected to a time crystalline state, brought about and stabilised by the nonlinearity, dissipation, and coupling in the model system. The properties of this system are highly interesting to study experimentally since it provides access to a truly large number

of coupled oscillators and therefore allows to investigate the emergence of synchronisation in such large ensembles.

In the following chapter we report on the emergence of synchronisation in a driven-dissipative hot Rydberg vapour such as the one studied theoretically. Besides the already well-known bistability and hysteresis in such a system, we also find robust oscillations in the transmission of the probe laser through the vapour. These oscillations arise from synchronisation in the vapour, though the underlying mechanism causing the occurrence of limit cycles is disputed and currently unknown.

## 5 | OSCILLATIONS

As shown in the previous Chapter 4, a driven-dissipative Rydberg vapour with nonlinearities is predicted to show very unexpected behaviour in the response to constant external driving. Beyond the optical bistability and hysteresis effects shown in Figure 5.1 (a), we have observed persistent oscillations in the response of a hot vapour of rubidium atoms. As shown in Figure 5.1 (b), the transmission of the vapour changes periodically within a certain parameter regime when scanning the coupling laser through the two-photon resonance (main plot), and when fixing coupling and probe laser in the oscillation regime.

In this chapter, the experimental setup is presented before the observed dependence of the oscillations on the system parameters is discussed. The presence of oscillations in the probe laser transmission depends on the settings of the external parameters and the Rydberg state properties, i.e. the Rabi frequencies, detunings and interaction strengths. The average interaction strength experienced by an atom depends on the Rydberg state as well as on the vapour density and therefore also on temperature. The occurrence and frequency of the oscillations in the response of the vapour were investigated for different Rydberg states, various coupling and probe Rabi frequencies, and a range of vapour densities. In Section 5.2, the experimentally observed dependence of the oscillations on the external parameters is presented. The subsequent Section 5.3 then relates the observations to the three-level hot vapour model and discusses the experimental results in light of the relevant experiments, concepts, and literature.

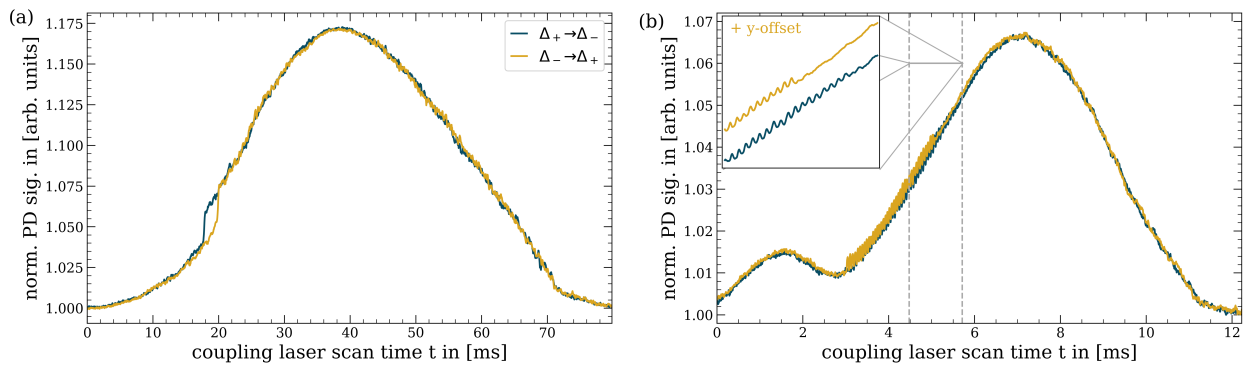


**Fig. 5.1: Bistability, hysteresis, and oscillations in the response of a thermal vapour.** Panel (a) shows a trace where optical bistability and the resulting hysteresis effect are visible as the coupling laser is scanned across two-photon resonance with a Rydberg state. The sudden jump in the vapour’s transmission is dependent on the coupling laser scan direction. (b) shows an example for the occurrence of oscillations on the resonance wing. The inset shows an enlargement of the oscillation region indicated by the gray dashed lines. The y-offset has been added for clarity.

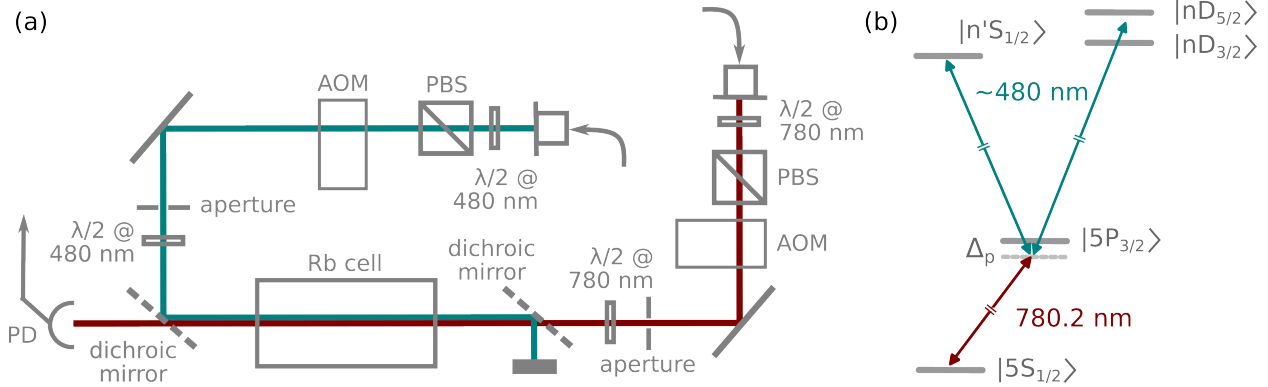


**Fig. 5.2: Experimental setup and relevant level scheme of rubidium.** (a) The probe and coupling laser light at 780 nm and 480 nm, respectively, are collimated by fiber couplers before passing a half-waveplate ( $\lambda/2$ ) and a polarising beamsplitter (PBS). The subsequent acousto-optic modulator (AOM) and aperture are used for remote control of the beam powers. Dichroic mirrors are used to combine the counterpropagating lasers on a shared beam path across the rubidium cell. The probe laser is detected by a photodiode (PD) which generates the measured voltage signal. (b) shows the generic level scheme of rubidium with the states that can be addressed via 2-photon excitation.

## 5.1 EXPERIMENTAL SETUP

The experimental setup used in this work is shown in Figure 5.2. A glass cell of 4 cm length is filled with rubidium at natural abundance<sup>1</sup> and held at constant vapour temperature which can be varied between 20 and 60 °C. In this work, the vapour temperature was varied in the range of 35 to 60 °C. The vapour is probed with a probe laser on the rubidium  $D_2$  line at 780.2 nm via detection of the transmission of the vapour, using two-photon EIT spectroscopy. The probe laser is locked at  $2\pi \times 140$  MHz below the closed transition  $|5S_{1/2}, F = 2\rangle \leftrightarrow |5P_{3/2}, F = 3\rangle$  of  $^{87}\text{Rb}$  [147] via modulation transfer spectroscopy (MTS) [182, 183]. The optical lock signal is fed into a PID controller for frequency stabilisation.

A counterpropagating coupling laser at  $\sim 480$  nm couples the intermediate state to a Rydberg state, which is either an  $|nS\rangle$  or  $|nD\rangle$  state. The coupling light is derived from the seed laser's fundamental light at  $\sim 960$  nm via second harmonic generation in a nonlinear crystal. The fundamental light of the coupling laser is locked to an ultranarrow, ultrastable cavity via sideband locking with an electro-optic modulator (EOM) [184, 185]. The error signal is generated from the cavity reflection spectrum with the Pound-Drever-Hall (PDH) error signal generation scheme [186, 187]. Using the EOM sideband allows to lock the laser to an arbitrary point in the cavity spectrum. Scanning the sideband frequency then scans the laser lock point across the frequency spectrum. Further details on the newly installed coupling laser and the updated cavity lock can be found in Appendices E and F.

The polarisation of the probe and coupling lasers is cleaned after exiting the fiber by use of polarising beamsplitters (PBS) and then set to the desired orientation by manual adjustment of a half-waveplate ( $\lambda/2$ ). Finally, the laser powers supplied to the experiment are remotely con-

<sup>1</sup>Natural abundance of rubidium is 28% of  $^{87}\text{Rb}$  and 72% of  $^{85}\text{Rb}$ . The  $^{87}\text{Rb}$  isotope was used in this work.

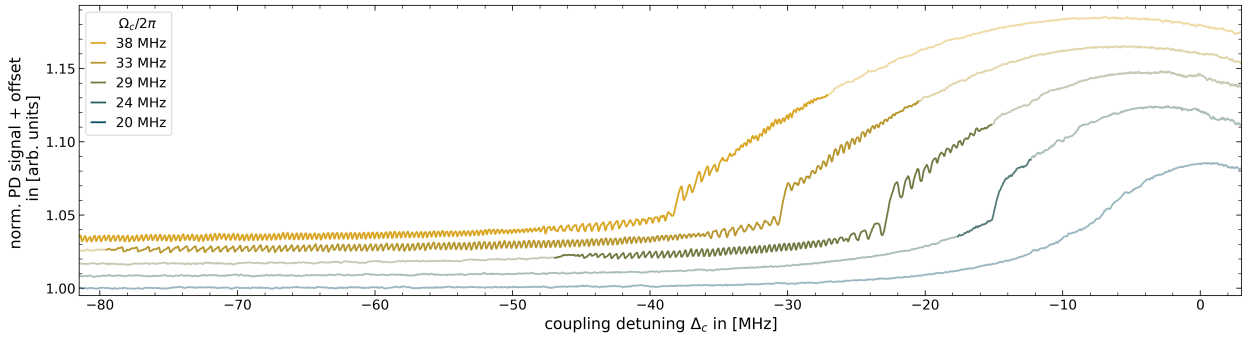


**Fig. 5.3: Onset of oscillations with increasing coupling Rabi frequency.** For a fixed probe Rabi frequency  $\Omega_p$ , the coupling Rabi frequency  $\Omega_c$  is increased and the normalised photodiode signal is shown. After the appearance of bistability in the vapour response, one can see an onset of oscillations for even higher coupling Rabi frequencies  $\Omega_c$ . The probe transition Rabi frequency is  $\Omega_p = 2\pi \times 191$  MHz for this dataset, the Rydberg state was  $|43D_{5/2}\rangle$  and the measurement was taken at a vapour temperature of  $T = (52.0 \pm 0.5)$  °C. This corresponds to a number density of  $^{87}\text{Rb}$  atoms of  $\rho_{^{87}\text{Rb}} = (4.7 \pm 0.2) \cdot 10^{10} \text{ cm}^{-3}$  [98, 189]. Each trace was given an individual y-offset for better visibility.

trolled via acousto-optic modulators (AOMs), which deflect power into higher orders propagating at slightly different angles such that they are dumped by an aperture.

Beam waists of up to 1 mm and different probe to coupling beam waist ratios  $w_p/w_c = 0.5, 2$  have been tried and no dependence of the oscillations on the beam waists has been observed. The data presented in this thesis was taken for probe and coupling beam waists of  $w_p = 390 \mu\text{m}$  and  $w_c = 440 \mu\text{m}$  respectively, unless specifically stated otherwise. Typical probe laser powers for the experiment were in the range of 50 – 600  $\mu\text{W}$ , while the coupling laser power is usually varied over a range of 25 – 300 mW. This corresponds to Rabi frequencies<sup>2</sup> of  $\Omega_p/2\pi$  in the range of 95 to 330 MHz and  $\Omega_c/2\pi \leq 35$  MHz.

For radiofrequency (rf) field sensing and similar applications one usually keeps the laser powers below the saturation intensity<sup>3</sup>, particularly the probe laser power. This is to avoid – or at least to minimise – effects like electron shelving and power broadening [118]. The strong driving regime is therefore rather seldomly used in hot vapour applications. For the beam waists specified above, one leaves the weak probe regime at roughly 18  $\mu\text{W}$ , or just below  $\Omega_p = 2\pi \times 60$  MHz.

When scanning the coupling laser across two-photon resonance, we have observed that increasing the coupling laser power to give higher Rabi frequencies often leads to an onset of bistability in the vapour response before entering the oscillation regime at even higher Rabi frequencies, as shown in Figure 5.3. Bistability refers to the sudden change in the vapour transmission where the system jumps from one stable state to another. The width of the oscillation region increases with increasing Rabi frequency as can clearly be seen in Figure 5.3. The dependence of the oscillations on the experimental parameters is presented in the following section.

<sup>2</sup>Rabi frequencies always state the peak Rabi frequency for a  $\text{TEM}_{00}$  (Gaussian) mode.

<sup>3</sup>The saturation intensity is usually a good benchmark for whether or not one is in the weak probe regime, even though one should generally be careful when defining a weak probe threshold [188].

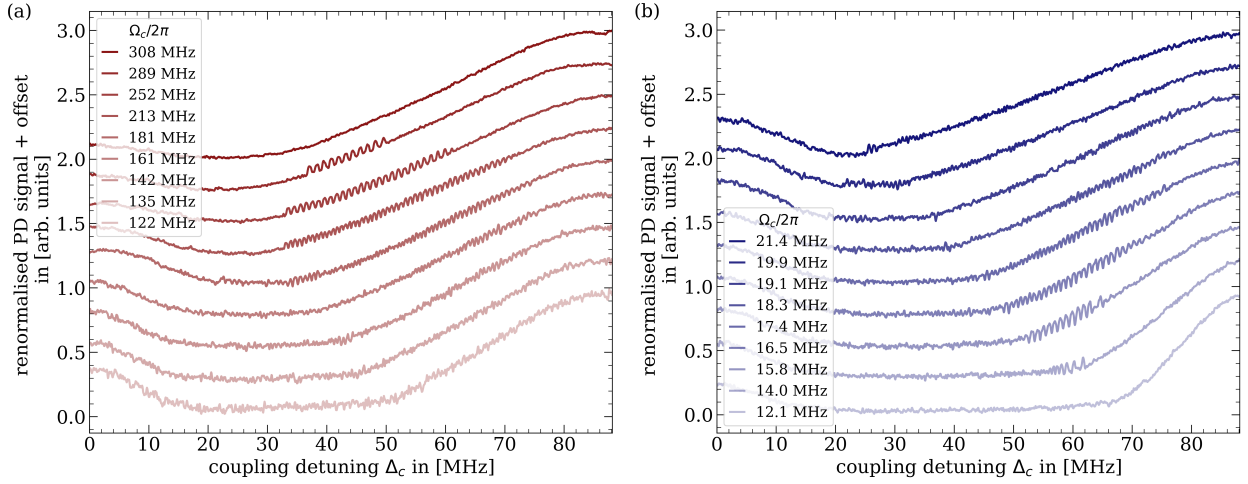


**Fig. 5.4: Scaling of oscillation regime with Rabi frequencies.** The occurrence of the oscillation regime is shown for for varying probe (a) and coupling (b) laser powers with the respective other parameters kept constant. The coupling laser coupled to the  $|50D_{3/2}\rangle$  Rydberg state at  $\Delta_c = 0$  MHz and the  $|50D_{5/2}\rangle$  state at  $\Delta_c = 2\pi \times 93$  MHz. The coupling Rabi frequency was kept constant at  $\Omega_c = 2\pi \times 18$  MHz in (a) and the probe Rabi frequency at  $\Omega_p = 2\pi \times 160$  MHz in (b), respectively.

## 5.2 BEHAVIOUR AND SCALING OF OSCILLATION REGION WITH EXPERIMENTAL PARAMETERS

In this section, the observed typical behaviour of the oscillations and the scaling of the oscillation region with the various experimental parameters is presented. The underlying mechanism causing the oscillations is currently disputed in literature, with two other works on this type of oscillations emerging during the completion of this thesis [190, 191]. In [190], it is proposed that limit cycles arise from a competition for population between different energetically close states in the Rydberg manifold. The authors of [191] propose that spatial inhomogeneities and a resulting spatial clustering of Rydberg atoms induce limit cycles.

The data in this Section is therefore presented as is with a purely descriptive approach to the phenomenon. Scalings of the width of the oscillation region with changes in Rabi frequency are discussed in Section 5.2.1 while the dependence on Rydberg state, and vapor temperature is shown in Section 5.2.2. The frequency of the oscillations is studied in Section 5.2.3 and we take a brief look at the shape of the oscillations along the scan in Section 5.2.4. A contextual discussion and interpretation of the results follows in Section 5.3.

### 5.2.1 DEPENDENCE OF OSCILLATIONS ON RABI FREQUENCIES

Figure 5.4 shows typical traces when scanning the coupling laser through two-photon resonance with a Rydberg state and increasing the Rabi frequency on one of the two transitions. All other experimental parameters were held constant. Within a certain parameter regime, os-

cillations occur in the transmission of the probe laser through the vapour<sup>4</sup>.

In Fig. 5.4 (a), the probe laser Rabi frequency is increased from the bottom to the top trace. Eventually, an oscillation region becomes clearly visible but the width of the region and the oscillation frequency reduce with increasing probe power. After crossing a threshold probe power, no oscillations remain in the response of the vapour.

The width of the oscillation region scales inversely when changing the coupling Rabi frequency since the oscillation region opens with increasing  $\Omega_c$ . After meeting a threshold coupling Rabi frequency, slow oscillations occur in the response of the vapour. The oscillation frequency and width of the region increases with increasing coupling power, as can be seen in Figure 5.4 (b). When increasing the coupling Rabi frequency even further, the oscillations become too fast to be distinguishable from noise in the scans. However, one can still see an edge, or plateau, near the  $|50D_{3/2}\rangle$  state at  $\Delta_c = 0$  MHz in the spectrum.

This general behaviour was consistently observed for different Rydberg states and atom number densities. However, the oscillation frequency is not always constant within one oscillation region, as one can see in some of the traces in Figure 5.4. For that reason, speaking of ‘the oscillations’ and of a single oscillation frequency does not capture the entire picture but is a simplification that is done here for ease of discussion. It is important to keep in mind, though, that the observations in the lab are more complex than that. Further example traces demonstrating this behaviour are shown in Figures 5.8 and 5.9.

### 5.2.2 SCALING WITH VAPOUR DENSITY AND RYDBERG STATE

It has been mentioned before that the presence of oscillations depends on the external experimental parameters, and that several oscillation regions may form. It is therefore very interesting to analyse the data from a different perspective by identifying the spectral regions where oscillations occur for different combinations of experimental parameters. This may help to shed some light on the underlying mechanism causing the occurrence of oscillations.

Example results are shown in Figure 5.5, the upper row shows the spectral regions in which oscillations are observed when coupling to the  $|79D\rangle$  states at different Rabi frequencies and three different densities. For fixed probe Rabi frequency  $\Omega_p$  one can observe an onset of oscillations at lower coupling Rabi frequencies for higher temperatures and therefore vapour densities. Clearly, one can infer a dependence of the presence of oscillations on the vapour density.

The lower row of Figure 5.5 shows the oscillation regime when addressing three different Rydberg states at similar vapour densities. Here, the onset of oscillations occurs at lower coupling Rabi frequencies for higher Rydberg states and otherwise similar experimental parameters. It is interesting to note that the van der Waals interaction  $|43D_{5/2}\rangle$  state is larger than of the  $|50D_{5/2}\rangle$  state due to a near Förster resonance [106] with the  $|42F_{5/2,7/2}\rangle$ ,  $|44P_{3/2}\rangle$ , and  $|45F_{5/2,7/2}\rangle$  pair-states. The  $C_6$  value of the  $|63D_{5/2}\rangle$  state is a factor 10 higher than that of the  $|50D_{5/2}\rangle$  state. Additionally, the formation of spectrally separate regions can clearly be seen in the dataset for the  $|63D_{5/2}\rangle$  state.

<sup>4</sup>In this example, no bistability occurs before or after the oscillation regime. The presence or absence of a bistability edge depends on the external parameters, including beam alignment. All data in this thesis was taken after optimising on a weak probe EIT feature, which indicates optimised beam overlap.

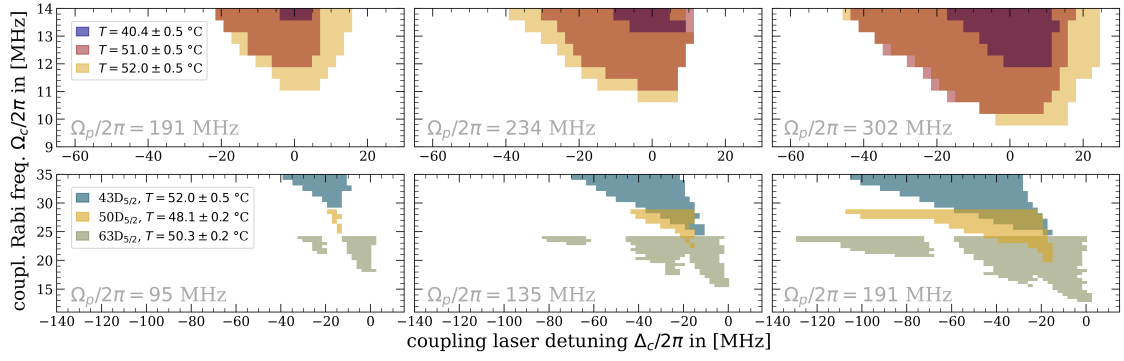


**Fig. 5.5: Scaling of oscillation region with experimental parameters.** The upper row shows the oscillation region with a coupling to the  $|79D_{5/2}\rangle$  state at  $\Delta_c = 0$  for three different probe Rabi frequencies and three different vapour densities. The critical coupling Rabi frequency required for an onset of oscillations reduces with increasing vapour temperature and therefore increasing number density. In the lower row, the oscillation region is indicated for three different Rydberg states at similar vapour temperatures. One can clearly see different, spectrally independent oscillation regimes in the  $|63D_{5/2}\rangle$  data. Also, the onset of oscillations occurs at lower critical coupling Rabi frequencies for higher- $n$  Rydberg states.

Generally, it is observed that higher probe Rabi frequencies, higher- $n$  Rydberg states and higher vapour densities lead to a lower threshold coupling Rabi frequency  $\Omega_c$  required to observe an onset of oscillations.

Furthermore, a different kind of splitting of the oscillation region has been observed for the  $|77D_{5/2}\rangle$  state at high vapour temperatures, as is shown in Figure 5.6. Here, the oscillation region suddenly breaks with a clear edge and a second oscillation region may form at the far side of the break for higher coupling Rabi frequencies.

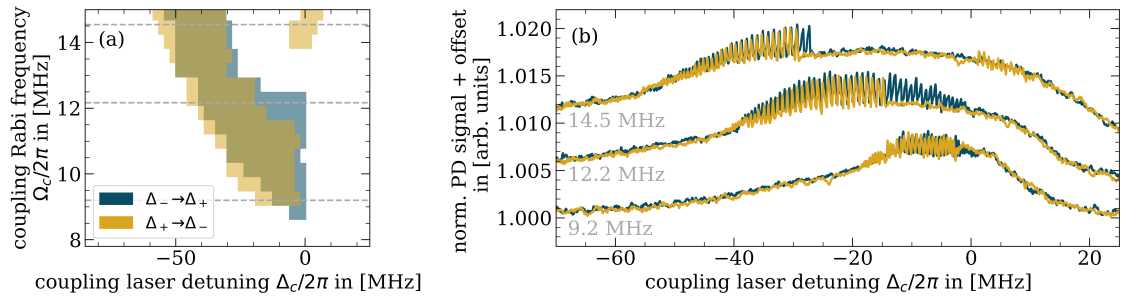


**Fig. 5.6: Sudden break in oscillation region for  $|77D_{5/2}\rangle$  state.** (a) shows the oscillation region for the  $|77D_{5/2}\rangle$  state at a probe Rabi frequency of  $\Omega_p/2\pi = 234$  MHz and vapour temperature  $T = (50.5 \pm 0.5)$  °C for different coupling Rabi frequencies  $\Omega_c$ . The oscillation region in the top right corner is present only for one scan direction but not the other. (b) shows the traces corresponding to the coupling Rabi frequencies  $\Omega_c/2\pi$  indicated by the gray dashed lines in (a). The corresponding values  $\Omega_c/2\pi$  are indicated below the respective traces. Each pair of traces has an arbitrary offset for better visibility.

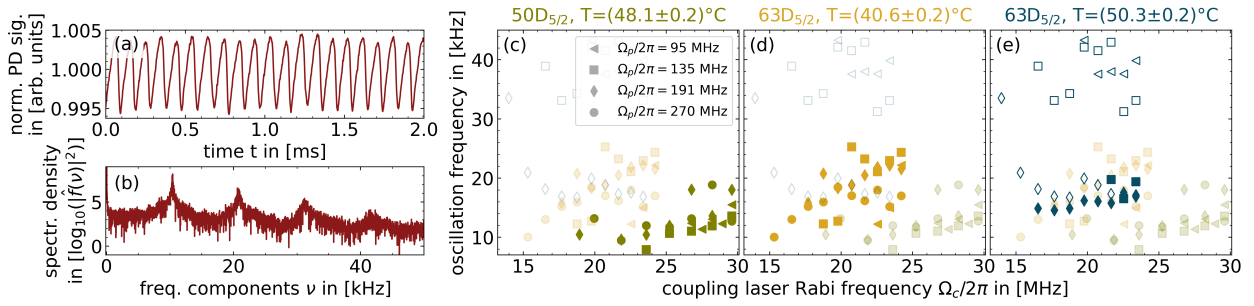


**Fig. 5.7: Comparison of oscillation frequency in different regimes.** (a) shows an example of the oscillations in time for fixed coupling laser detuning  $\Delta_c$ . The coupling laser couples to the  $|50D_{5/2}\rangle$  state with  $\Omega_p = 2\pi \times 191$  MHz,  $\Omega_c = 2\pi \times 24$  MHz and  $T = (48.1 \pm 0.2)^\circ\text{C}$ . Panel (b) shows the resulting spectral density of the time trace in (a). This is used to extract the oscillation frequency. (c)-(e) show the oscillation frequency for various probe Rabi frequencies, for different Rydberg states and vapour temperatures. At higher number densities the  $|63D_{5/2}\rangle$  state shows two spectrally separate regions with oscillations, compare also with Figure 5.9. The open blue symbols show the oscillation frequency for the second oscillation region that does not exist in the other datasets. Further details can be found in the main text.

### 5.2.3 OSCILLATION FREQUENCY SCALING

To get a better understanding of the scaling of the oscillation frequency with the Rabi frequencies and the Rydberg-Rydberg interaction strength, a direct measurement of the oscillation frequency was made. For these measurements, the coupling laser detuning was fixed such that the system was inside the oscillation regime and a time trace of the probe laser transmission through the vapour was captured, as shown in Figure 5.7 (a). Therefore, all external parameters were kept constant for the duration of one measurement, which includes laser powers and detunings, and vapour temperature. The response of the vapour shows an oscillatory behaviour that is persistent in time and appears undamped on timescales as long as ten minutes. Oscillation frequencies were inferred from the time traces by calculation of the Fourier spectrum of the trace in Figure 5.7 (a). The oscillation frequency was taken to be the lowest frequency peak in the spectral density  $|\hat{f}(\omega)|$  which is not the DC component, as shown in (b).

The data for Figure 5.7 (c)-(e) was collected by performing this measurement for a range of Rabi frequencies on the  $|50D_{5/2}\rangle$  (olive) and  $|63D_{5/2}\rangle$  (yellow, blue) states. The yellow and blue data points are both for the  $|63D_{5/2}\rangle$  state but the yellow dataset was taken at a lower vapour temperature, i.e. at lower atom number density. Olive and blue datasets were taken for similar atom number densities but different Rydberg states. The blue dataset features not just one but two oscillation regions with different oscillation frequencies. This second region lies closer to the resonance with the  $j = 5/2$  state in the spectrum. It does not occur in the other dataset from that Rydberg state (yellow) and is therefore indicated with open symbols. The different shapes of the symbols indicate different probe Rabi frequencies. Further example traces can be seen in Figure 5.9.

For some datasets there seems to be a tendency of increasing oscillation frequencies for higher coupling laser powers, as can also be seen in the top row of Figure 5.9. Given the data, there is no obvious relation between oscillation frequency and probe Rabi frequency. However, as

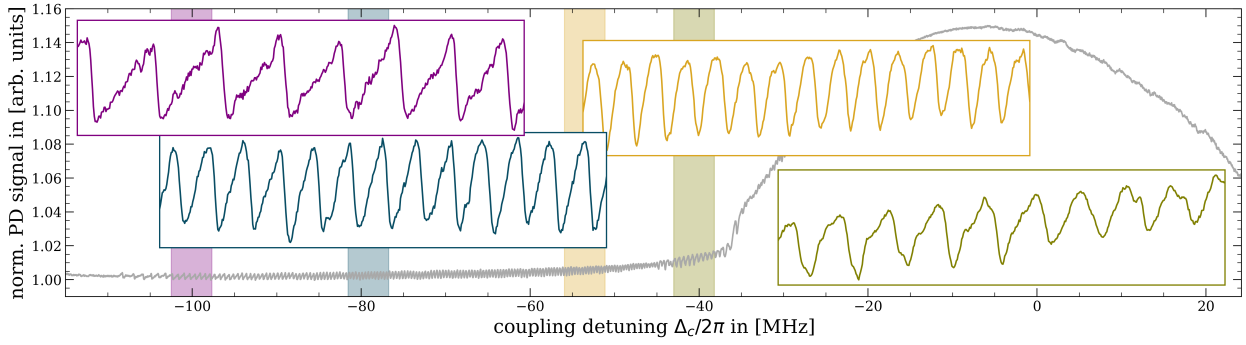


**Fig. 5.8: Change in frequency and shape of oscillations along scan.** Example trace from the  $|43D_{5/2}\rangle$  state at  $2\pi \times 191$  MHz probe Rabi frequency and  $2\pi \times 37$  MHz coupling Rabi frequency at  $T = (52.0 \pm 0.5)$  °C. The oscillations have generally been observed to change in shape along the oscillation region. Observed shapes resemble sawtooth, sawtooth with steps in the flank, modulus of cosine/ $\cos^2$  and triangular functions. The highlighted regions shown in the insets have the same frequency width so one can see the change in oscillation frequency between the regions.

mentioned before, the oscillation frequency varies within a single oscillation region. It therefore seems unreasonable to derive any conclusive interpretation from the data shown in Figure 5.7 (c)-(e). This invites a further, more systematic investigation of the phenomenon.

#### 5.2.4 SHAPE AND FREQUENCY OF OSCILLATIONS ALONG SCAN

As remarked in the previous section, the oscillation frequency changes along the oscillation region. This change in oscillation frequency goes along with a change in shape of the oscillations, as shown in Figure 5.8. It shows an enlargement of the four highlighted regions, each covering the same frequency range. The oscillation shapes were observed to resemble sawtooth, sawtooth with steps in the rising flank, triangular, and modulus of cosine or  $\cos^2$  functions. Many datasets, but not all, show the same order of shapes from negative towards positive detuning: sawtooth, triangular, cosine-like.

Additionally, Figure 5.8 indicates the presence of two separate oscillation regions, sharing a spectral boundary at  $\Delta_c/2\pi \approx -45$  MHz. The discrete change in oscillation frequency, as well as the repeated occurrence of the sawtooth shape in the lower-frequency end of the rightmost (olive) region, indicates that the two regions are indeed separate and independent of another. In Figures 5.5 and 5.9 the occurrence of spectrally separate oscillation regions is also very clearly visible.

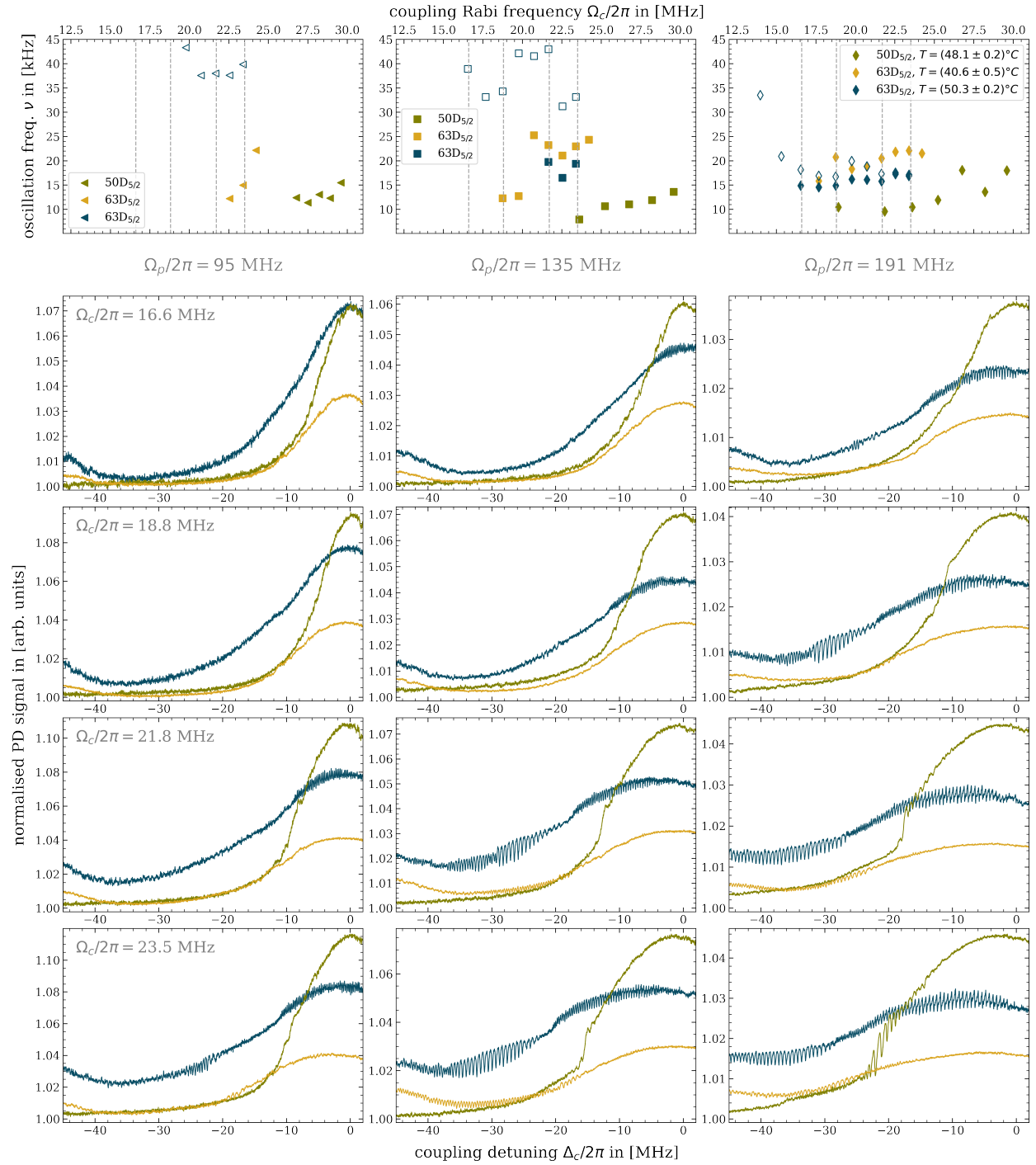


**Fig. 5.9: Example traces in oscillation regime.** The transmission of the vapour is shown for three different probe Rabi frequencies  $\Omega_p$  (columns) and four different coupling Rabi frequencies  $\Omega_c$  (rows), increasing to the right and bottom, respectively. The Rabi frequencies of the example traces are indicated in the oscillation frequency plots in the top row. The colour coding and corresponding datasets are the same as in Figure 5.7.

### 5.3 INTERPRETATION OF THE EXPERIMENTAL RESULTS

The experimental results were presented without interpretation or context to allow the reader to draw their own conclusions from the data. This section will provide the context for the experiment and an interpretation of the data.

The most notable feature of the observed oscillations is that their occurrence is independent of the coupling laser scan speed. This goes as far as that the oscillations persist in time when fixing all controllable parameters including the coupling laser detuning, as shown in Figure 5.7. The system is driven with constant laser powers and frequencies, therefore the oscillations cannot occur as a consequence of external modulation. Additionally, the laser Rabi frequencies are three orders of magnitude faster than the oscillation frequency. Hence, the oscillations do not originate from periodic driving but emerge fundamentally from the system itself. This is also supported by Figure 5.5 which shows that a variation of the vapour density changes the threshold for an onset of oscillations without changes to the driving of the system.

Conclusively, we observe a system that is attracted toward a limit cycle in certain parameter regimes. From this conclusion, several questions emerge that we will attempt to answer with the tools developed in this thesis and the experimental data presented above. One may now ask: What mechanism causes the occurrence of limit cycles in this system? How can we interpret these oscillations from a physical perspective? And how is it that a hot vapour with motion-induced dephasing of the different velocity classes of atoms still shows a clear, robust oscillatory response rather than a superposition of many different limit cycles averaging out to a noisy signal?

#### *Synchronisation*

The last question is maybe the easiest one to answer. We have already established that the system is attracted toward a limit cycle, but naïvely one would expect that every velocity class of atoms is attracted towards a different limit cycle due to the motion-induced detuning. As a result, the response of the vapour would be a noisy and incoherent signal, as shown in the lower row of Figure 4.11. This is not what we observe, since we clearly find a single oscillatory signal. The mechanism which prevents a noisy output is a global coupling between the different velocity classes leading to synchronisation. This coupling between the different velocity classes could be induced by Rydberg interactions between the different velocity classes, or the global effects of Stark shifts induced by ionised Rydberg atoms. Other coupling mechanisms are also possible. There is experimental evidence for the presence of a weak plasma in a hot vapour Rydberg experiment under similar conditions as ours [63, 65], and Rydberg-Rydberg interactions certainly also occur in our experimental regime. In Chapter 4, we have shown that both effects could lead to the formation of limit cycles for different velocity classes, and provide their own respective global coupling mechanisms.

The relevant point to stress here is that there must be a mechanism in the system which combines the different limit cycles expected from the microscopic description of the hot vapour to a single and clear oscillatory signal of the bulk quantities. Such a mechanism is provided by the synchronisation of the constituent oscillators through a global coupling force, irrespective of its

nature. We therefore attribute the observation of robust and stable periodic oscillations to the emergence of synchronisation in a driven-dissipative hot Rydberg vapour.

### *Possible mechanisms causing oscillations*

One would then like to know which mechanism actually causes the occurrence of limit cycles, and this question is not so easy to answer. In Chapter 4 we have shown that any Rydberg-population dependent level shift, which can be mapped to a power law in the Rydberg density, renders the system nonlinear and may cause Hopf bifurcations which can facilitate the occurrence of attractive limit cycles. Both the Rydberg interactions and the ion-induced Stark shifts of the Rydberg level can be mapped onto a power law scaling<sup>5</sup>, but other mechanisms may equally cause the system to be attracted towards limit cycles. In [190], it is proposed that limit cycles arise from a competition for population between different energetically close states in the Rydberg manifold. The authors of [191] propose spatial inhomogeneities and a resulting spatial clustering of Rydberg atoms to induce limit cycles.

The second proposed mechanism, i.e. the cluster-induced limit cycles, is a theory which fits well for the experimental parameters reported in [191]. However, the probe Rabi frequencies used in this work are around one order of magnitude higher than in the reference, and an estimation of expected Rydberg atom densities in our experiment shows that we are near or even well inside the regime of saturated Rydberg densities due to the blockade effect. This spatial clustering hypothesis therefore seems unlikely to capture the processes in our system under strong driving. Additionally, the oscillations observed in [191] are transient rather than persistent. They also scale differently to the ones reported here and in [190], where the experimental conditions are similar to ours.

The authors of [190] cite a competition for Rydberg population between energetically close levels as causing limit cycles. The theory, as presented in the paper, assumes a direct coupling of ground and Rydberg state with an effective Rabi frequency  $\Omega$ . In other words, the assumption is made that one can eliminate the intermediate state dynamics, which tends to be a difficult assumption to make in a hot vapor where Doppler shifts easily lead to effective detunings of several linewidths  $\Gamma_{ge}$ . This assumption certainly does not hold for the experiments reported in this work since the intermediate state detuning is only  $\Delta_p/2\pi = -140$  MHz. This is easily surpassed by the 1D RMS velocity of rubidium atoms at 40°C, meaning that some velocity classes experience significant population of the intermediate state which changes the dynamics of the system. Nonetheless, the proposed mechanism of limit cycles being caused by competition for Rydberg population of different  $m_J$  states within the Rydberg manifold is possible. In this interpretation, it would also be the Rydberg interaction causing a global coupling between different velocity classes so that synchronisation may occur<sup>6</sup>.

A further hint on the origin of limit cycles for a single velocity class is given by Figure 5.5, showing the synchronisation regions for various Rydberg states, densities, and laser powers.

<sup>5</sup>The conditions for this mapping to a power law to be (approximately) accurate can be found in Appendices B and C for Rydberg interactions and Stark shifts, respectively.

<sup>6</sup>In [190], the system has been studied theoretically only for a single velocity class. It would be interesting to investigate the proposed model in a full hot vapour simulation to see how bistability and synchronisation behave when taking many velocity classes into account. Also, including the intermediate state in the theoretical description might reveal further dynamics and would be relevant in the context of a full hot vapour treatment.

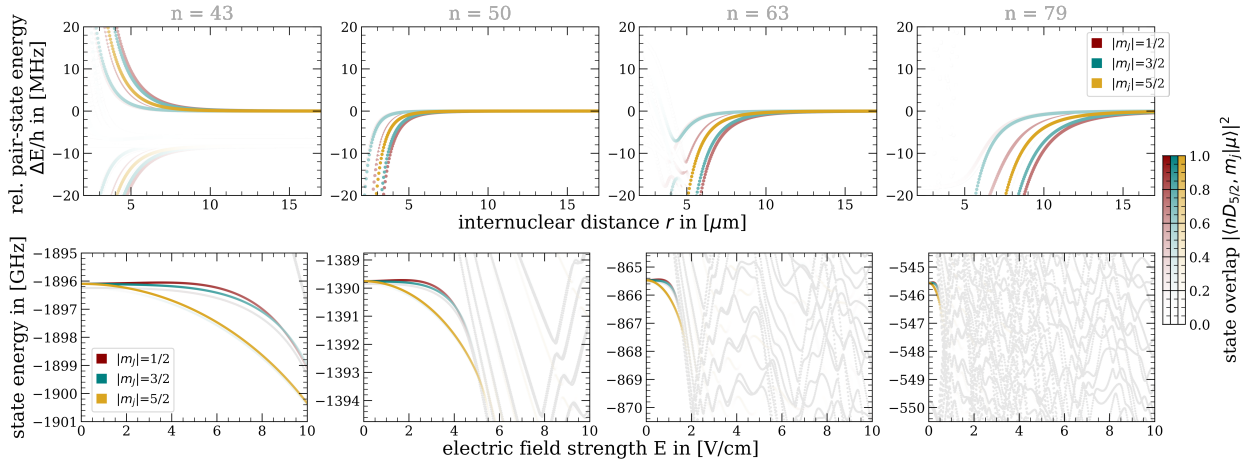


**Fig. 5.10: Pair interaction potentials and Stark shifts for  $43D_{5/2}$ ,  $50D_{5/2}$ ,  $63D_{5/2}$  and  $79D_{5/2}$  states in rubidium.** The pair potentials (upper row) and Stark shifts (lower row) for the Rydberg states in Figure 5.5. As can also be seen in the resulting pair potential, the  $|43D_{5/2}\rangle$  Rydberg pair state has a Förster resonance with the  $|42F_{5/2,7/2}\rangle$ ,  $|44P_{3/2}\rangle$ , and  $|45F_{5/2,7/2}\rangle$  pair states. Pair potential data is given for spatial orientation of the atoms along the quantisation axis. The electric field polarisability increases with  $n$ .

The upper row shows the synchronisation region for various densities when coupling to the  $|79D\rangle$  states. It indicates a clear dependence on the vapour density and therefore on the Rydberg atom spacing. This is consistent with any interpretation that uses Rydberg interactions as mechanism where higher Rydberg densities lead to stronger facilitation of synchronisation in the vapour, but it is similarly in agreement with the ion-induced Stark shift interpretation.

More interesting is the lower row of Figure 5.5 where the synchronisation regime is shown for different Rydberg states with  $n = 43, 50, 63$ . One can clearly see that the threshold coupling Rabi frequency required for an onset of oscillations is lower for higher principal quantum numbers  $n$  at every probe Rabi frequency shown in the plot. The Rydberg states were chosen due to their  $C_6$  interaction strengths since the  $|43D_{5/2}\rangle$  state is on a Förster resonance, leading to stronger van der Waals interactions than for the  $|50D_{5/2}\rangle$  state. One might expect to see a trace of this in the data in form of a lower critical coupling Rabi frequency marking the onset of oscillations – if the limit cycles are caused by van der Waals interactions. No indication for this can be seen.

The observed lowering of the critical coupling Rabi frequency with higher  $n$  is consistent with a plasma-induced Stark shift causing the occurrence of limit cycles. Reason being that higher  $n$  states have a higher polarisability, as shown in Figure 5.10, and higher ionisation cross sections. This leads to an earlier onset of oscillations for higher principal quantum numbers due to higher global coupling strengths  $V$ .

It is yet too early to settle on one mechanism as cause of the limit cycles and more experiments are required to answer this question with certainty.

## 5.4 OPEN QUESTIONS, OUTLOOK, AND CONCLUSION

Several open questions remain, first and foremost the one regarding the origin of and mechanism behind the limit cycles. Different mechanisms have been proposed and can be tested through further experiments.

The Rydberg interaction mechanism could be tested with a comparison of the  $|43D_{5/2}\rangle$  state to the  $|42D_{5/2}\rangle$  at otherwise identical parameters. The van der Waals interaction of pairs of  $m_J = 5/2$ -state atoms differs by a factor of  $\approx 20$  between these two neighboring states while the other  $m_J$  state pair interactions and the collisional cross-section for ionisation of Rydberg atoms is very similar. Alternatively, addressing only the  $m_J = 5/2$  state and variation of the principal quantum number between 42 and 43 should equally provide further information on the Rydberg interaction dependence. If one observes oscillations while coupling only to a single (hyper-)fine state, then this would also be a strong indication against the Rydberg population competition mechanism assumed in [190]. It would also be interesting to look at the dependence of the onset of synchronisation on the intermediate state detuning, and to compare attractive and repulsive pair interactions.

Using an ultracold atomic vapour setup would allow the system to be studied without the Doppler averaging across many velocity classes, so that the behaviour of a single velocity class would become accessible. Additionally, as the plasma formation in a hot vapour is mostly induced by collisional ionisation of Rydberg atoms, a frozen gas experiment would give access to a plasma-free environment. These experiments usually also feature excellent electromagnetic field control such that one could investigate the effects of external Stark shifts as well. Alternatively, a weak DC field could be used in a hot vapour cell to quickly siphon off all charges from the beam area and therefore remove the plasma from the beam region.

An electromagnetic field dependence opens an avenue to utilise the oscillations for electromagnetic field sensing, or to exert further control on the system by providing additional tunable parameters. When using this platform to experimentally study the emergence of synchronisation in ensembles of large numbers of coupled oscillators, such an externally tunable parameter might prove to be very useful.

We can conclude that the origin of the limit cycles in our system remains unclear at present. Understanding the underlying mechanism would allow a better understanding of the system, also when subject to additional fields, and improve predictability of the system's response.

However, irrespective of the origin of the limit cycles, all currently proposed and studied mechanisms have in common that the hot vapour system hosts a wide range of different velocity classes, each being attracted to different limit cycles. The frequency entrainment of the limit cycles is caused by global mean-field coupling of all velocity classes, which eventually leads to synchronisation and a single oscillatory response of the vapour. This oscillation of the probe transmission through the vapour is robust and does not show any damping on timescales on the order of minutes.

The three-level hot vapour simulation presented in Chapter 4 phenomenologically reproduces the experiment. This includes the occurrence of several spectrally separated synchronisation regions, the resulting shapes of oscillations, and scalings with probe and coupling Rabi frequencies and coupling strength. This scaling includes the changes in width of the oscillation region with changes in  $\Omega_p$  or  $\Omega_c$ , see also Figure 5.4, and the earlier onset of oscillations at

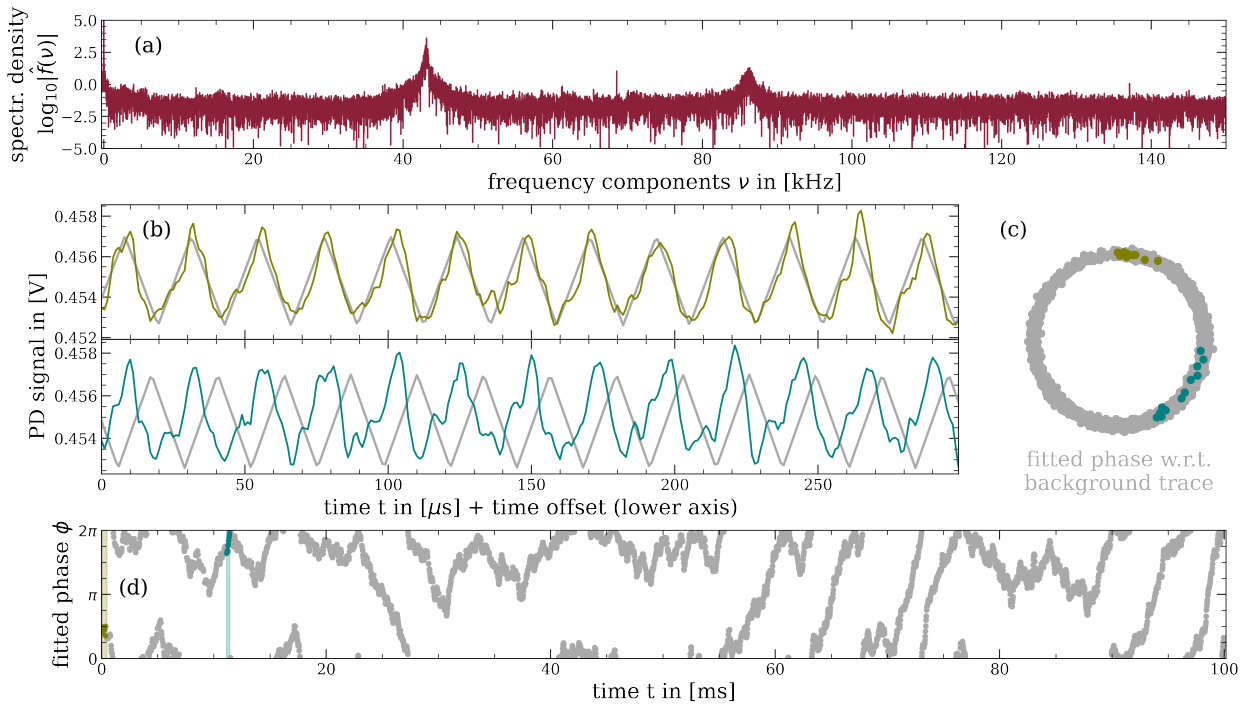


**Fig. 5.11: Phase drift of oscillations in a single realisation.** (a) The spectral density of the oscillations reveals a clear oscillation frequency  $\nu_{osc}$  of 43.1 kHz. Two segments of the data trace are shown in (b) with a background triangular waveform of frequency  $\nu_{osc}$  in dark gray. The drift in phase between the two segments is clearly visible, and the lower segment (blue) also shows an additional slight change in oscillation frequency. The extracted phases of the waveform over the length of the entire sequence of 0.1 s are shown in (c) and (d) with the coloured dots indicating the segments of (b).

lower  $\Omega_c^{crit.}$  for higher interaction strengths  $V$ . Hysteresis with the coupling laser scan direction is also predicted by the hot vapour simulations and the model reproduces the experimentally observed oscillation frequencies e.g. for the Rydberg interaction Hamiltonian at reasonable experimental parameters. Even though the origin of the limit cycles is still unclear and further experimental and theoretical work has to be done to answer this question, we can conclude that the major properties of the hot vapour model are also found in the experiment. These are ergodicity breaking from optical bistability, as well as the emergence of synchronisation leading to a non-equilibrium state of matter.

More difficult is a statement on the time crystallinity phase that is claimed in reference [190]. To experimentally demonstrate a time crystal it is necessary to show the freedom of phase in the limit cycle for different realisations of the system. The idea is that, since the phase of the system on the limit cycle is not fixed but pre-determined only by the initial conditions, then different instances of realisations of the same system should differ in phase because initial conditions will naturally vary on a microscopic level. However, in order to attribute a measured phase variance to different realisations of the system, one first needs to show phase invariance of the system within a single realisation. That means that for any one realisation, the phase of the oscillations

with respect to a reference waveform at the oscillation frequency should be invariant. Deviations of the phase in time hint at correlations and drifts with other experimental parameters like, among others, laser powers and detunings. One expects that stable experimental conditions are required to arrive at a system that is phase invariant in time for a single realisation – so that the time crystal property can be shown.

Figure 5.11 shows that this is not the case for our experimental setup in the present form. The extracted phase of the oscillations fluctuates over time for one long-term data trace, as shown in (d). The resulting spread in phases is attributed to fluctuations in experimental parameters, and the system is arguably not stable enough in time during a single realisation to be able to infer phase freedom in the limit cycle from a variation of phases for different realisations. It is therefore not possible to demonstrate a continuous driven-dissipative time crystal with the experimental setup in its present state.

Updates to the experiment in the form of stabilisations of the experimental parameters is expected to improve on the phase drifts. In small systems with gapped many-body Hamiltonians it might be possible to show the time crystalline phase of the system's ground state even in the presence of experimental uncertainties and noise. For macroscopic systems of many constituents and an effectively ungapped many-body Hamiltonian, it is currently unclear if time crystallinity can conclusively be shown from an experimental perspective<sup>7</sup>.

---

<sup>7</sup>It is currently unclear whether it is experimentally feasible to stabilise the experimental parameters to the necessary degree of stability in order to arrive at phase invariance on reasonably long timescales. In private communications, the authors of [190] indicated that they had also observed phase drift like it is shown in Figure 5.11 (d). They mentioned that a certain level of phase diffusion might be a property of such time crystals. It is certainly important to gain more clarity on this question, both from an experimental and a theoretical perspective.

## 6 | CONCLUSION AND OUTLOOK

Synchronisation is at the heart of many effects occurring in nature but also in some particular physical, chemical, or biological systems. A fundamental understanding of synchronisation from both a theoretical and an experimental perspective is therefore key to understanding the behaviour of many systems in our environment. Due to a lack of suitable systems, it has to date proven challenging to experimentally study the transition to synchronisation in systems that provide a large number of constituent oscillators while also being widely tunable.

In Chapter 4 we have shown that an atomic three-level system subject to a level shift of the Rydberg state, scaling with a power-law in Rydberg density, undergoes bifurcations. These bifurcations lead to multistability in the system and, for some parameter ranges, to the formation of attractive limit cycles due to Hopf bifurcations. Systems caught by such limit cycle attractors are phase oscillators where the phase within the limit cycle is free and therefore easily adjusted by a force. Therefore, when coupling an ensemble of phase oscillators via a global mean field one finds that the resulting force and back-action dynamics can result in synchronisation of the ensemble for strong enough couplings.

In a hot vapour system with many velocity classes interacting via a global Rydberg density mean field, we observe that synchronisation of the velocity classes occurs for strong enough couplings between the velocity classes. This results in persistent oscillations of the bulk quantities of the simulated vapour. For instance, the simulations predict oscillations in the imaginary part of the ground-excited state coherence  $\rho_{ge}^i$  which is proportional to the transmission of a vapour.

Experimentally, we find oscillations in the transmission of the probe laser through an atomic vapour when performing two-photon EIT spectroscopy of Rydberg states in rubidium at temperatures in the range of 35 to 60 °C. The occurrence of these oscillations has been shown to depend strongly on the experimental conditions, as detailed in Chapter 5. The wide range of Rydberg atomic state properties, as outlined in Chapter 3, provides a tuning mechanism to change the system parameters very easily. The state dependent van der Waals interaction  $C_6$  can be contrasted with the equally state dependent electric polarisability to try and find the mechanism that causes the nonlinearity leading to the formation of limit cycles, and to understand how the global coupling mechanism works. We attribute the oscillations in the probe transmission to the emergence of synchronisation in our driven-dissipative hot Rydberg vapour since the hot vapour simulation phenomenologically reproduces the experimentally observed behaviour.

In this thesis, we have reported on the emergence of synchronisation in a driven-dissipative hot Rydberg vapour. The key features of this system allow to experimentally investigate the onset of synchronisation in large ensembles of globally coupled oscillators. Additionally, the

tunability of Rydberg states allow for targeted manipulation of the system parameters so that large ranges of parameter space are accessible with this system. Therefore, an avenue has been opened to easily explore and study the synchronisation transition in ensembles with large numbers of coupled phase oscillators. Improvements to the stability of the experimental parameters is expected to improve the phase stability of the oscillations, thereby paving the way to experimentally investigate the time crystal property of the oscillatory phase. However, open questions regarding the underlying mechanism causing the nonlinearity in the system remain and are currently contested. Further theoretical and experimental research into the system will help to establish the origin of the dominant driver of the nonlinearities.

We can therefore conclude that the reported results demonstrate the emergence of synchronisation in a driven-dissipative hot Rydberg vapour and can be linked to continuous dissipative time crystals, but we cannot yet establish the fundamental mechanism driving the system into the oscillatory state. This thesis is therefore well-concluded with the following quote by Emma Goldman:

*"Finalities are for gods and governments, not for the human intellect."*

# APPENDIX

# A | STEADY-STATE SOLUTIONS AND STABILITY ANALYSIS FOR DRIVEN SYSTEMS

In this appendix, further details of the theoretical study of the effective 2-level and the three-level model are given which leads to the results presented in Chapter 4. First, the equations of motion for the effective 2-level and the 3-level model are set out in detail and the steady state solutions are defined via the real zeros of a polynomial. The resulting steady states are discussed for different scalings with  $n$  and their stability properties are analysed using the methods outlined in Chapter 4.

For the effective 2-level model, it is shown that Hopf bifurcation cannot occur while the three-level model is shown to undergo Hopf bifurcation in certain parameter regimes.

The model as well as the calculations of the steady states make no assumptions on the laser powers, the results are therefore valid also in the strong probe regime. We assume the parameters to be in the following regimes:  $\Gamma, \Omega \in \mathbb{R}_+$ ,  $\tilde{\Delta}, V \in \mathbb{R}$ , and  $n \in \mathbb{N}_0$  unless stated otherwise

## A.1 EFFECTIVE 2-LEVEL SYSTEM

Treating real and imaginary part of the density matrix elements separately, the equations of motion for the effective 2-level model read

*Equations of motion*

$$\dot{\rho}_{gg}^r = -\Omega \rho_{ge}^i + \Gamma \rho_{ee}^r, \quad (\text{A.1a})$$

$$\dot{\rho}_{gg}^i = \Gamma \rho_{ee}^i, \quad (\text{A.1b})$$

$$\dot{\rho}_{ee}^r = \Omega \rho_{ge}^i - \Gamma \rho_{ee}^r, \quad (\text{A.1c})$$

$$\dot{\rho}_{ee}^i = -\Gamma \rho_{ee}^i, \quad (\text{A.1d})$$

$$\dot{\rho}_{ge}^r = \frac{1}{2}\Omega(\rho_{ee}^i - \rho_{gg}^i) - \frac{1}{2}\Gamma \rho_{ge}^r + \left(\tilde{\Delta} - V(\rho_{ee}^r)^n\right) \rho_{ge}^i, \quad (\text{A.1e})$$

$$\dot{\rho}_{ge}^i = -\frac{1}{2}\Omega(\rho_{ee}^r - \rho_{gg}^r) - \frac{1}{2}\Gamma \rho_{ge}^i - \left(\tilde{\Delta} - V(\rho_{ee}^r)^n\right) \rho_{ge}^r, \quad (\text{A.1f})$$

where we have made use of the fact that  $\rho_{jj}^i = 0$  to simplify  $V \rho_{ee}^n$  to  $V(\rho_{ee}^r)^n$ . Using the trace condition  $1 = \sum_j \rho_j$  and hermiticity of the density matrix as constraints, one can generally reduce this set of equations from six to three as stated in equations (4.3).

### Steady state solutions

The steady states of the effective 2-level model are determined by finding the steady states of the Lindblad equation. This is equivalent to solving the above system of equations for  $\dot{\rho}_{kl}^j = 0$  in  $\mathbb{R}$ . The resulting steady state solutions for all elements of the density matrix are determined by the roots of the polynomial

$$0 = (\rho_{ge}^i)^{2n+1} \left[ \frac{2}{\Gamma} V^2 \left( \frac{\Omega}{\Gamma} \right)^{2n} \right] - (\rho_{ge}^i)^{n+1} \left[ \frac{4}{\Gamma} V \tilde{\Delta} \left( \frac{\Omega}{\Gamma} \right)^n \right] + \rho_{ge}^i \left[ \frac{\Omega^2 + 2\tilde{\Delta}^2}{\Gamma} + \frac{\Gamma}{2} \right] - \frac{\Omega}{2}. \quad (\text{A.2})$$

The steady state values of the other elements of the density matrix follow via

$$\rho_{gg}^i = \rho_{ee}^i = 0, \quad (\text{A.3a})$$

$$\rho_{gg}^r = 1 - \rho_{ee}^r = 1 - \frac{\Omega}{\Gamma} \rho_{ge}^i, \quad (\text{A.3b})$$

$$\rho_{ee}^r = \frac{\Omega}{\Gamma} \rho_{ge}^i, \quad (\text{A.3c})$$

$$\rho_{ge}^r = \frac{2}{\Gamma} \left[ \tilde{\Delta} \rho_{ge}^i - V \left( \frac{\Omega}{\Gamma} \right)^n (\rho_{ge}^i)^{n+1} \right]. \quad (\text{A.3d})$$

The roots of the polynomial (A.2) depend on the value of  $n$ , i.e. on the power law scaling of the population-dependent level shift. Analytic solutions exist for  $n \in \{0, 1\}$ , and for  $n = 0$  this is given by

$$\rho_{ge}^i = \frac{\Omega/2}{\frac{\Omega^2 + 2(\tilde{\Delta} - V)^2}{\Gamma} + \frac{\Gamma}{2}}. \quad (\text{A.4})$$

For  $n = 1$  the three solutions are given by the well known roots of a cubic. The results are either a single real solution plus a complex-conjugate pair, or three real solutions.

For higher  $n$ , the order of the polynomial (A.2) is  $\geq 5$  and does not have a generic analytic solution. However, using Descartes' rule of signs [125] we know that a maximum of three positive real roots of the polynomial exists and, generally, always a minimum of one. For a physical interpretation of the populations as state probabilities we require a solution  $\rho_{ge}^i$  to lie in the interval  $\rho_{ge}^i \in [0, \frac{\Gamma}{\Omega}]$ , as can be seen from equation (A.3c).

It will now be shown that, for all  $n \in \mathbb{N}$ , the roots lie in the interval  $[0, \frac{\Gamma}{\Omega}]$  and that there is always a minimum of one root. For this, we define the polynomial

$$\mathcal{P}(x) = -\frac{\Omega}{2} + x \cdot \frac{2}{\Gamma} \left[ \frac{\Gamma^2}{4} + \frac{\Omega^2}{2} + \left( \tilde{\Delta} - V \left( \frac{\Omega}{\Gamma} x \right)^n \right)^2 \right] \quad (\text{A.5})$$

so that we recover equation (A.2) when setting  $\mathcal{P}(x) = 0$ . In fact, this polynomial is a simple reformulation of (A.2), which means that studying this polynomial gives information on the solutions of equation (A.2). Also, as we are interested in real solutions only, we demand that  $x \in \mathbb{R}$ .

The term in square brackets of the polynomial (A.5) is always positive, it therefore follows immediately that  $\mathcal{P}(x) < 0 \forall x \leq 0$ . Also, for non-vanishing system parameters  $\Omega, \Gamma$  it always holds

$$\mathcal{P}\left(\frac{\Gamma}{\Omega}\right) = \frac{1}{\Omega} \left( \frac{\Omega^2 + \Gamma^2}{2} + 2(\Delta - V)^2 \right) > 0.$$

For any  $\{\Omega, \Gamma\}$ , the term in square brackets is bounded from below by  $\Gamma^2/4 + \Omega^2/2$ , so one finds that for  $\mathcal{P}(x) < 0$  it must hold that

$$x < \frac{\Omega\Gamma}{2\Omega^2 + \Gamma^2} < \frac{\Gamma}{\Omega}.$$

Therefore,  $\mathcal{P}(x) > 0 \forall x \geq \frac{\Gamma}{\Omega}$ .

This result now guarantees that all real roots of the polynomial  $\mathcal{P}$  lie in the interval  $[0, \frac{\Gamma}{\Omega}]$  as is required for interpretation of the populations as probabilities, and guarantees the existence of at least one root since  $\mathcal{P}(x) < 0$  for  $x < 0$  and  $\mathcal{P}(x) > 0$  for  $x > \Gamma/\Omega$ . From Descartes' rule of signs we know that there is exactly one root for  $\text{sign}(V) \neq \text{sign}(\tilde{\Delta})$  and either one or three otherwise.

A fast numeric method to calculate all roots of a polynomial in  $\mathbb{C}$  utilizes the companion matrix of the polynomial of order  $k$

$$\mathcal{P}(\lambda) = \alpha_k \lambda^k + \dots + \alpha_1 \lambda + \alpha_0.$$

The companion matrix  $\mathcal{C}(\mathcal{P})$  is defined as the  $(k-1) \times (k-1)$ -dimensional square matrix

$$\mathcal{C}(\mathcal{P}) = \begin{pmatrix} 0 & 0 & \dots & 0 & -\alpha_0/\alpha_k \\ 1 & 0 & \dots & 0 & -\alpha_1/\alpha_k \\ 0 & 1 & \dots & 0 & -\alpha_2/\alpha_k \\ \vdots & \vdots & \ddots & \vdots & \vdots \\ 0 & 0 & \dots & 1 & -\alpha_{k-1}/\alpha_k \end{pmatrix}. \quad (\text{A.6})$$

A useful property of the companion matrix is that its characteristic polynomial  $\chi[\mathcal{C}(\mathcal{P})](\lambda)$  is equal to our initial polynomial  $\mathcal{P}(\lambda)$  but normalised, i.e.  $\chi[\mathcal{C}(\mathcal{P})](\lambda) = \alpha_{2n+1}^{-1} \mathcal{P}(\lambda)$ . The eigenvalues  $\lambda_i$  of  $\mathcal{C}(\mathcal{P})$  are equal to the roots of its characteristic polynomial  $\chi$  and therefore identical to the roots of our polynomial  $\mathcal{P}$ .

Fast numerical algorithms for the calculation of eigenvectors and eigenvalues exist, and we have not encountered stability issues of the numerical algorithms for the companion matrices resulting from our system parameters. It should be noted that the values for the density matrix elements obtained with the steady state approach presented above are in excellent agreement with the values for the attractive steady states obtained from time integration of the equations of motion (A.1).

One can also set  $n$  to a value  $n \notin \mathbb{N}$  and equation (A.2) remains valid. However, in order to use the companion matrix to calculate the steady state values, one must be able to re-formulate the

equation as a polynomial with integer coefficients of  $\rho_{ge}^i$ . Therefore, if one wishes to study a case with  $n \notin \mathbb{N}$  one has to re-formulate the polynomial (A.2) accordingly or employ an alternative method to find all real roots.

### Stability of the steady states

Applying the stability analysis presented in Section 4.2.2 to the effective 2-level approach described in Section 4.2.1, one finds the linearisation of the map

$$\Phi : \mathbb{R}^6 \rightarrow \mathbb{R}^6, \mathbf{x} \mapsto \Phi(\mathbf{x}) \quad \text{with} \quad \mathbf{x} = (\rho_{gg}^r, \rho_{gg}^i, \rho_e^r, \rho_{ee}^i, \rho_{ge}^r, \rho_{ge}^i)$$

given by  $J = \left( \frac{\partial \Phi_i}{\partial \mathbf{x}_j} \right)_{i,j}$ . For the remaining discussion we will fix the steady state  $\rho_0$ . Evaluation of  $J$  at  $\rho_0 = (\rho_{gg,0}^r, \rho_{gg,0}^i, \rho_{ee,0}^r, \rho_{ee,0}^i, \rho_{ge,0}^r, \rho_{ge,0}^i)$ , as defined through equations (A.2) and (A.3), results in

$$J_\mu(\rho_0) = \begin{pmatrix} 0 & 0 & \Gamma & 0 & 0 & -\Omega \\ 0 & 0 & 0 & \Gamma & 0 & 0 \\ 0 & 0 & -\Gamma & 0 & 0 & \Omega \\ 0 & 0 & 0 & -\Gamma & 0 & 0 \\ 0 & -\frac{\Omega}{2} & -nV\rho_{ge,0}^i \left( \frac{\Omega\rho_{ge,0}^i}{\Gamma} \right)^{n-1} & \frac{\Omega}{2} & -\frac{\Gamma}{2} & \tilde{\Delta} - V \left( \frac{\Omega\rho_{ge,0}^i}{\Gamma} \right)^n \\ \frac{\Omega}{2} & 0 & -\frac{\Omega}{2} - \frac{2nV}{\Omega} \left( \frac{\Omega\rho_{ge,0}^i}{\Gamma} \right)^n \left( -\tilde{\Delta} + V \left( \frac{\Omega\rho_{ge,0}^i}{\Gamma} \right)^n \right) & 0 & -\tilde{\Delta} + V \left( \frac{\Omega\rho_{ge,0}^i}{\Gamma} \right)^n & -\frac{\Gamma}{2} \end{pmatrix} \quad (\text{A.7})$$

The corresponding characteristic polynomial, equally evaluated at the steady state  $\rho_{ge,0}^i$

$$\chi[J](\lambda) = \lambda^2 (\Gamma + \lambda) \left[ \begin{aligned} & \lambda^3 + 2\lambda^2\Gamma \\ & + \lambda \left( \Omega^2 + \tilde{\Delta}^2 + \frac{5}{4}\Gamma^2 - 2(n+1)V\tilde{\Delta} \left( \frac{\Omega\rho_{ge,0}^i}{\Gamma} \right)^n + (2n+1)V^2 \left( \frac{\Omega\rho_{ge,0}^i}{\Gamma} \right)^{2n} \right) \\ & + \frac{\Gamma}{4} \left( 4\tilde{\Delta}^2 + 2\Omega^2 + \Gamma^2 - 8(n+1)V\tilde{\Delta} \left( \frac{\Omega\rho_{ge,0}^i}{\Gamma} \right)^n + 4(2n+1)V^2 \left( \frac{\Omega\rho_{ge,0}^i}{\Gamma} \right)^{2n} \right) \end{aligned} \right]. \quad (\text{A.8})$$

This polynomial can now be studied following the analysis for the stability of a steady state defined via  $\rho_{ge,0}^i$ . The three eigenvalues that are independent of the particular steady state value of  $\rho_{ge,0}^i$  arise from the over-determinedness of the system of equations (A.1) when using the additional constraints of hermiticity of  $\rho$  and the trace condition. With these constraints, the system (A.1) is actually a system determined by three independent variables which is reflected by the cubic factor of the characteristic polynomial (A.8) that determines the remaining three eigenvalues of the linearisation  $J$ .

The steady state is asymptotically stable if the real part of all  $j$  eigenvalues is smaller than zero, i.e.  $\lambda_j < 0$ . In our case, this applies only to the three eigenvalues that are dependent on the particular steady state  $\rho_0$ , i.e. the ones determined by the cubic in square brackets in (A.8). This is because the term in square brackets is equal to the characteristic polynomial one obtains when applying the trace condition and hermiticity of the density matrix to reduce the initial set of six equations (A.1) to a set of three equations in the three variables  $\rho_{gg}^r$ ,  $\rho_{ge}^r$ , and  $\rho_{ge}^i$ .

To analyse the stability of the steady states for  $\rho_{ge,0}^i$  we use the Routh-Hurwitz criterion [192] since it allows to give statements on the stability of a steady state without an explicit expression for the steady state, as is the case for our system when  $n \geq 2$ . Since the relevant characteristic polynomial of the linearisation  $J$  is a cubic

$$\chi[J](\lambda) = \lambda^3 + a_2\lambda^2 + a_1\lambda + a_0$$

the criterion states that all eigenvalues  $\lambda_j$  of  $J$  have a negative real part except for a purely imaginary pair iff<sup>1</sup>  $a_2 > 0$ ,  $a_0 > 0$  and  $a_2a_1 - a_0 = 0$ . In this case, a Hopf bifurcation occurs. If the last condition is changed to  $a_2a_1 - a_0 > 0$ , then all eigenvalues have a negative real part and the steady state is stable.

From the cubic factor of the polynomial (A.8) one sees immediately that  $a_2 = 2\Gamma > 0$  is satisfied whenever  $\Gamma > 0$ , i.e. whenever there is a non-vanishing decay from the excited state  $|e\rangle$ . In physical terms this is equivalent to demanding that the system is dissipative.

Looking at the term  $a_2a_1 - a_0$ , one finds this to be equal to  $a_2a_1 - a_0 = a_0 + \Gamma(\Omega^2 + 2\Gamma^2)$ , see also [131]. The condition  $a_2a_1 - a_0 = 0$  will never be satisfied since the condition  $a_0 > 0$  must also be met for a Hopf bifurcation to occur and  $\Gamma, \Omega \in \mathbf{R}_+$ . We can therefore conclude that the two-level model does not undergo a Hopf bifurcation for all choices of model parameters.

This result is critical for the comparison of the effective 2-level model and the 3-level model, and should therefore be highlighted. An effective two-level system described by (A.1) undergoes saddle-node bifurcations [127] when the number of steady state solutions changes between one and three, but it does not undergo a Hopf bifurcation. Therefore, we do not expect any time-periodic solutions (limit cycles) to be observed in a dissipative Hamiltonian system that is determined by the equations of motion detailed in (A.1).

Regarding the stability of the equilibrium points defined by (A.2), the condition  $a_2a_1 - a_0 > 0$  is satisfied whenever  $a_0 + \Gamma(\Omega^2 + 2\Gamma^2) > 0$ . The last property to check is therefore whether  $a_0 > 0$  since it then follows that  $a_0 + \Gamma(\Omega^2 + 2\Gamma^2) > 0$  given that we have assumed  $\Gamma, \Omega \in \mathbf{R}_+$ .  $a_0 > 0$  requires that

$$\begin{aligned} a_0 &= \frac{\Gamma}{4} \left( 4\tilde{\Delta}^2 + 2\Omega^2 + \Gamma^2 - 8(n+1)V\tilde{\Delta} \left[ \frac{\Omega\rho_{ge,0}^i}{\Gamma} \right]^n + 4(2n+1)V^2 \left[ \frac{\Omega\rho_{ge,0}^i}{\Gamma} \right]^{2n} \right) \\ &= \frac{\Gamma}{4} \left( 2\Omega^2 + \Gamma^2 + 4 \left[ \tilde{\Delta} - V \left( \frac{\Omega}{\Gamma} \rho_{ge}^i \right)^n \right] \cdot \left[ \tilde{\Delta} - (2n+1)V \left( \frac{\Omega}{\Gamma} \rho_{ge}^i \right)^n \right] \right) > 0. \end{aligned}$$

This is always satisfied for the case of  $\text{sign}(V) \neq \text{sign}(\tilde{\Delta})$ , which is also the case where only a single steady state solution exists. Therefore, this one solution must be attractive. For the case of multiple steady states, which may occur if  $\text{sign}(\tilde{\Delta}) = \text{sign}(V)$ , the stability of a steady state  $\rho_{ge,0}^i$  is tested by verifying whether or not above inequality holds.

## A.2 3-LEVEL SYSTEM

The three-level system outlined in Section 4.2.3 is studied using the same procedure as outlined above for the effective 2-level model. However, even though it is still technically possible

<sup>1</sup>if and only if

to write down the coefficients of the steady state polynomials and the characteristic polynomial of the linearisation, it becomes unfeasible in reality. Therefore, the equations of motion are presented and a closed-form expression for the steady state polynomial in terms of newly defined coefficients is given such that the results are reproducible.

The resulting steady state solutions and their stability are therefore studied numerically, using the methods presented in the above section on the effective 2-level model.

### Equations of Motion

The equations of motion of this model, separated by real and imaginary part for each element of the density matrix, read

$$\dot{\rho}_{gg}^r = -\Omega_p \rho_{ge}^i + \Gamma_{ge} \rho_{ee}^r + \Gamma_{gr} \rho_{rr}^r, \quad (\text{A.9a})$$

$$\dot{\rho}_{gg}^i = +\Gamma_{ge} \rho_{ee}^i + \Gamma_{gr} \rho_{rr}^i, \quad (\text{A.9b})$$

$$\dot{\rho}_{ee}^r = +\Omega_p \rho_{ge}^i - \Omega_c \rho_{er}^i - \Gamma_{ge} \rho_{ee}^r + \Gamma_{er} \rho_{rr}^r, \quad (\text{A.9c})$$

$$\dot{\rho}_{ee}^i = -\Gamma_{ge} \rho_{ee}^i + \Gamma_{er} \rho_{rr}^i, \quad (\text{A.9d})$$

$$\dot{\rho}_{rr}^r = +\Omega_c \rho_{er}^i - (\Gamma_{gr} + \Gamma_{er}) \rho_{rr}^r, \quad (\text{A.9e})$$

$$\dot{\rho}_{rr}^i = -(\Gamma_{gr} + \Gamma_{er}) \rho_{rr}^i, \quad (\text{A.9f})$$

$$\dot{\rho}_{ge}^r = +\frac{\Omega_p}{2} (\rho_{ee}^i - \rho_{gg}^i) - \frac{\Omega_c}{2} \rho_{gr}^i + \tilde{\Delta}_p \rho_{ge}^i - \frac{\Gamma_{ge}}{2} \rho_{ge}^r, \quad (\text{A.9g})$$

$$\dot{\rho}_{ge}^i = -\frac{\Omega_p}{2} (\rho_{ee}^r - \rho_{gg}^r) + \frac{\Omega_c}{2} \rho_{gr}^r - \tilde{\Delta}_p \rho_{ge}^r - \frac{\Gamma_{ge}}{2} \rho_{ge}^i, \quad (\text{A.9h})$$

$$\dot{\rho}_{er}^r = +\frac{\Omega_c}{2} (\rho_{rr}^i - \rho_{ee}^i) + \frac{\Omega_p}{2} \rho_{gr}^i + (\tilde{\Delta}_c - V(\rho_{rr}^r)^n) \rho_{er}^i - \frac{\Gamma_{ge} + \Gamma_{er} + \Gamma_{gr}}{2} \rho_{er}^r, \quad (\text{A.9i})$$

$$\dot{\rho}_{er}^i = -\frac{\Omega_c}{2} (\rho_{rr}^r - \rho_{ee}^r) - \frac{\Omega_p}{2} \rho_{gr}^r - (\tilde{\Delta}_c - V(\rho_{rr}^r)^n) \rho_{er}^r - \frac{\Gamma_{ge} + \Gamma_{er} + \Gamma_{gr}}{2} \rho_{er}^i, \quad (\text{A.9j})$$

$$\dot{\rho}_{gr}^r = +\frac{\Omega_p}{2} \rho_{er}^i - \frac{\Omega_c}{2} \rho_{ge}^i - \frac{\Gamma_{gr} + \Gamma_{er}}{2} \rho_{gr}^r + (\tilde{\Delta}_p + \tilde{\Delta}_c - V(\rho_{rr}^r)^n) \rho_{gr}^i, \quad (\text{A.9k})$$

$$\dot{\rho}_{gr}^i = -\frac{\Omega_p}{2} \rho_{er}^r + \frac{\Omega_c}{2} \rho_{ge}^r - \frac{\Gamma_{gr} + \Gamma_{er}}{2} \rho_{gr}^i - (\tilde{\Delta}_p + \tilde{\Delta}_c - V(\rho_{rr}^r)^n) \rho_{gr}^r. \quad (\text{A.9l})$$

Again, we have used the fact that the imaginary part of the populations is zero due to hermiticity of the density matrix to simplify  $V(\rho_{rr})^n$  to  $V(\rho_{rr}^r)^n$ . In this three-level case, one finds that the time-evolution of the system is actually determined by eight equations instead of the twelve given above. This reduction in equations comes from the hermiticity of the density matrix  $\rho$ , implying that  $\rho_{kk}^i = 0$ , and the trace condition which removes another degree of freedom from the system of equations.

### Steady state solutions

In order to determine the steady state solutions of the system, we again set the time derivative of the density matrix elements, i.e. the left hand side of (A.9), to zero and solve in  $\mathbb{R}$ . The result is more tedious to obtain due to the number of equations involved, but it is again possible to derive a polynomial in  $\rho_{er}^i$  which determines the steady states through its roots, and express the other density matrix elements via  $\rho_{er}^i$ . To find this polynomial, one first expresses the populations via the coherences

$$\rho_{gg}^r = 1 - \frac{\Omega_p}{\Gamma_{ge}} \rho_{ge}^i - \frac{\Omega_c}{\Gamma_{er} + \Gamma_{gr}} \left( 1 - \frac{\Gamma_{gr}}{\Gamma_{ge}} \right) \rho_{er}^i, \quad (\text{A.10a})$$

$$\rho_{ee}^r = \frac{1}{\Gamma_{ge}} \left( \Omega_p \rho_{ge}^i - \Omega_c \frac{\Gamma_{gr}}{\Gamma_{er} + \Gamma_{gr}} \rho_{er}^i \right), \quad (\text{A.10b})$$

$$\rho_{rr}^r = \frac{\Omega_c}{\Gamma_{er} + \Gamma_{gr}} \rho_{er}^i, \quad (\text{A.10c})$$

$$0 = \rho_{gg}^i = \rho_{ee}^i = \rho_{rr}^i, \quad (\text{A.10d})$$

and then solves the remaining (non-linear) system of six equations of the coherences

$$\left. \begin{array}{l} 0 = -a_1 \rho_{ge}^r + a_2 \rho_{ge}^i - a_6 \rho_{gr}^i \\ 0 = +b_0 - b_1 \rho_{ge}^r - b_2 \rho_{ge}^i + b_4 \rho_{er}^i + b_5 \rho_{gr}^r \\ 0 = +c_3 \rho_{er}^r + c_4 \rho_{er}^i + c_6 \rho_{gr}^i \\ 0 = +d_2 \rho_{ge}^i - d_3 \rho_{er}^r - d_4 \rho_{er}^i + d_5 \rho_{gr}^r \\ 0 = -e_2 \rho_{ge}^i + e_4 \rho_{er}^i - e_5 \rho_{gr}^r + e_6 \rho_{gr}^i \\ 0 = +f_1 \rho_{ge}^r - f_3 \rho_{er}^r - f_5 \rho_{gr}^r - f_6 \rho_{gr}^i \end{array} \right\}. \quad (\text{A.11})$$

The coefficients are indexed by column from 0 (leftmost) to 6 (rightmost), and from  $a$  (top) to  $f$  (bottom) row. In the following, only the coefficients  $x_j$  will be used as indicated above to avoid clutter. With  $V' = V \left( \frac{\Omega_c}{\Gamma_{er} + \Gamma_{gr}} \rho_{er}^i \right)^n$  one obtains the coefficients defined as

$$\begin{aligned} a_1 &= \frac{\Gamma_{ge}}{2} & a_2 &= \tilde{\Delta}_p & a_6 &= \frac{\Omega_c}{2} \\ b_0 &= \frac{\Omega_p}{2} & b_1 &= \tilde{\Delta}_p & b_2 &= \left( \frac{\Gamma_{ge}}{2} + \frac{\Omega_p^2}{\Gamma_{ge}} \right) \\ b_4 &= \frac{\Omega_p \Omega_c}{\Gamma_{er} + \Gamma_{gr}} \left( \frac{\Gamma_{gr}}{\Gamma_{ge}} - \frac{1}{2} \right) & b_5 &= \frac{\Omega_c}{2} \\ c_3 &= \frac{\Gamma_{ge} + \Gamma_{er} + \Gamma_{gr}}{2} & c_4 &= (\tilde{\Delta}_c - V') & c_6 &= \frac{\Omega_p}{2} \\ d_2 &= \frac{\Omega_p \Omega_c}{2 \Gamma_{ge}} & d_3 &= (\tilde{\Delta}_c - V') \\ d_4 &= \frac{1}{2} \left( \frac{\Omega_c^2}{\Gamma_{er} + \Gamma_{gr}} \left( \frac{\Gamma_{gr}}{\Gamma_{ge}} + 1 \right) + \Gamma_{ge} + \Gamma_{er} + \Gamma_{gr} \right) & d_5 &= \frac{\Omega_p}{2} \\ e_2 &= \frac{\Omega_c}{2} & e_4 &= \frac{\Omega_p}{2} & e_5 &= \frac{\Gamma_{gr} + \Gamma_{er}}{2} & e_6 &= (\tilde{\Delta}_p + \tilde{\Delta}_c - V') \\ f_1 &= \frac{\Omega_c}{2} & f_3 &= \frac{\Omega_p}{2} & f_5 &= (\tilde{\Delta}_p + \tilde{\Delta}_c - V') & f_6 &= \frac{\Gamma_{gr} + \Gamma_{er}}{2} \end{aligned}$$

When solving this system of equations one must be careful with the terms containing  $V'$  since this is proportional to  $(\rho_{er}^i)^n$  and renders the system of equations (A.11) nonlinear for  $n \neq 0$ .

With the additional definitions

$$\begin{aligned}
 b_4^* &= b_4 - \left( b_2 + b_1 \frac{a_2}{a_1} \right) \frac{e_4}{e_2} & b_5^* &= b_5 + \left( b_s + b_1 \frac{a_2}{a_1} \right) \frac{e_5}{e_2} \\
 b_6^* &= b_1 \frac{a_6}{a_1} - \left( b_2 + b_1 \frac{a_2}{a_1} \right) \frac{e_6}{e_2} & d_4^* &= d_4 + d_3 \frac{c_4}{c_3} - d_2 \frac{e_4}{e_2} \\
 d_5^* &= d_5 + d_2 \frac{e_5}{e_2} & d_6^* &= d_3 \frac{c_6}{c_3} - d_2 \frac{e_6}{e_2} & f_4^* &= f_3 \frac{c_4}{c_3} - f_1 \frac{a_2}{a_1} \frac{e_4}{e_2} \\
 f_5^* &= f_5 + f_1 \frac{a_2}{a_1} \frac{e_5}{e_2} & f_6^* &= f_6 + f_1 \frac{a_6}{a_1} + f_3 \frac{c_6}{c_3} - f_1 \frac{a_2}{a_1} \frac{e_6}{e_2}
 \end{aligned}$$

for reduction of the length of the expressions, one arrives at the following polynomial in  $\rho_{er}^i$  which defines the steady state solutions of the three-level system. The polynomial is given by

$$\begin{aligned}
 0 = & b_0 d_5^* (f_6^* d_5^* - f_5^* d_6^*) \\
 & + \rho_{er}^i [(b_4^* d_5^* - b_5^* d_4^*) (f_6^* d_5^* - f_5^* d_6^*) - (f_4^* d_5^* - f_5^* d_4^*) (b_6^* d_5^* - b_5^* d_6^*)],
 \end{aligned} \tag{A.14}$$

and the steady state values of the remaining coherences follow as

$$\rho_{ge}^r = \frac{1}{a_1} (a_2 \rho_{ge}^i - a_6 \rho_{gr}^i), \tag{A.15a}$$

$$\rho_{ge}^i = \frac{1}{e_2} (e_4 \rho_{er}^i - e_5 \rho_{gr}^r + e_6 \rho_{gr}^i), \tag{A.15b}$$

$$\rho_{er}^r = \frac{1}{c_3} (c_4 \rho_{er}^i + c_6 \rho_{rg}^i), \tag{A.15c}$$

$$\rho_{gr}^r = - \frac{1}{d_5^*} (d_4^* \rho_{er}^i + d_6^* \rho_{gr}^i), \tag{A.15d}$$

$$\rho_{gr}^i = - \left[ f_6^* - f_5^* \frac{d_6^*}{d_5^*} \right]^{-1} \left( f_4^* - f_5^* \frac{d_4^*}{d_5^*} \right) \rho_{er}^i, \tag{A.15e}$$

with the populations already defined above in equations (A.10).

If one wants to include dephasing of the coherences, one simply has to re-define the appropriate coefficients and proceed as before.

The polynomial (A.14), defining the steady state values, is of the form

$$\mathcal{P}(\rho_{er}^i) = \sum_{k \in N} \alpha_k (\rho_{er}^i)^k$$

with  $N = \{4n+1, 3n+1, 2n+1, 2n, n+1, n, 1, 0\}$ , and is therefore of order  $\max(4n+1, 1)^2$ . This polynomial has eight terms which allows for a maximum of seven sign flips in the sequence of coefficients. Hence, a maximum of seven positive, real roots exist according to Descartes' rule of signs.

<sup>2</sup>Distinguishing these cases becomes relevant if one studies the system for negative  $n$ , for instance.

General expressions for all eight coefficients  $\alpha_j$  exists and can easily be obtained with the help of symbolic mathematics programs like Mathematica. The expressions for most coefficients are, however, too long to present them here.

The steady state values were calculated with an implementation of the companion matrix approach in Python, therefore only systems with  $n \in \mathbb{N}_0$  could be studied numerically.

#### *Stability of the steady states*

For the linearisation of the map and the resulting characteristic polynomial, the same holds as for the steady state polynomial: in principle, it is possible to write down an analytic closed-form expression, but they become too tedious to work with. Therefore, the linearisation was implemented in Python and the eigenvalues were obtained using numpy functions.

The steady state values calculated via the polynomial (A.14) were again in excellent agreement with the values for the locally attractive steady states of the system obtained by numerical integration of the equations of motion. Therefore, the polynomial procedure is not just reliable but also much preferable as it is computationally significantly less expensive and faster than integration of the system. Additionally, it returns information on all steady states of the system and not just the locally attractive ones.

## B | INTERACTION HAMILTONIAN FOR VAN DER WAALS-TYPE INTERACTIONS

When being in the van der Waals interaction regime<sup>1</sup>, the Rydberg-Rydberg interaction scales as  $C_6/r_{kl}^6$  for a pair of atoms ( $k, l$ ) at distance  $r_{kl}$ . Therefore, the system's many-body Hamiltonian including two-body interactions is given as

$$\mathcal{H}_{tot.} = \sum_k \left( \mathcal{H}_{AL}^{(k)} + \mathcal{H}_{int.}^{(k)} \right) \quad (\text{B.1})$$

with the interaction<sup>2</sup> term for atom  $k$  defined as

$$\mathcal{H}_{int.}^{(k)} = -\frac{\hbar}{2} \sum_{l \neq k} \frac{C_6^{(k,l)}}{r_{kl}^6} |r\rangle_{kk} \langle r| \otimes |r\rangle_{ll} \langle r|. \quad (\text{B.2})$$

For few particles, the full quantum dynamics can be computed on classical supercomputers. However, due to the exponential growth of Hilbert space with the number of particles, this task quickly becomes unfeasible. One solution to this problem is to use quantum simulators, that is quantum systems which 'naturally' implement the Hamiltonian of interest in a system that is easier to handle than the eoriginal one. Given the restrictions of such a quantum simulator and further questions such as experimental imperfections or impact of finite size effects, there has been a lot of work done on the theoretical side to complement quantum simulators by approximating the behaviour of quantum systems such that larger system sizes become handleabl for classical computers. One approximation often done in the literature is the mean-field approximation, where one replaces the two-body correlator

$$|r\rangle_{kk} \langle r| \otimes \sum_l |r\rangle_{ll} \langle r|$$

<sup>1</sup>This requires that the average spacing between Rydberg atoms is larger than the LeRoy radius, which is a measure for the distance two atoms must have such that their Rydberg state wavefunctions do not overlap.

<sup>2</sup>This interaction between pairs of atoms in the cloud can generate entanglement, causing the many-body density matrix  $\rho$  to loose the block-diagonal structure  $\rho_{C_6=0} = \otimes_k \rho^{(k)}$  which is a property of non-interacting systems.

with the expectation value for the density operator<sup>3</sup>, i.e.  $\hat{n}_{rr}^{(l)} \rightarrow \langle \hat{n}_{rr}^{(l)} \rangle_{\rho^{(l)}} = \rho_{rr}^{(l)}$ . This approximation changes the interaction Hamiltonian to a mean-field Hamiltonian

$$\mathcal{H}_{int.}^{(k)} = -\frac{\hbar}{2} |r\rangle_{kk} \langle r| \sum_{l \neq k} \frac{C_6^{(k,l)}}{r_{kl}^6} \rho_{rr}^{(l)}. \quad (\text{B.3})$$

This expression is still comparably complex since one has to compute the full sum in the interaction part of the Hamiltonian for every time step and every sample run. The mean-field approach is employed in e.g. the dTWA formalism, which allows to simulate several thousands of particles at once [193].

From the form of equation (B.3), one can now proceed in two different ways to further simplify the system<sup>4</sup>.

#### *Nearest-neighbor interaction at average Rydberg atom spacing*

The first, very simplistic approach assumes that the interaction with the nearest neighbor Rydberg atom contributes much stronger than all other interactions, such that interactions with Rydberg atoms other than the nearest neighbor can be neglected. The second assumption is that the nearest Rydberg atom is found at the average Rydberg atom spacing<sup>5</sup>  $\langle r_{Ryd.} \rangle = \frac{5}{9} (\rho_v f_{Ryd})^{-1/3}$ , where  $\rho_v$  denotes the vapour density and  $f_{Ryd}$  the fraction of atoms in the Rydberg state. Assuming the fraction of atoms in the Rydberg state to be uniform across the vapour, this is then equal to the expectation value of the Rydberg state for atom  $k$ .

Given the assumptions above, the simplified mean-field interaction Hamiltonian is given by

$$\mathcal{H}_{int.}^{(k)} = -\frac{\hbar}{2} |r\rangle_{kk} \langle r| \left( \frac{9}{5} \right)^6 C_6 \rho_v^2 (\rho_{rr}^{(k)})^3. \quad (\text{B.4})$$

To work with this expression without having to deal with all  $k$  atoms in the sample, we make the last approximation of removing the sum over all  $k$  atoms in the many-body Hamiltonian and justify this by stating that, statistically, the situation will be the same for all atoms and therefore it suffices to consider a single one. This leads to the following, final formulation of the simplified mean-field Hamiltonian

$$\mathcal{H}_{tot.} = \mathcal{H}_{AL} - |r\rangle \langle r| \frac{\hbar}{2} \left( \frac{9}{5} \right)^6 C_6 \rho_v^2 \rho_{rr}^3. \quad (\text{B.5})$$

When adding the incoherent decay and dephasing terms through the Lindblad operator terms, one can identify this approach with the three-level model with the parameters  $n = 3$  and  $V = \frac{\hbar}{2} \left( \frac{9}{5} \right)^6 C_6 \rho_v^2$ . The unit check for this approximation is positive,  $V$  has the unit of an energy in Hz.

<sup>3</sup>The density operator of the  $l$ -th atom  $\hat{n}_{rr}^{(l)}$  is defined as  $\hat{n}_{rr}^{(l)} = |r\rangle_l \langle r|$  such that  $\langle \hat{n}_{rr}^{(l)} \rangle_{\rho} = \text{Tr} [\hat{n}_{rr}^{(l)} \rho^{(l)}] = \rho_{rr}^{(l)}$  and  $\rho^{(l)} = \text{Tr}_{j \neq l} [\rho]$ .

<sup>4</sup>Note that we were interested in a practical and handleable approach to the problem, and not the most accurate form one could find.

<sup>5</sup>This equation comes from the expression for the average distance of atoms in a uniform random sample with density  $\rho_v$ ,  $\langle r \rangle = \frac{5}{9} (\rho_v)^{-1/3}$  [194].

*Statistical distribution of Rydberg atoms with uniform density*

Above expression for the interaction Hamiltonian has successfully reduced the scope of the problem from a full-grown  $N$ -particle many-body problem to an effective one-body equation of motion. However, the assumptions of only nearest-neighbour interaction, and the nearest-neighbour atom distance being the average spacing of Rydberg atoms in the vapour, are both very crude.

One can better represent the situation by considering the statistical distribution of interatomic distances in a cloud of uniform density  $\rho_v$ . An expression for the probability of finding  $n$  atoms within distance  $r$  of the central atom in a  $d$ -dimensional space has been derived in Appendix D for the large particle limit. There, it is found that the probability of finding exactly  $n$  atoms within radius  $r$  of the atom of interest is given by the Poisson distribution

$$\mathcal{P}_\mu(n) := \text{Poisson}_\mu(n) = \frac{1}{n!} \mu^n \exp(-\mu)$$

where the mean<sup>6</sup>  $\mu(r) = \frac{4}{3}\pi\rho_x r^3$  in  $\mathbb{R}^3$  and  $\rho_x$  denotes the density of interest, i.e. the atomic density or Rydberg atom density. The likelihood of finding exactly  $n$  atom(s) in the shell of radius  $r$  and thickness  $dr \rightarrow 0$  follows by taking the derivative of the above, i.e.

$$\begin{aligned} p_{\mu(r)}(n)dr &= \frac{d}{dr} \left[ \frac{1}{n!} \mu(r)^n \exp(-\mu(r)) \right] dr \\ &= \left( \frac{n}{\mu(r)} - 1 \right) \left( \frac{d}{dr} \mu(r) \right) \mathcal{P}_{\mu(r)}(n) dr \\ &= \left( \frac{d\mu(r)}{dr} \right) \cdot [\mathcal{P}_{\mu(r)}(n-1) - \mathcal{P}_{\mu(r)}(n)] dr. \end{aligned} \tag{B.6}$$

For future calculations it is relevant to note that the Poisson distribution is normalised for every  $\mu > 0$  such that  $1 = \sum_n \mathcal{P}_\mu(n)$ .

The interaction  $V(r_i)$  contributed by atoms in the shell  $[r_i, r_i + \Delta r_i]$  can be approximated by the sum

$$V(r_i)\Delta r_i = \sum_j \frac{C_6}{r_i^6} \Big|_{r_j \in [r_i, r_i + \Delta r_i]} \Delta r_i \tag{B.7}$$

for  $\Delta r_i \rightarrow 0$ . With the statistical distribution of atoms given in equation (B.6), one can immedi-

<sup>6</sup>In the general case for  $d$ -dimensions, one finds that  $\mu(r) = \rho \bar{\mathcal{B}}_r$  in  $\mathbb{R}^d$  with  $\bar{\mathcal{B}}_r$  the closed,  $d$ -dimensional ball of radius  $r$  around the origin. So for  $d = 1$  :  $\mu(r) = 2\rho_x r$ , for  $d = 2$  :  $\mu(r) = \pi\rho_x r^2$  and for  $d = 3$  :  $\mu(r) = \frac{4}{3}\pi\rho_x r^3, \dots$

ately calculate the interaction strength contributed by atoms at distance  $r$  for  $dr \rightarrow 0$  via

$$\begin{aligned}
\bar{V}(r)dr &= \frac{C_6}{r^6} \sum_{n \geq 1} n p_{\mu(r)}(n) dr \\
&= \frac{C_6}{r^6} \left( \frac{d}{dr} \mu(r) \right) \sum_{n \geq 1} [n \mathcal{P}_{\mu(r)}(n-1) - n \mathcal{P}_{\mu(r)}(n)] dr \\
&= \frac{C_6}{r^6} \left( \frac{d}{dr} \mu(r) \right) \left[ \sum_{n \geq 0} (n+1) \mathcal{P}_{\mu(r)}(n) - \sum_{n \geq 0} n \mathcal{P}_{\mu(r)}(n) \right] dr \\
&= \frac{C_6}{r^6} \left( \frac{d}{dr} \mu(r) \right) \left[ \sum_{n \geq 0} \mathcal{P}_{\mu(r)}(n) \right] dr \\
&= \frac{C_6}{r^6} \left( \frac{d}{dr} \mu(r) \right) dr
\end{aligned} \tag{B.8}$$

where the sum over  $n \geq 0$  in the second-to-last line evaluates to 1. The total interaction strength induced on the atom by its environment then follows by integration over space where we assume that  $\bar{V} = \bar{V}(r) \cdot \bar{V}(\theta, \phi)$  is separable into a radial and an angular component. Then, one finds for three-dimensional space with  $\mu(r) = \frac{4}{3} \pi \rho_x r^3$  that

$$\begin{aligned}
\bar{V} &= \int_0^\pi d\theta \int_0^{2\pi} d\phi \bar{V}(\theta, \phi) \int_{r_1}^{r_2} dr \bar{V}(r) \\
&= I_{(\theta, \phi)} \int_{r_1}^{r_2} dr 4\pi \rho_x r^2 \frac{C_6}{r^6} \\
&= -\frac{4}{3} \pi \rho_x C_6 I_{(\theta, \phi)} \cdot r^{-3} \Big|_{r_1}^{r_2}.
\end{aligned} \tag{B.9}$$

The upper bound  $r_2$  is theoretically given by infinity, and the lower bound must be greater than zero<sup>7</sup>. A reasonable choice for  $r_1$ , given the problem we are dealing with, is to set  $r_1$  equal to the Rydberg blockade radius, as no second atom can be excited into the Rydberg state within the blockade radius and hence this volume is empty of particles contributing to a Rydberg-interaction induced level shift  $\bar{V}$  anyways. In future, the lower bound  $r_1$  will therefore be chosen to match the blockade radius  $r_b$ , i.e.  $r_1 = r_b = \left(\frac{C_6}{\Omega}\right)^{1/6}$ . The Rabi frequency  $\Omega$  in the expression for the blockade radius  $r_b$  denotes the two-level effective Rabi frequency  $\Omega = \frac{\Omega_p \Omega_c}{2\Delta}$  and the resulting interaction experienced by an atom in the vapour then follows as

$$\bar{V} = \frac{4}{3} \pi \rho_x C_6 I_{(\theta, \phi)} \cdot r_b^{-3} = \frac{4}{3} \pi \rho_v \rho_{rr} I_{(\theta, \phi)} \sqrt{\hbar C_6 \Omega}. \tag{B.10}$$

The resulting interaction part of the Hamiltonian is then given by

$$\mathcal{H}_{int.} = -\frac{4\pi\rho_v}{3} I_{(\theta, \phi)} \sqrt{\hbar \Omega C_6 \rho_{rr}^2} |r\rangle \langle r| \tag{B.11}$$

<sup>7</sup>Else, one runs into an infinity which is very unphysical and is a speciality of QFTs and the likes.

where the second factor of  $\rho_{rr}$  follows from equation (B.3). In the idealised case of angular dependence-free Rydberg-Rydberg interactions, the integral  $I_{(\theta,\phi)}$  evaluates to  $4\pi$ . For reasons of simplicity, this will be assumed for future calculations. Also, the unit check for this result is equally positive, the interaction term contributes an energy in the unit Hz.

The resulting scaling of the interaction strength is only quadratic in the Rydberg state population, rather than cubic as in the very crude derivation presented above. In this derivation, the Rydberg blockade effect is partially taken into account by setting the lower bound of the integral in (B.9) to the blockade radius  $r_b$ . Therefore, the interaction will in future be assumed to follow a square power law in  $\rho_{rr}$  and the interaction Hamiltonian be given by equation (B.11). However, one should bear in mind that the probability of finding  $n$  particles at distance  $r$  as derived in Appendix D holds for Rydberg atoms only in the regime far from saturation of the Rydberg atom density.

## C | APPROXIMATION OF THE PLASMA MODEL

In [63], the authors have proposed plasma formation due to ionisation of Rydberg atoms in the thermal vapour as the main mechanism leading to bistability. The lineshapes resulting from their theory match the presented data well, additionally they present some experimental evidence indicating the presence of a plasma in their hot Rydberg vapour.

The procedure to determine the steady state presented in [63] does not provide a route to an intuitive understanding of the system's dynamics. It does, however, provide a phenomenological explanation for a mechanism underlying the bistability observed in hot Rydberg vapours. It is therefore interesting to see if we can model the plasma formation approach and study it with our methods.

The model proposed in [63] includes an additional population of ions as a fourth level, which we haven't included in the three-level model. Therefore, the steady state ion population has to be re-expressed in terms of the Rydberg state population and the resulting Stark shift given as a function of  $\rho_{rr}^r$ . Further details on the model itself can be found in [63] and appendices thereof. We will here derive the scaling of the level shift resulting from Stark effects due to the presence of ions, but will not discuss their model in detail.

The level shift due to Stark effects is assumed to be given by the average of the Stark shift  $\Delta_S(E)$  at a given field strength  $E$ , weighted by the probability  $P_N(E)$  of finding this field strength given an ion density  $\mathcal{N}_{ion}$ . I.e.

$$\bar{\Delta}_S = \int_0^\infty dE P_{\mathcal{N}_{ion}}(E) \Delta_S(E). \quad (\text{C.1})$$

The probability distribution for the charge-induced microfields

$$P_{\mathcal{N}_{ion}}(E)dE = \frac{1}{Q_H} \mathcal{H}\left(\frac{E}{Q_H}\right) dE \quad (\text{C.2})$$

is determined by the Holtsmark [195] probability distribution  $\mathcal{H}(\beta)$ , which is extensively used in plasma physics to describe the fields created by the charged particles in a plasma. The Holtsmark distribution is defined as

$$\mathcal{H}(\beta) = \frac{2\beta}{\pi} \int_0^\infty dx x \sin(\beta x) \exp(-x^{3/2}). \quad (\text{C.3})$$

Analytic expressions for the Holtsmark distribution exist [196], but the behaviour of the function is no more intuitive in the analytic than in the integral form. The normal field  $Q_H$  depends on

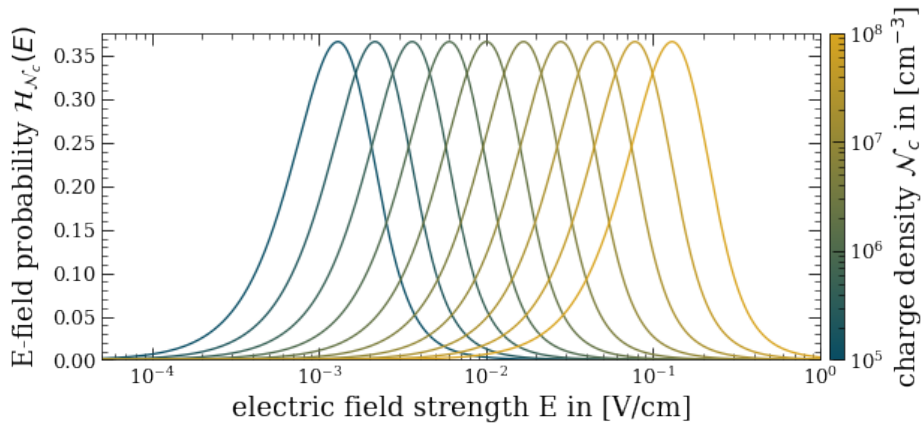


**Fig. C.1: Electric microfield strength distribution induced by different charge densities.** The probability of finding a given electric field strength  $E$  is shown for various charge densities  $\mathcal{N}_{ion}$ . For the experimental parameters of this thesis, only electric fields with  $E \ll 1$  V/cm have significant probabilities of occurrence.

the ion density  $\mathcal{N}_{ion}$  and is defined as

$$Q_H = \frac{e}{2\epsilon_0} \left( \frac{4}{15} \mathcal{N}_{ion} \right)^{2/3} \quad (\text{C.4})$$

with the elementary charge  $e$ , vacuum permittivity of free space  $\epsilon_0$  and ion density  $\mathcal{N}_{ion}$  in  $1/\text{m}^3$ . The plasma-induced electric field distribution is shown in figure C.1 and is  $\ll 1$  V/cm for the experimental parameters in this thesis.

In [197], an analytic approximation of the average Stark shift  $\bar{\Delta}_S$  depending of the ion number density  $\mathcal{N}_c$  is given to scale as

$$\bar{\Delta}_S(\mathcal{N}_{ion}) \propto -\alpha \mathcal{N}_{ion}^{4/3} \quad (\text{C.5})$$

with  $\alpha$  denoting the polarisability of the respective Rydberg state.

This simplifies the problem significantly since we need now only find an expression for the ion number density  $\mathcal{N}_{ion}$  in terms of the Rydberg population  $\rho_{rr}^r$  and find the appropriate power law scaling for  $\bar{\Delta}_s \propto (\rho_{rr}^r)^n$ . We start with the expression for the ion density  $\mathcal{N}_{ion}$  or, equivalently, the ion state population  $\rho_{ion}^r$  since  $\mathcal{N}_{ion} = \rho_{ion}^r \mathcal{N}_{tot}$ , in terms of the Rydberg state population  $\rho_{rr}^r$ .

In the steady state, we have

$$\Gamma_d \rho_{ion} = \Gamma_i \rho_{rr}^r \quad (\text{C.6})$$

with the decay rates

$$\Gamma_d \approx 2\Gamma_t = \frac{2}{\omega} \sqrt{\frac{k_B T}{\pi m_{ion} \ln(2)}},$$

$$\Gamma_i = \mathcal{N}_{tot} \sqrt{\frac{8k_B T}{\pi}} \left( \sigma_g \sqrt{\frac{2}{m_{ion}}} + \sigma_e \frac{1}{\sqrt{m_e}} \rho_{ion}^r \right)$$

The variables are defined<sup>1</sup> and reasonable values given in [63]. Since the one summand in the decay rate  $\Gamma_i$  depends on the ion state population, we have to re-formulate equation C.6 as

$$\rho_{rr} = a_1 \frac{\rho_{ion}^r}{1 + a_2 \rho_{ion}^r} \quad (\text{C.8})$$

with

$$a_1 = \frac{2\Gamma_t}{\sigma_g \mathcal{N}_{tot}} \sqrt{\frac{\pi m_{ion}}{16k_B T}} = \frac{1}{2\sqrt{\ln(2)}\omega \mathcal{N}_{tot}\sigma_g} \quad \text{and} \quad a_2 = \frac{\sigma_e}{\sigma_g} \sqrt{\frac{m_{ion}}{2m_e}}.$$

For the heavier alkalis, and at principal quantum number around  $n = 50$ , one finds  $a_2 \approx 5000$ . Therefore, the fraction in  $\rho_{ion}$  can be expanded in a Taylor expansion<sup>2</sup> around zero, resulting in the polynomial

$$\rho_{rr}^r = a_1 (\rho_{ion}^r - a_2 (\rho_{ion}^r)^2). \quad (\text{C.9})$$

Only the smaller valued root of this polynomial leads to a physically interpretable result with  $\rho_{ion}^r \in [0, 1]$  and is given by another Taylor expansion<sup>3</sup> to second order.

$$\rho_{ion} = \frac{1}{2a_2} \left( 1 - \sqrt{1 - \frac{4a_2}{a_1} \rho_{rr}^r} \right) \approx \frac{1}{a_1} \rho_{rr}^r + \frac{1}{4a_1} (\rho_{rr}^r)^2 + \mathcal{O}((\rho_{rr}^r)^3) \quad (\text{C.10})$$

Plugging this back into equation C.5 for the average Stark shift, we find the expression

$$\bar{\Delta}_S(\rho_{rr}^r) \propto -\alpha \mathcal{N}_{tot}^{4/3} (\rho_{ion}^r)^{4/3} \quad (\text{C.11a})$$

$$\approx -\alpha \mathcal{N}_{tot}^{4/3} \left( \frac{1}{a_1} \rho_{rr}^r + \frac{1}{4a_1} (\rho_{rr}^r)^2 \right)^{4/3} \quad (\text{C.11b})$$

$$\approx -\alpha \left( \frac{\mathcal{N}_{tot} \rho_{rr}^r}{a_1} \right)^{4/3} \left( 1 + \frac{1}{3} \rho_{rr}^r + \mathcal{O}((\rho_{rr}^r)^2) \right) \quad (\text{C.11c})$$

where the last step is another approximation. For small Rydberg state populations such that the Taylor approximations hold, the Stark shift induced detuning off the Rydberg state can be well approximated as scaling with a power law  $n = 4/3$ .

<sup>1</sup>Here,  $\mathcal{N}_{tot}$  denotes the ground state density, on the order of  $10^{10} - 10^{12} \text{ 1/(cm)}^3$ ;  $\omega$  the minimal beam waist, usually on order of  $0.1 - 1 \text{ mm}$ ;  $k_B$  the Boltzmann constant and  $T$  the temperature in K, for hot vapour systems on the order of  $300 - 400 \text{ K}$ ;  $m_{ion}$  and  $m_e$  the masses of the ionic core and electron, respectively;  $\sigma_g = 0.06\sigma_{geo}$  and  $\sigma_e = (1 - 10)\sigma_{geo}$  denote the ionisation cross section of Rydberg atoms with ground state atoms and electrons, respectively.  $\sigma_{geo} = \pi a_0^2 (n^*)^4$  denotes the geometric cross section of the Rydberg state with Bohr radius  $a_0$  and effective principal quantum number  $n^*$ .

<sup>2</sup>The Taylor converges since  $\rho_{ion}^r \leq \frac{1}{3} 10^{-4}$  for the experimental parameters in [63] such that the convergence criterion  $|a_2| < 1/|\rho_{ion}^r|$  of the Taylor series is satisfied.

<sup>3</sup>This Taylor expansion converges as well since we find, for reasonable experimental parameters, that  $a_1 \approx 200$  and  $\rho_{rr}^r \approx 2.8 \cdot 10^{-3}$  such that the convergence criterion is again satisfied.

## D | SPATIAL DISTRIBUTION OF ATOMS IN A THERMAL VAPOUR

In a thermal vapour with random distribution of particles, one can derive the probability of finding exactly  $n$  particles within distance  $r$  of an initial particle. One has to make the assumption of a uniform spatial probability distribution, i.e. that a particle has equal likelihood of being found at any given position in space, which implies a uniform particle number density. An expression for this is derived in the following.

Starting with a fixed volume  $V_{tot}$  containing a total number of atoms  $N_{tot}$ , one defines the particle number density via  $N_{tot} = \rho V_{tot}$ . Since the probability of finding a single atom in a volume  $V$  is uniform over all space, it is given by  $p_v = p(V) = V/V_{tot}$ . The probability of finding  $n$  particles within a  $d$ -dimensional sphere of radius  $r$  and the remaining  $N_{tot} - n$  particles in the remaining volume  $V_{tot}/V$  (where  $/$  here denotes the mathematical exclusion), is

$$P(\text{exactly } n \text{ particles in volume } V_d) = \binom{N_{tot}}{n} (p_v)^n (1 - p_v)^{N_{tot}-n} \quad (\text{D.1})$$

with  $p_v$  being the probability of finding a particle within the  $d$ -dimensional volume  $V_d$ , i.e.  $p_v = V_d/V_{tot}$ . Substituting the values for  $p_v$ , one finds

$$\begin{aligned} p(n; V_d, \rho) &= \frac{N_{tot}!}{n!(N_{tot} - n)!} \left(\frac{V_d}{V_{tot}}\right)^n \left(1 - \frac{V_d}{V_{tot}}\right)^{N_{tot}-n} \\ &= \frac{1}{n!} N_{tot} \cdot \dots \cdot (N_{tot} - n + 1) \left(\frac{\rho V_d}{N_{tot}}\right)^n \left(1 - \frac{\rho V_d}{N_{tot}}\right)^{N_{tot}-n}. \end{aligned}$$

For the large particle limit with  $n \ll N$  where  $N \rightarrow \infty$ , the above expression is approximated by

$$\begin{aligned} p(n; V_d, \rho) &\stackrel{N_{tot} \gg n}{\approx} \frac{1}{n!} N_{tot}^n \left(\frac{\rho V_d}{N_{tot}}\right)^n \left(1 - \frac{\rho V_d}{N_{tot}}\right)^{N_{tot}} \\ &\stackrel{N_{tot} \rightarrow \infty}{\rightarrow} \frac{1}{n!} (\rho V_d)^n \exp(-\rho V_d) \\ &= \text{Poisson}_\mu(n) \quad \text{with} \quad \mu = \rho V_d. \end{aligned} \quad (\text{D.2})$$

In the limit  $N_{tot} \rightarrow \infty$  in the second step, one keeps the density  $\rho = N_{tot}/V_{tot}$  constant which is identical to just appending more and more volume with constant density in all directions of space.

The result is a Poissonian distribution  $\mathcal{P}_\mu(n)$  for the particle number within the volume  $V_d$ , weighted by the mean  $\mu(r) = \rho V_d(r)$  - which is equal to the average number of particles in the volume. The resulting form is coherent with the fact that the Poissonian distribution describes a distribution of uncorrelated events with uniform probability of occurrence, as was initially assumed for the particle distribution. As is well known, the Poissonian distribution is normalised in the sum over particle number  $n$  for any given  $\mu \geq 0$ , the expectation value for number of particles within the volume is given by  $\mu = \rho V_d$  and the standard deviation by  $\sigma = \sqrt{\mu}$ . This is shown in Figure D.1 (b).

When calculating the statistical distribution of neighboring Rydberg atoms, one has to take the Rydberg blockade into account which gives a radius  $r_b$  within which one cannot excite a second Rydberg atom (see also Chapter 3). In the saturated regime [198], the neighboring Rydberg atoms are packed densely. However, far from the saturation regime we expect the probability of finding exactly  $n$  Rydberg atoms within a shell to scale almost identical as for the case without blockade. This approach does not account for the blockade volume of the other Rydberg atoms and is therefore approximately valid only in the regime where the average Rydberg atom spacing  $r_{av}$  is much larger than the blockade radius, i.e.  $r_{av} \gg r_b$ . The effect of Rydberg blockade on the distribution of neighboring Rydberg atoms was taken into account in [199].

In the regime far from saturation, the resulting probabilities for finding exactly  $n$  Rydberg atoms within a sphere of radius  $r$  therefore depends on the density  $\rho$  and the dimension  $d$  of the problem. An example for the 2-dimensional case is shown in Figure D.1 (c). For the purposes of this thesis, we are interested in the number of particles within a sphere of radius  $r$  in three dimensions. Therefore, we set  $\mu_{3D}(r) = \frac{4}{3}\pi\rho r^3$  for any further calculations.

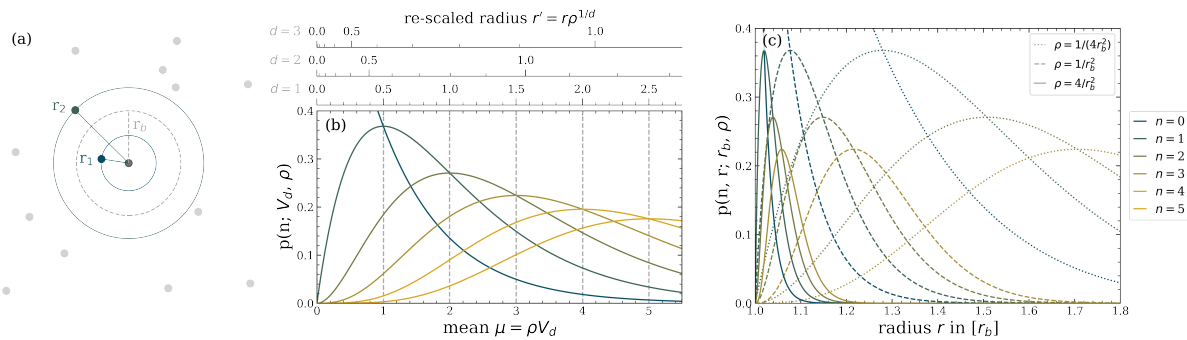


**Fig. D.1: Spatial distribution of particles in  $d$  dimensions.** (a) shows an illustration of the nearest-neighbor distance problem for the case of  $d = 2$ . In (b), the probability of finding exactly  $n$  particles in a spherical volume defined by  $\mu = \rho V_d$  are shown and the resulting re-scaled radii  $r' = r\rho^{1/d}$  are plotted above the graph for the dimensions  $d \in \{1, 2, 3\}$ . The scaling of  $p_n(n, r; r_b, \rho)$  with the ratio of density  $\rho$  to blockade radius  $r_b$  is shown in (c) for  $n \in \{0, 1, 2, 3\}$ .

## E | NEW TA-SHG LASER @ 480 NM

A second, new coupling laser for future experiments with two different Rydberg states was installed on the laser table. The laser is a TA-SHG pro at 960/480 nm from Toptica with 480 nm output powers of up to  $\sim 1.2$  W. The laser was named *Margit*<sup>1</sup>, which is an old German name meaning *child of light*.

The seed laser diode at 960 nm is locked to an ultrastable high-finesse cavity via error signal generation using the cavity reflection spectrum together with a PDH scheme. Further details on the laser lock are given in Appendix F.

Due to the high output powers, the laser must be handled with care. When focussing the laser beam down to lower beam waists one must be careful not to destroy conventional optics as the laser can easily exceed the standard energy density damage thresholds.

Scattering losses in optical fibers are significant at these short wavelengths of  $\sim 480$  nm. This problem occurs predominantly at high laser powers, but also leads to generally lower coupling efficiencies. A maximum coupling efficiency of 66% has been achieved for up to 600 mW incident power. When re-doing the fiber coupling it is paramount to reduce the incident laser power to a minimum. Otherwise, the high powers may be focussed anywhere on the surface of the fiber which causes the fiber head to degrade from heat. Similarly, when operating the fiber at high incident powers, a slow heat-induced degradation of the surface can occur even for optimum beam alignment. If the surface has degraded, a simple polishing of the fiber head with a fiber polishing kit repairs most damage.

Nonetheless, to achieve long lifetimes of the fiber it has to be handled with great care and only as much power as necessary for the experiment should be sent through the fiber. The remaining surplus power can easily be guided into a beam dump.

---

<sup>1</sup>After the first person was stung by the high power beam it has been agreed by the lab crew that the laser's nickname, being the second syllable of its name, is very appropriate.

## F | CAVITY LOCK

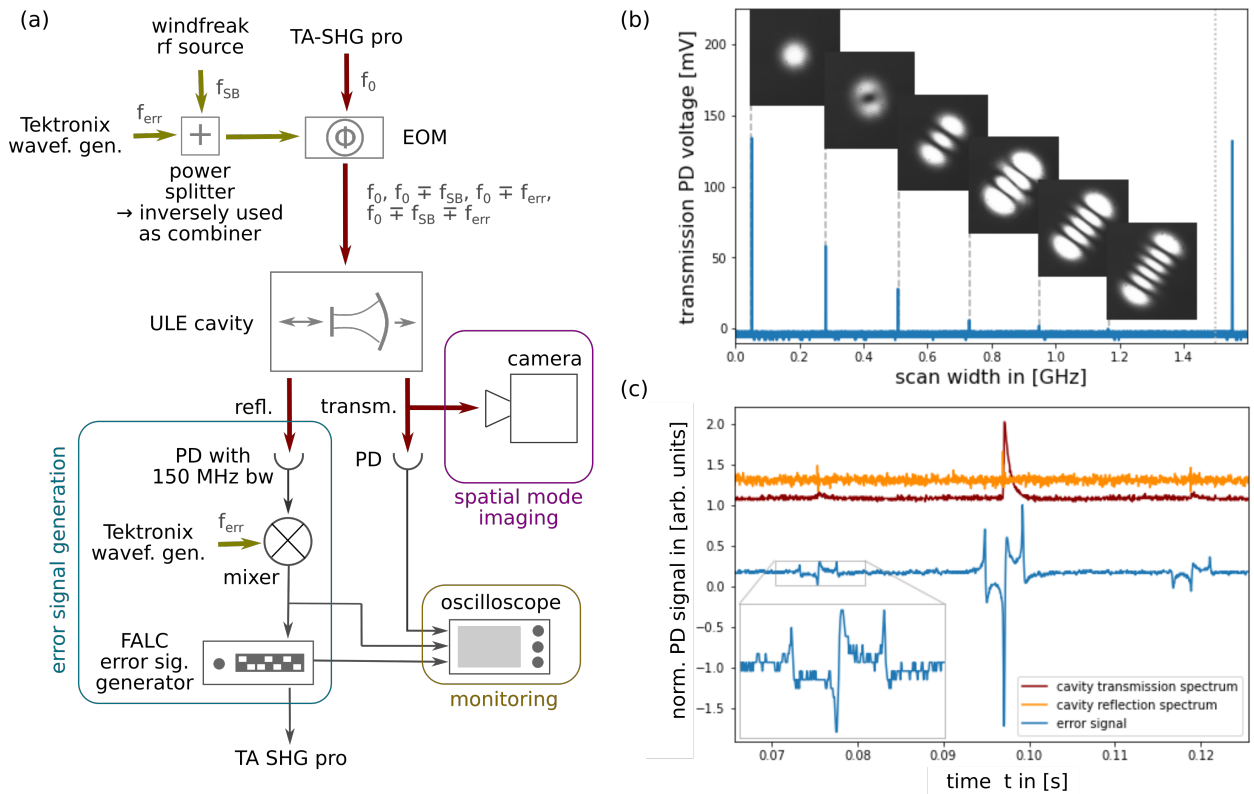


**Fig. F.1: Schematics of cavity lock.** The schematic structure of a sideband cavity lock is shown in (a), further details can be found in the main text. Panel (b) shows the TEM mode spectrum transmitted through the cavity. The generated error signal with the inset showing a zoom-in of one EOM-generated sideband is shown in (c). We use FALCs from Toptica to generate the error signal that is eventually fed back to the laser diode.

In a three-level excitation scheme, the coupling laser has to be locked onto or scanned through the two-photon resonance. Two-photon EIT locks [200, 201] are an option, but require comparably much coupling laser power which might not be available. Therefore, the standard solution is to use cavities to generate an artificial atomic resonance which can similarly be used for the generation of an error signal. The fundamental light at  $\sim 960$  nm of the existing (old) TA-SHG pro laser system had therefore been locked to an ultrastable, ultralow expansion (ULE) reference cavity. Details on the cavity and the previous lock of the old laser system can be found in

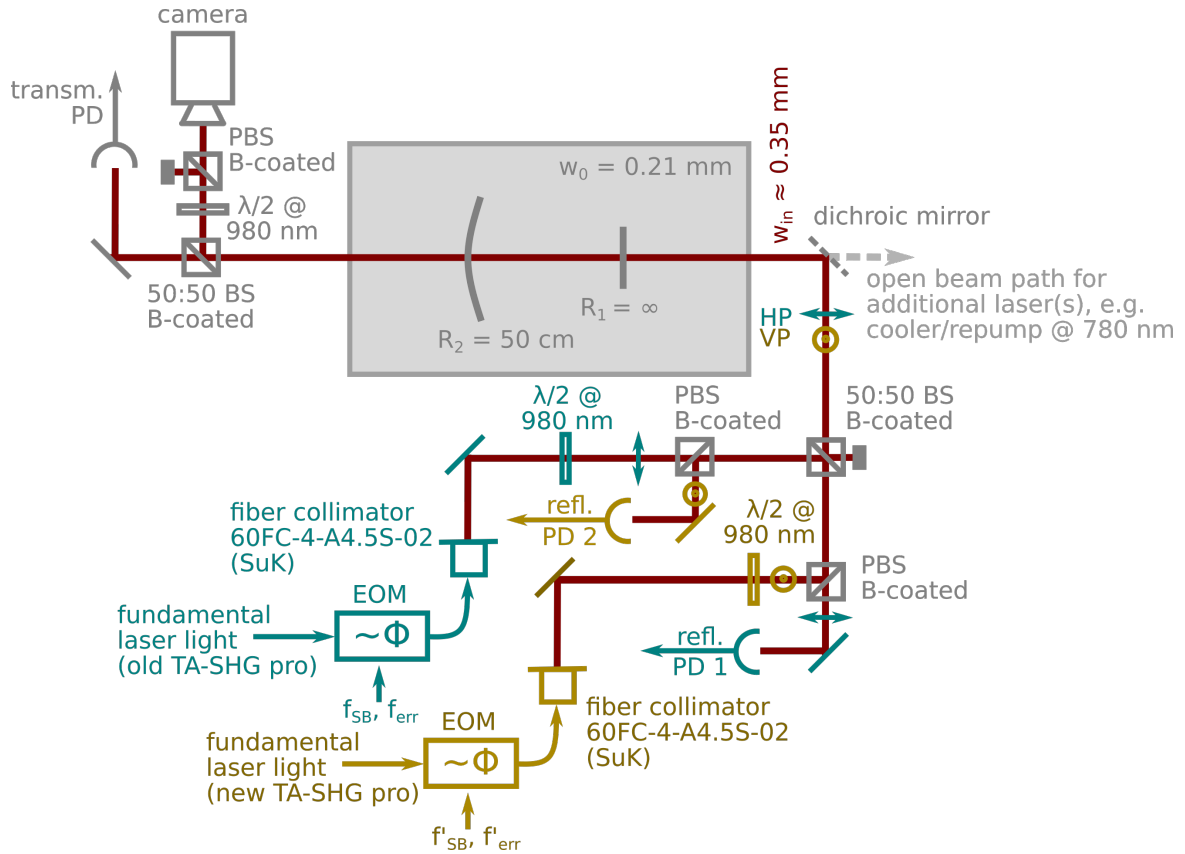


**Fig. F.2: Optical setup of cavity lock for two lasers at  $\sim 960 \text{ nm}$ .** The beam paths for the old (teal) and new (yellow) TA-SHG pro laser systems are shown and the relevant parts are specified in the graph. We use fiber-coupled EOMs of the PMxxx series from Jenoptik. Since both lasers are polarised perpendicularly, the reflected light falls only on a single reflection photodetectors and the polarising optics for spatial mode imaging of the light transmitted through the cavity can select either of the two lasers.

the PhD thesis of Nicholas Spong [147]. Since the cavity spectrum does not necessarily match the desired frequency for the lock point, one has to lock onto the sideband of an electro-optic modulator (EOM) instead. The frequency of the sideband can be adjusted as required, which allows for an arbitrary lock point in the spectrum [184, 185]. An example for the cavity spectrum of the ULE cavity and the error signal generated from the  $\text{TEM}_{00}$  mode and EOM sidebands are shown in Figure F.1 (b) and (c), respectively. A schematic representation of a cavity lock is shown in Figure F.1 (a).

Details on the principle of a sideband lock can be found in e.g. [184, 185]. It might be relevant to note, though, that the sideband lock can also be used to scan the coupling laser through resonance in a controllable fashion as a sideband scan lock.

For this, the sideband frequency  $f_{SB}$  is scanned slowly which changes the frequency of the zero crossing of the error signal generated by the sideband. We have found that a tweaking of the FALC settings for error signal generation towards a more aggressive lock allows for larger scan

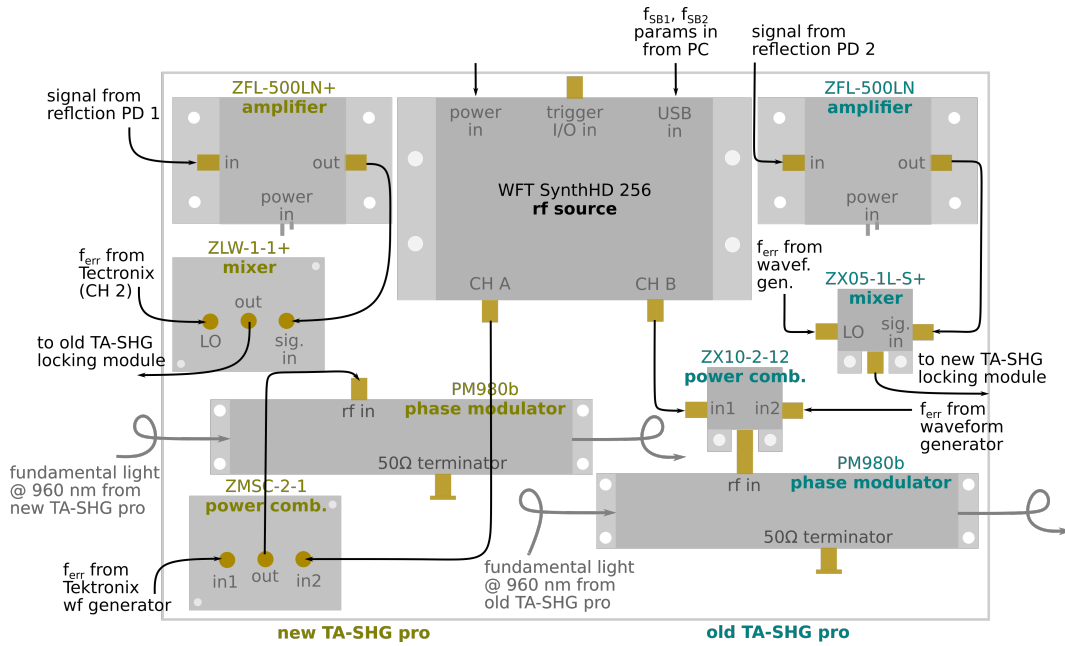


**Fig. F.3: Electronics setup of cavity lock.** The wiring of the electronics and the parts are specified in the graph. All electronic parts are from MiniCircuits, the fiber-coupled phase modulators from Jenoptik.

widths and faster scan rates. The maximum stable operation we have achieved<sup>1</sup> with a sideband scan lock was for scan rates of 0.1 MHz / 10 ms over scan ranges of 140 MHz of fundamental light, i.e. 280 MHz at  $\sim 480$  nm.

It is easily possible to lock multiple lasers onto the same cavity<sup>2</sup>, e.g. when the wavelengths of the lasers are different enough to separate the light with dichroic mirrors. Since both the old and new TA-SHG pro operate at  $\sim 960$  nm fundamental light, we have distinguished them by polarisation instead. The 50:50 beamsplitter used to combine the lasers onto the same beam path leads to 75% losses of the incident light until detection. For our systems, this was not an issue as we receive enough pickup light from the 960 nm diode to still get strong enough a signal on the photodetectors. The resulting cross-talk between the lasers is  $\sim 1\%$  of the incident power after the EOMs, which is negligibly small and did not have a detrimental effect on the quality of the locks.

The optical setup used to lock both lasers onto the same cavity is shown in Figure F.2 and the laser polarisations as well as the relevant parts are specified. The corresponding board carrying the electronics with part specification is shown in Figure F.3.

<sup>1</sup>The maximum scan ranges and scan speed will depend on the specifics of the electronics, error signal generator, laser diode and signal quality. The quality of the signal and optimisation of the generated error signal are key for obtaining stable and fast scans over large scan ranges without loosing the laser out of the lock. It is then even possible to scan across higher-order TEM cavity modes without unlocking of the laser.

<sup>2</sup>As long as the lasers fall within the wavelength range of the cavity mirror's coating. If the lasers fall outside the specified range of the coating one can still use the cavity for locking as long as one gets a decent spectrum. Just try, you might actually be lucky!

## G | BIBLIOGRAPHY

- [1] Z. Néda, E. Ravasz, Y. Brechet, T. Vicsek, and A.-L. Barabási, “The sound of many hands clapping”, *Nature* **403**, 849–850 (2000).
- [2] J. Pantaleone, “Synchronization of metronomes”, *American Journal of Physics* **70**, 992–1000 (2002).
- [3] J. Buck, “Synchronous Rhythmic Flashing of Fireflies. II.”, *The Quarterly Review of Biology* **63**, 265–289 (1988).
- [4] S. H. Strogatz, “From Kuramoto to Crawford: exploring the onset of synchronization in populations of coupled oscillators”, *Physica D* **143**, 1–20 (2000).
- [5] J. A. Acebrón, L. L. Bonilla, C. J. P. Vicente, F. Ritort, and R. Spigler, “The Kuramoto model: A simple paradigm for synchronization phenomena”, *Rev. Mod. Phys.* **77** **77**, 137–185 (2005).
- [6] Y. Kuramoto, “Chemical Turbulence”, 111–140 (1984).
- [7] G. Ertl, “Oscillatory Kinetics and Spatio-Temporal Self-Organization in Reactions at Solid Surfaces”, *Science* **254**, 1750–1755 (1991).
- [8] I. Z. Kiss, Y. Zhai, and J. L. Hudson, “Emerging Coherence in a Population of Chemical Oscillators”, *Science* **296**, 1676–1678 (2002).
- [9] I. Belykh, M. Bocian, A. R. Champneys, K. Daley, R. Jeter, J. H. G. Macdonald, and A. McRobie, “Emergence of the London Millennium Bridge instability without synchronisation”, *Nature Communications* **12** (2021) 10.1038/s41467-021-27568-y.
- [10] P. Dallard, T. Fitzpatrick, A. Flint, A. Low, R. R. Smith, M. Willford, and M. Roche, “London Millennium Bridge: Pedestrian-Induced Lateral Vibration”, *Journal of Bridge Engineering* **6**, 412–417 (2001).
- [11] A. T. Winfree, “Biological rhythms and the behavior of populations of coupled oscillators”, *Journal of Theoretical Biology* **16**, 15–42 (1967).
- [12] Y. Kuramoto, “Self-entrainment of a population of coupled non-linear oscillators”, in *International Symposium on Mathematical Problems in Theoretical Physics* (Springer-Verlag), pp. 420–422.
- [13] A. R. Willms, P. M. Kitanov, and W. F. Langford, “Huygens’ clocks revisited”, *Royal Society Open Science* **4**, 170777 (2017).
- [14] A. T. Winfree, “The prehistory of the Belousov-Zhabotinsky oscillator”, *Journal of Chemical Education* **61**, 661 (1984).

- 
- [15] J. L. Hudson and J. C. Mankin, “Chaos in the Belousov-Zhabotinskii reaction”, *The Journal of Chemical Physics* **74**, 6171–6177 (1981).
- [16] M. O. Scully and M. S. Zubairy, *Quantum Optics* (Cambridge University Press, 1997).
- [17] Y. O. Dudin, L. Li, F. Bariani, and A. Kuzmich, “Observation of coherent many-body Rabi oscillations”, *Nature Physics* **8**, 790–794 (2012).
- [18] M. Fleischhauer, A. Imamoglu, and J. P. Marangos, “Electromagnetically induced transparency: Optics in coherent media”, *Reviews of Modern Physics* **77**, 633–673 (2005).
- [19] S. H. Autler and C. H. Townes, “Stark Effect in Rapidly Varying Fields”, *Physical Review* **100**, 703–722 (1955).
- [20] S. Chen, D. J. Reed, A. R. MacKellar, L. A. Downes, N. F. A. Almuhawish, M. J. Jamieson, C. S. Adams, and K. J. Weatherill, “Terahertz electrometry via infrared spectroscopy of atomic vapor”, *Optica* **9**, 485 (2022).
- [21] R. Finkelstein, S. Bali, O. Firstenberg, and I. Novikova, “A practical guide to electromagnetically induced transparency in atomic vapor”, *New Journal of Physics* **25**, 035001 (2023).
- [22] H. Morishita, T. Tashima, D. Mima, H. Kato, T. Makino, S. Yamasaki, M. Fujiwara, and N. Mizuochi, “Extension of the Coherence Time by Generating MW Dressed States in a Single NV Centre in Diamond”, *Scientific Reports* **9** (2019) 10.1038/s41598-019-49683-z.
- [23] M. Steger, K. Saeedi, M. L. W. Thewalt, J. J. L. Morton, H. Riemann, N. V. Abrosimov, P. Becker, and H.-J. Pohl, “Quantum Information Storage for over 180 s Using Donor Spins in a <sup>28</sup>Si “Semiconductor Vacuum””, **336**, 1280–1283 (2012).
- [24] H. Fan, S. Kumar, J. Sedlacek, H. Kübler, S. Karimkashi, and J. P. Shaffer, “Atom based RF electric field sensing”, *Journal of Physics B: Atomic, Molecular and Optical Physics* **48**, 202001 (2015).
- [25] N. Prajapati, A. Rotunno, S. Berweger, M. Simons, A. Artusio-Glimpse, and C. L. Holloway, “TV and Video Game Streaming with a Quantum Receiver: A Study on a Rydberg atom-based receivers bandwidth and reception clarity”, (2022) 10.48550/ARXIV.2205.02716.
- [26] C. L. Holloway, J. A. Gordon, S. Jefferts, A. Schwarzkopf, D. A. Anderson, S. A. Miller, N. Thaicharoen, and G. Raithel, “Broadband Rydberg Atom-Based Electric-Field Probe for SI-Traceable, Self-Calibrated Measurements”, *IEEE Transactions on Antennas and Propagation* **62**, 6169–6182 (2014).
- [27] S. E. Harris, J. E. Field, and A. Imamoglu, “Nonlinear optical processes using electromagnetically induced transparency”, *Physical Review Letters* **64**, 1107–1110 (1990).
- [28] K.-J. Boller, A. Imamoglu, and S. E. Harris, “Observation of electromagnetically induced transparency”, *Physical Review Letters* **66**, 2593–2596 (1991).
- [29] M. D. Lukin, “Colloquium: Trapping and manipulating photon states in atomic ensembles”, *Reviews of Modern Physics* **75**, 457–472 (2003).
- [30] M. Fleischhauer and M. D. Lukin, “Dark-State Polaritons in Electromagnetically Induced Transparency”, *Physical Review Letters* **84**, 5094–5097 (2000).

- [31] C. Liu, Z. Dutton, C. H. Behroozi, and L. V. Hau, “Observation of coherent optical information storage in an atomic medium using halted light pulses”, *Nature* **409**, 490–493 (2001).
- [32] D. F. Phillips, A. Fleischhauer, A. Mair, R. L. Walsworth, and M. D. Lukin, “Storage of Light in Atomic Vapor”, *Physical Review Letters* **86**, 783–786 (2001).
- [33] I. Carusotto and C. Ciuti, “Quantum fluids of light”, *Reviews of Modern Physics* **85**, 299–366 (2013).
- [34] H. Deng, G. Weihs, C. Santori, J. Bloch, and Y. Yamamoto, “Condensation of Semiconductor Microcavity Exciton Polaritons”, *Science* **298**, 199–202 (2002).
- [35] J. Kasprzak, M. Richard, S. Kundermann, A. Baas, P. Jeambrun, J. M. J. Keeling, F. M. Marchetti, M. H. Szymańska, R. André, J. L. Staehli, V. Savona, P. B. Littlewood, B. Deveaud, and L. S. Dang, “Bose–Einstein condensation of exciton polaritons”, *Nature* **443**, 409–414 (2006).
- [36] G. Lerario, A. Fieramosca, F. Barachati, D. Ballarini, K. S. Daskalakis, L. Dominici, M. D. Giorgi, S. A. Maier, G. Gigli, S. Kéna-Cohen, and D. Sanvitto, “Room-temperature superfluidity in a polariton condensate”, *Nature Physics* **13**, 837–841 (2017).
- [37] Y. Sun, P. Wen, Y. Yoon, G. Liu, M. Steger, L. N. Pfeiffer, K. West, D. W. Snoke, and K. A. Nelson, “Bose–Einstein Condensation of Long-Lifetime Polaritons in Thermal Equilibrium”, *Physical Review Letters* **118**, 016602 (2017).
- [38] D. Maxwell, D. J. Szwer, D. Paredes-Barato, H. Busche, J. D. Pritchard, A. Gauguet, K. J. Weatherill, M. P. A. Jones, and C. S. Adams, “Storage and Control of Optical Photons Using Rydberg Polaritons”, *Physical Review Letters* **110**, 103001 (2013).
- [39] N. L. Spong, Y. Jiao, O. D. Hughes, K. J. Weatherill, I. Lesanovsky, and C. S. Adams, “Collectively Encoded Rydberg Qubit”, *Physical Review Letters* **127**, 063604 (2021).
- [40] H. Busche, P. Huillery, S. W. Ball, T. Ilieva, M. P. A. Jones, and C. S. Adams, “Contactless nonlinear optics mediated by long-range Rydberg interactions”, *Nature Physics* **13**, 655–658 (2017).
- [41] O. Firstenberg, C. S. Adams, and S. Hofferberth, “Nonlinear quantum optics mediated by Rydberg interactions”, *Journal of Physics B: Atomic, Molecular and Optical Physics* **49**, 152003 (2016).
- [42] O. Firstenberg, T. Peyronel, Q.-Y. Liang, A. V. Gorshkov, M. D. Lukin, and V. Vuletić, “Attractive photons in a quantum nonlinear medium”, *Nature* **502**, 71–75 (2013).
- [43] A. K. Mohapatra, T. R. Jackson, and C. S. Adams, “Coherent Optical Detection of Highly Excited Rydberg States Using Electromagnetically Induced Transparency”, *Physical Review Letters* **98**, 113003 (2007).
- [44] K. J. Weatherill, J. D. Pritchard, R. P. Abel, M. G. Bason, A. K. Mohapatra, and C. S. Adams, “Electromagnetically induced transparency of an interacting cold Rydberg ensemble”, *Journal of Physics B: Atomic, Molecular and Optical Physics* **41**, 201002 (2008).

- 
- [45] G. Günter, M. R. de Saint-Vincent, H. Schempp, C. S. Hofmann, S. Whitlock, and M. Weidemüller, “Interaction Enhanced Imaging of Individual Rydberg Atoms in Dense Gases”, *Physical Review Letters* **108**, 013002 (2012).
- [46] A. K. Mohapatra, M. G. Bason, B. Butscher, K. J. Weatherill, and C. S. Adams, “A giant electro-optic effect using polarizable dark states”, *Nature Physics* **4**, 890–894 (2008).
- [47] J. A. Sedlacek, A. Schwettmann, H. Kübler, and J. P. Shaffer, “Atom-Based Vector Microwave Electrometry Using Rubidium Rydberg Atoms in a Vapor Cell”, *Physical Review Letters* **111**, 063001 (2013).
- [48] V. I. Yudin, A. V. Taichenachev, Y. O. Dudin, V. L. Velichansky, A. S. Zibrov, and S. A. Zibrov, “Vector magnetometry based on electromagnetically induced transparency in linearly polarized light”, *Physical Review A* **82**, 033807 (2010).
- [49] K. Cox, V. I. Yudin, A. V. Taichenachev, I. Novikova, and E. E. Mikhailov, “Measurements of the magnetic field vector using multiple electromagnetically induced transparency resonances in Rb vapor”, *Physical Review A* **83**, 015801 (2011).
- [50] M. D. Eisaman, A. André, F. Massou, M. Fleischhauer, A. S. Zibrov, and M. D. Lukin, “Electromagnetically induced transparency with tunable single-photon pulses”, *Nature* **438**, 837–841 (2005).
- [51] Y.-F. Hsiao, P.-J. Tsai, H.-S. Chen, S.-X. Lin, C.-C. Hung, C.-H. Lee, Y.-H. Chen, Y.-F. Chen, I. A. Yu, and Y.-C. Chen, “Highly Efficient Coherent Optical Memory Based on Electromagnetically Induced Transparency”, *Physical Review Letters* **120**, 183602 (2018).
- [52] E. Poem, R. Finkelstein, O. Michel, O. Lahad, and O. Firstenberg, “Fast, noise-free memory for photon synchronization at room temperature”, (2018) [10.1109/acp.2018.8596149](https://arxiv.org/abs/10.1109/acp.2018.8596149).
- [53] W. Demtröder, *Atoms, Molecules and Photons* (Springer, 2018).
- [54] D. A. Steck, *Rubidium 85 D Line Data*, (online, last accessed: 11/07/2023), last accessed: 11.07.2023.
- [55] D. A. Steck, *Rubidium 87 D Line Data*, (online, last accessed: 11/07/2023).
- [56] A. Tauschinsky, R. Newell, H. B. van Linden van den Heuvell, and R. J. C. Spreeuw, “Measurement of  $^{87}\text{Rb}$  Rydberg-state hyperfine splitting in a room-temperature vapor cell”, *Physical Review A* **87**, 042522 (2013).
- [57] C. R. Higgins and I. G. Hughes, “Electromagnetically induced transparency in a V-system with  $^{87}\text{Rb}$  vapour in the hyperfine Paschen-Back regime”, *Journal of Physics B: Atomic, Molecular and Optical Physics* **54**, 165403 (2021).
- [58] A. M. Kaufman, B. J. Lester, and C. A. Regal, “Cooling a Single Atom in an Optical Tweezer to Its Quantum Ground State”, *Physical Review X* **2**, 041014 (2012).
- [59] N. Šibalić, “Rydberg atom ensembles under dephasing and dissipation: from single- to many-body dynamics”, PhD thesis (Durham University, 2017).
- [60] D. J. Whiting, N. Šibalić, J. Keaveney, C. S. Adams, and I. G. Hughes, “Single-Photon Interference due to Motion in an Atomic Collective Excitation”, *Physical Review Letters* **118**, 253601 (2017).

- [61] G. Biedermann, H. J. McGuinness, A. V. Rakholia, Y.-Y. Jau, D. R. Wheeler, J. D. Sterk, and G. R. Burns, “Atom Interferometry in a Warm Vapor”, *Physical Review Letters* **118**, 163601 (2017).
- [62] P. Geppert, M. Althön, D. Fichtner, and H. Ott, “Diffusive-like redistribution in state-changing collisions between Rydberg atoms and ground state atoms”, *Nature Communications* **12** (2021) 10.1038/s41467-021-24146-0.
- [63] D. Weller, J. P. Shaffer, T. Pfau, R. Löw, and H. Kübler, “Interplay between thermal Rydberg gases and plasmas”, *Physical Review A* **99**, 043418 (2019).
- [64] G. Vitrant, J. M. Raimond, M. Gross, and S. Haroche, “Rydberg to plasma evolution in a dense gas of very excited atoms”, *Journal of Physics B: Atomic and Molecular Physics* **15**, L49–L55 (1982).
- [65] D. A. Anderson, G. Raithel, M. Simons, and C. L. Holloway, “Quantum-optical spectroscopy for plasma electric field measurements and diagnostics”, (2017) 10.48550/ARXIV.1712.08717.
- [66] D. C. Aveline, J. R. Williams, E. R. Elliott, C. Dutenhoffer, J. R. Kellogg, J. M. Kohel, N. E. Lay, K. Oudrhiri, R. F. Shotwell, N. Yu, and R. J. Thompson, “Observation of Bose–Einstein condensates in an Earth-orbiting research lab”, *Nature* **582**, 193–197 (2020).
- [67] D. J. Fixsen, “The temperature of the cosmic microwave background”, *The Astrophysical Journal* **707**, 916–920 (2009).
- [68] S. Knappe, V. Shah, P. D. D. Schwindt, L. Hollberg, J. Kitching, L.-A. Liew, and J. Moreland, “A microfabricated atomic clock”, *Applied Physics Letters* **85**, 1460–1462 (2004).
- [69] D. A. Anderson, R. E. Sapiro, and G. Raithel, “Rydberg Atoms for Radio-Frequency Communications and Sensing: Atomic Receivers for Pulsed RF Field and Phase Detection”, *IEEE Aerospace and Electronic Systems Magazine* **35**, 48–56 (2020).
- [70] C. G. Wade, N. Šibalić, N. R. de Melo, J. M. Kondo, C. S. Adams, and K. J. Weatherill, “Real-time near-field terahertz imaging with atomic optical fluorescence”, *Nature Photonics* **11**, 40–43 (2016).
- [71] M. Hosseini, B. Sparkes, G. Campbell, P. Lam, and B. Buchler, “High efficiency coherent optical memory with warm rubidium vapour”, *Nature Communications* **2** (2011) 10.1038/ncomms1175.
- [72] F. Ferri, R. Rosa-Medina, F. Finger, N. Dogra, M. Soriente, O. Zilberberg, T. Donner, and T. Esslinger, “Emerging Dissipative Phases in a Superradiant Quantum Gas with Tunable Decay”, *Physical Review X* **11**, 041046 (2021).
- [73] H. Keßler, P. Kongkhambut, C. Georges, L. Mathey, J. G. Cosme, and A. Hemmerich, “Observation of a Dissipative Time Crystal”, *Physical Review Letters* **127**, 043602 (2021).
- [74] N. Sibalic and C. S. Adams, *Rydberg Physics* (IOP Publishing, 2018).
- [75] C. S. Adams, J. D. Pritchard, and J. P. Shaffer, “Rydberg atom quantum technologies”, *Journal of Physics B: Atomic, Molecular and Optical Physics* **53**, 012002 (2019).

- 
- [76] J. D. Pritchard, K. J. Weatherill, and C. S. Adams, “Nonlinear optics using cold Rydberg atoms”, in *Annual Review of Cold Atoms and Molecules* (World Scientific, 2013), pp. 301–350.
- [77] C. Murray and T. Pohl, “Quantum and Nonlinear Optics in Strongly Interacting Atomic Ensembles”, in *Advances In Atomic, Molecular, and Optical Physics* (Elsevier, 2016), pp. 321–372.
- [78] T. Peyronel, O. Firstenberg, Q.-Y. Liang, S. Hofferberth, A. V. Gorshkov, T. Pohl, M. D. Lukin, and V. Vuletić, “Quantum nonlinear optics with single photons enabled by strongly interacting atoms”, *Nature* **488**, 57–60 (2012).
- [79] M. Saffman, T. G. Walker, and K. Mølmer, “Quantum information with Rydberg atoms”, *Reviews of Modern Physics* **82**, 2313–2363 (2010).
- [80] M. D. Lukin, M. Fleischhauer, R. Cote, L. M. Duan, D. Jaksch, J. I. Cirac, and P. Zoller, “Dipole Blockade and Quantum Information Processing in Mesoscopic Atomic Ensembles”, *Physical Review Letters* **87**, 037901 (2001).
- [81] M Saffman, “Quantum computing with atomic qubits and Rydberg interactions: progress and challenges”, *Journal of Physics B: Atomic, Molecular and Optical Physics* **49**, 202001 (2016).
- [82] A. Browaeys and T. Lahaye, “Many-body physics with individually controlled Rydberg atoms”, *Nature Physics* **16**, 132–142 (2020).
- [83] H. Weimer, M. Müller, I. Lesanovsky, P. Zoller, and H. P. Büchler, “A Rydberg quantum simulator”, *Nature Physics* **6**, 382–388 (2010).
- [84] T. F. Gallagher, *Rydberg Atoms* (Cambridge University Press, 2005).
- [85] D. E. Chang, V. Vuletić, and M. D. Lukin, “Quantum nonlinear optics — photon by photon”, *Nature Photonics* **8**, 685–694 (2014).
- [86] O. Firstenberg, T. Peyronel, Q.-Y. Liang, A. V. Gorshkov, M. D. Lukin, and V. Vuletić, “Attractive photons in a quantum nonlinear medium”, *Nature* **502**, 71–75 (2013).
- [87] W. Li, I. Mourachko, M. W. Noel, and T. F. Gallagher, “Millimeter-wave spectroscopy of cold Rb Rydberg atoms in a magneto-optical trap: Quantum defects of the ns, np, and nd series”, *Physical Review A* **67**, 052502 (2003).
- [88] J. Han, Y. Jamil, D. V. L. Norum, P. J. Tanner, and T. F. Gallagher, “Rb nf quantum defects from millimeter-wave spectroscopy of cold 85Rb Rydberg atoms”, *Physical Review A* **74**, 054502 (2006).
- [89] M. Mack, F. Karlewski, H. Hattermann, S. Höckh, F. Jessen, D. Cano, and J. Fortágh, “Measurement of absolute transition frequencies of 87Rb to nS and nD Rydberg states by means of electromagnetically induced transparency”, *Physical Review A* **83**, 052515 (2011).
- [90] W. E. Cooke and T. F. Gallagher, “Effects of blackbody radiation on highly excited atoms”, *Physical Review A* **21**, 588–593 (1980).
- [91] I. I. Beterov, I. I. Ryabtsev, D. B. Tretyakov, and V. M. Entin, “Quasiclassical calculations of blackbody-radiation-induced depopulation rates and effective lifetimes of Rydberg nS, nP, and nD alkali-metal atoms with  $n \leq 80$ ”, *Physical Review A* **79**, 052504 (2009).

- 
- [92] T. F. Gallagher and W. E. Cooke, “Interactions of Blackbody Radiation with Atoms”, *Physical Review Letters* **42**, 835–839 (1979).
- [93] W. P. Spencer, A. G. Vaidyanathan, D. Kleppner, and T. W. Ducas, “Temperature dependence of blackbody-radiation-induced transfer among highly excited states of sodium”, *Physical Review A* **25**, 380–384 (1982).
- [94] H.-T. Tu, K.-Y. Liao, G.-D. He, Y.-F. Zhu, S.-Y. Qiu, H. Jiang, W. Huang, W. Bian, H. Yan, and S.-L. Zhu, “Approaching the standard quantum limit of a Rydberg-atom microwave electrometer”, (2023) [10.48550/ARXIV.2307.15617](https://arxiv.org/abs/10.48550/ARXIV.2307.15617).
- [95] L. A. Downes, L. Torralbo-Campo, and K. J. Weatherill, “A practical guide to terahertz imaging using thermal atomic vapour”, *New Journal of Physics* **25**, 035002 (2023).
- [96] L. Isenhower, E. Urban, X. L. Zhang, A. T. Gill, T. Henage, T. A. Johnson, T. G. Walker, and M. Saffman, “Demonstration of a Neutral Atom Controlled-NOT Quantum Gate”, *Physical Review Letters* **104**, 010503 (2010).
- [97] D. Comparat and P. Pillet, “Dipole blockade in a cold Rydberg atomic sample [Invited]”, *Journal of the Optical Society of America B* **27**, A208 (2010).
- [98] N. Šibalić, J. Pritchard, C. Adams, and K. Weatherill, “ARC: An open-source library for calculating properties of alkali Rydberg atoms”, *Computer Physics Communications* **220**, 319–331 (2017).
- [99] S. Weber, C. Tresp, H. Menke, A. Urvoy, O. Firstenberg, H. P. Büchler, and S. Hofferberth, “Calculation of Rydberg interaction potentials”, *Journal of Physics B: Atomic, Molecular and Optical Physics* **50**, 133001 (2017).
- [100] R. J. L. Roy, “Long-Range Potential Coefficients From RKR Turning Points:  $C_6$  and  $C_8$  for B(3II $\text{O}u^+$ )-State  $\text{Cl}_2$ ,  $\text{Br}_2$ , and  $\text{I}_2$ ”, *Canadian Journal of Physics* **52**, 246–256 (1974).
- [101] B. Ji, C.-C. Tsai, and W. C. Stwalley, “Proposed modification of the criterion for the region of validity of the inverse-power expansion in diatomic long-range potentials”, *Chemical Physics Letters* **236**, 242–246 (1995).
- [102] S. Ravets, H. Labuhn, D. Barredo, T. Lahaye, and A. Browaeys, “Measurement of the angular dependence of the dipole-dipole interaction between two individual Rydberg atoms at a Förster resonance”, *Physical Review A* **92**, 020701 (2015).
- [103] A. Fioretti, D. Comparat, C. Drag, T. F. Gallagher, and P. Pillet, “Long-Range Forces between Cold Atoms”, **82**, 1839–1842.
- [104] K. Afrousheh, P. Bohlouli-Zanjani, D. Vagale, A. Mugford, M. Fedorov, and J. D. D. Martin, “Spectroscopic Observation of Resonant Electric Dipole-Dipole Interactions between Cold Rydberg Atoms”, *Physical Review Letters* **93**, 233001 (2004).
- [105] T. J. Carroll, K. Claringbould, A. Goodsell, M. J. Lim, and M. W. Noel, “Angular Dependence of the Dipole-Dipole Interaction in a Nearly One-Dimensional Sample of Rydberg Atoms”, *Physical Review Letters* **93**, 153001 (2004).
- [106] T. G. Walker and M. Saffman, “Consequences of Zeeman degeneracy for the van der Waals blockade between Rydberg atoms”, *Physical Review A* **77**, 032723 (2008).

- 
- [107] M. Saffman, T. G. Walker, and K. Mølmer, “Quantum information with Rydberg atoms”, *Reviews of Modern Physics* **82**, 2313–2363 (2010).
- [108] L. Béguin, A. Vernier, R. Chicireanu, T. Lahaye, and A. Browaeys, “Direct Measurement of the van der Waals Interaction between Two Rydberg Atoms”, *Physical Review Letters* **110**, 263201 (2013).
- [109] D. Barredo, S. Ravets, H. Labuhn, L. Béguin, A. Vernier, F. Nogrette, T. Lahaye, and A. Browaeys, “Demonstration of a Strong Rydberg Blockade in Three-Atom Systems with Anisotropic Interactions”, *Physical Review Letters* **112**, 183002 (2014).
- [110] A. Reinhard, T. C. Liebisch, B. Knuffman, and G. Raithel, “Level shifts of rubidium Rydberg states due to binary interactions”, *Physical Review A* **75**, 032712 (2007).
- [111] A. Paris-Mandoki, H. Gorniaczyk, C. Tresp, I. Mirgorodskiy, and S. Hofferberth, “Tailoring Rydberg interactions via Förster resonances: state combinations, hopping and angular dependence”, *Journal of Physics B: Atomic, Molecular and Optical Physics* **49**, 164001 (2016).
- [112] D. A. Varshalovich, A. N. Moskalev, and V. K. Khersonskii (WORLD SCIENTIFIC, 1988), pp. 3–35.
- [113] T. G. Walker and M. Saffman, “Zeros of Rydberg–Rydberg Förster interactions”, *Journal of Physics B: Atomic, Molecular and Optical Physics* **38**, S309–S319 (2005).
- [114] C. Carr, R. Ritter, C. G. Wade, C. S. Adams, and K. J. Weatherill, “Nonequilibrium Phase Transition in a Dilute Rydberg Ensemble”, *Physical Review Letters* **111**, 113901 (2013).
- [115] N. Šibalić, C. G. Wade, C. S. Adams, K. J. Weatherill, and T. Pohl, “Driven-dissipative many-body systems with mixed power-law interactions: Bistabilities and temperature-driven nonequilibrium phase transitions”, *Physical Review A* **94**, 011401 (2016).
- [116] N. R. de Melo, C. G. Wade, N. Šibalić, J. M. Kondo, C. S. Adams, and K. J. Weatherill, “Intrinsic optical bistability in a strongly driven Rydberg ensemble”, *Physical Review A* **93**, 063863 (2016).
- [117] D. Weller, A. Urvoy, A. Rico, R. Löw, and H. Kübler, “Charge-induced optical bistability in thermal Rydberg vapor”, *Physical Review A* **94**, 063820 (2016).
- [118] M. L. Citron, H. R. Gray, C. W. Gabel, and C. R. Stroud, “Experimental study of power broadening in a two-level atom”, *Physical Review A* **16**, 1507–1512 (1977).
- [119] S. E. Harris, J. E. Field, and A. Imamoglu, “Nonlinear optical processes using electromagnetically induced transparency”, *Physical Review Letters* **64**, 1107–1110 (1990).
- [120] K.-J. Boller, A. Imamoglu, and S. E. Harris, “Observation of electromagnetically induced transparency”, *Physical Review Letters* **66**, 2593–2596 (1991).
- [121] M. I. Rosen, “Niels Hendrik Abel and Equations of the Fifth Degree”, *The American Mathematical Monthly* **102**, 495 (1995).
- [122] R. G. Ayoub, “Paolo Ruffini’s contributions to the quintic”, *Archive for History of Exact Sciences* **23**, 253–277 (1980).
- [123] M. Steed, “Proofs of the Fundamental Theorem of Algebra”, (2014).

- [124] R. A. Horn and C. R. Johnson, *Matrix Analysis* (Cambridge University Press, 1985).
- [125] X. Wang, “A Simple Proof of Descartes’s Rule of Signs”, *The American Mathematical Monthly* **111**, 525 (2004).
- [126] A. Fontana, “A Proof of Descartes’ Rule of Signs”, *Ratio Mathematica* **35** (2018) 10.23755/rm.v35i0.425.
- [127] D. Ruelle, *Elements of Differentiable Dynamics and Bifurcation Theory* (Elsevier Science & Technology Books, 2014).
- [128] J. E. Marsden and M. McCracken, *The Hopf Bifurcation and Its Applications* (Springer New York, 1976).
- [129] P. Hartman, *Ordinary Differential Equations* (2002).
- [130] R. Mattes, I. Lesanovsky, and F. Carollo, “Entangled time-crystal phase in an open quantum light-matter system”, (2023) 10.48550/arXiv.2303.07725.
- [131] T. E. Lee, H. Häffner, and M. C. Cross, “Antiferromagnetic phase transition in a nonequilibrium lattice of Rydberg atoms”, *Physical Review A* **84**, 031402 (2011).
- [132] A. J. Lotka, “Undamped Oscillations Derived from the Law of Mass Action”, *Journal of the American Chemical Society* **42**, 1595–1599 (1920).
- [133] V. Volterra, “Fluctuations in the Abundance of a Species considered Mathematically”, *Nature* **118**, 558–560 (1926).
- [134] B. van der Pol, “On relaxation-oscillations”, *The London, Edinburgh, and Dublin Philosophical Magazine and Journal of Science* **2**, 978–992 (1926).
- [135] A. M. Lyapunov, *Genral Problem of the Stability Of Motion*, Vol. 55 (CRC Press, 1992), pp. 531–534.
- [136] Y. A. Kuznetsov, *Elements of Applied Bifurcation Theory* (Springer New York, 1995).
- [137] W. H. Press, S. A. Teukolsky, W. T. Vetterling, and B. P. Flannery, *Numerical Recipes 3rd Edition, The Art of Scientific Computing* (Cambridge University Press, 2007), p. 1256.
- [138] E. Fehlberg, “Klassische Runge-Kutta-Formeln fünfter und siebenter Ordnung mit Schrittweiten-Kontrolle”, *Computing* **4**, 93–106 (1969).
- [139] J. Dormand and P. Prince, “A family of embedded Runge-Kutta formulae”, *Journal of Computational and Applied Mathematics* **6**, 19–26 (1980).
- [140] A. Pikovsky, M. Rosenblum, and J. Kurths, *Synchronisation: A Universal Concept in Non-linear Sciences* (Cambridge University Press, 2001), pp. 1–24.
- [141] R. A. Oliva and S. H. Strogatz, “Dynamics of a large array of globally coupled lasers with distributed frequencies”, *International Journal of Bifurcation and Chaos* **11**, 2359–2374 (2001).
- [142] A. F. Glova, “Phase locking of optically coupled lasers”, *Quantum Electronics* **33**, 283–306 (2003).
- [143] S. Peleš, J. L. Rogers, and K. Wiesenfeld, “Robust synchronization in fiber laser arrays”, *Physical Review E* **73**, 026212 (2006).

- 
- [144] K. Wiesenfeld, P. Colet, and S. H. Strogatz, “Synchronization Transitions in a Disordered Josephson Series Array”, *Physical Review Letters* **76**, 404–407 (1996).
- [145] T. J. Walker, “Acoustic Synchrony: Two Mechanisms in the Snowy Tree Cricket”, *Science* **166**, 891–894 (1969).
- [146] A. Pikovsky and M. Rosenblum, “Self-organized partially synchronous dynamics in populations of nonlinearly coupled oscillators”, *Physica D: Nonlinear Phenomena* **238**, 27–37 (2009).
- [147] N. L. R. Spong, “Coherent manipulation of Rydberg Polaritons”, PhD thesis (Durham University, 2021).
- [148] E. Fermi, J. Pasta, and S. Ulam, *Studies of Nonlinear Problems I*, tech. rep. (Los Alamos Scientific Laboratory, University of California, 1955).
- [149] M. Pettini and M. Landolfi, “Relaxation properties and ergodicity breaking in nonlinear Hamiltonian dynamics”, *Physical Review A* **41**, 768–783 (1990).
- [150] G. P. Berman and F. M. Izrailev, “The Fermi–Pasta–Ulam problem: Fifty years of progress”, *Chaos: An Interdisciplinary Journal of Nonlinear Science* **15**, 015104 (2005).
- [151] G. Benettin, R. Livi, and G. Parisi, “Ergodicity: How Can It Be Broken?”, in *Large Deviations in Physics* (Springer Berlin Heidelberg, 2014), pp. 29–70.
- [152] L. D’Alessio, Y. Kafri, A. Polkovnikov, and M. Rigol, “From quantum chaos and eigenstate thermalization to statistical mechanics and thermodynamics”, *Advances in Physics* **65**, 239–362 (2016).
- [153] T. Mori, T. N. Ikeda, E. Kaminishi, and M. Ueda, “Thermalization and prethermalization in isolated quantum systems: a theoretical overview”, *J. Phys. B* **51**, 112001 (2018) **51**, 112001 (2017).
- [154] A. Shapere and F. Wilczek, “Classical Time Crystals”, *Physical Review Letters* **109**, 160402 (2012).
- [155] F. Wilczek, “Quantum Time Crystals”, *Physical Review Letters* **109**, 160401 (2012).
- [156] H. Watanabe and M. Oshikawa, “Absence of Quantum Time Crystals”, *Physical Review Letters* **114**, 251603 (2015).
- [157] D. V. Else, B. Bauer, and C. Nayak, “Floquet Time Crystals”, *Physical Review Letters* **117**, 090402 (2016).
- [158] S. Choi, J. Choi, R. Landig, G. Kucsko, H. Zhou, J. Isoya, F. Jelezko, S. Onoda, H. Sumiya, V. Khemani, C. von Keyserlingk, N. Y. Yao, E. Demler, and M. D. Lukin, “Observation of discrete time-crystalline order in a disordered dipolar many-body system”, *Nature* **543**, 221–225 (2017).
- [159] J. Zhang, P. W. Hess, A. Kyprianidis, P. Becker, A. Lee, J. Smith, G. Pagano, I.-D. Potirniche, A. C. Potter, A. Vishwanath, N. Y. Yao, and C. Monroe, “Observation of a discrete time crystal”, *Nature* **543**, 217–220 (2017).
- [160] M. P. Zaletel, M. Lukin, C. Monroe, C. Nayak, F. Wilczek, and N. Y. Yao, “Colloquium: Quantum and Classical Discrete Time Crystals”, (2023) <https://doi.org/10.48550/arXiv.2305.08904>.

- [161] P. Hannaford and K. Sacha, “A decade of time crystals: Quo vadis?”, *Europhysics Letters* **139**, 10001 (2022).
- [162] Z. Gong, R. Hamazaki, and M. Ueda, “Discrete Time-Crystalline Order in Cavity and Circuit QED Systems”, *Physical Review Letters* **120**, 040404 (2018).
- [163] H. Taheri, A. B. Matsko, L. Maleki, and K. Sacha, “All-optical dissipative discrete time crystals”, *Nature Communications* **13** (2022) 10.1038/s41467-022-28462-x.
- [164] F. Iemini, A. Russomanno, J. Keeling, M. Schirò, M. Dalmonte, and R. Fazio, “Boundary Time Crystals”, *Physical Review Letters* **121**, 035301 (2018).
- [165] B. Buča, J. Tindall, and D. Jaksch, “Non-stationary coherent quantum many-body dynamics through dissipation”, *Nature Communications* **10** (2019) 10.1038/s41467-019-09757-y.
- [166] D. Dreon, A. Baumgärtner, X. Li, S. Hertlein, T. Esslinger, and T. Donner, “Self-oscillating pump in a topological dissipative atom-cavity system”, *Nature* **608**, 494–498 (2022).
- [167] P. Kongkhambut, J. Skulte, L. Mathey, J. G. Cosme, A. Hemmerich, and H. Keßler, “Observation of a continuous time crystal”, *Science* **377**, 670–673 (2022).
- [168] T. Liu, J.-Y. Ou, K. F. MacDonald, and N. I. Zheludev, “Photonic metamaterial analogue of a continuous time crystal”, *Nature Physics* (2023) 10.1038/s41567-023-02023-5.
- [169] A. Greilich, N. E. Kopteva, A. N. Kamenskii, P. S. Sokolov, V. L. Korenev, and M. Bayer, “Continuous time crystal in an electron-nuclear spin system: stability and melting of periodic auto-oscillations”, (2023) 10.48550/arXiv.2303.15989.
- [170] V. Khemani, R. Moessner, and S. L. Sondhi, “A Brief History of Time Crystals”, (2019) 10.48550/ARXIV.1910.10745.
- [171] F. Gambetta, F. Carollo, M. Marcuzzi, J. Garrahan, and I. Lesanovsky, “Discrete Time Crystals in the Absence of Manifest Symmetries or Disorder in Open Quantum Systems”, *Physical Review Letters* **122**, 015701 (2019).
- [172] T. L. Heugel, M. Oscity, A. Eichler, O. Zilberberg, and R. Chitra, “Classical Many-Body Time Crystals”, *Physical Review Letters* **123**, 124301 (2019).
- [173] F. Iemini, A. Russomanno, J. Keeling, M. Schirò, M. Dalmonte, and R. Fazio, “Boundary Time Crystals”, *Physical Review Letters* **121**, 035301 (2018).
- [174] F. Carollo and I. Lesanovsky, “Exact solution of a boundary time-crystal phase transition: Time-translation symmetry breaking and non-Markovian dynamics of correlations”, *Physical Review A* **105**, 1040202 (2022).
- [175] L. E. Reichl, *A Modern Course in Statistical Physics* (Wiley, 2016).
- [176] D. Pazó, “Thermodynamic limit of the first-order phase transition in the Kuramoto model”, *Physical Review E* **72**, 046211 (2005).
- [177] X. Hu, S. Boccaletti, W. Huang, X. Zhang, Z. Liu, S. Guan, and C.-H. Lai, “Exact solution for first-order synchronization transition in a generalized Kuramoto model”, *Scientific Reports* **4** (2014) <https://doi.org/10.1038/srep07262>.

- 
- [178] G. Filatrella, N. F. Pedersen, and K. Wiesenfeld, “Generalized coupling in the Kuramoto model”, *Physical Review E* **75**, 017201 (2007).
- [179] I. Leyva, R. Sevilla-Escoboza, J. M. Buldú, I. Sendiña-Nadal, J. Gómez-Gardeñes, A. Arenas, Y. Moreno, S. Gómez, R. Jaimes-Reátegui, and S. Boccaletti, “Explosive First-Order Transition to Synchrony in Networked Chaotic Oscillators”, *Physical Review Letters* **108**, 168702 (2012).
- [180] J. K. Jang, X. Ji, C. Joshi, Y. Okawachi, M. Lipson, and A. L. Gaeta, “Observation of Arnold Tongues in Coupled Soliton Kerr Frequency Combs”, *Physical Review Letters* **123**, 153901 (2019).
- [181] T. E. Lee and H. R. Sadeghpour, “Quantum Synchronization of Quantum van der Pol Oscillators with Trapped Ions”, *Physical Review Letters* **111**, 234101 (2013).
- [182] G. C. Bjorklund, “Frequency-modulation spectroscopy: a new method for measuring weak absorptions and dispersions”, *Optics Letters* **5**, 15 (1980).
- [183] D. J. McCarron, S. A. King, and S. L. Cornish, “Modulation transfer spectroscopy in atomic rubidium”, *Measurement Science and Technology* **19**, 105601 (2008).
- [184] J. I. Thorpe, K. Numata, and J. Livas, “Laser frequency stabilization and control through offset sideband locking to optical cavities”, *Optics Express* **16**, 15980 (2008).
- [185] R. Legaie, C. J. Picken, and J. D. Pritchard, “Sub-kilohertz excitation lasers for quantum information processing with Rydberg atoms”, *Journal of the Optical Society of America B* **35**, 892 (2018).
- [186] R. W. P. Drever, J. L. Hall, F. V. Kowalski, J. Hough, G. M. Ford, A. J. Munley, and H. Ward, “Laser Phase and Frequency Stabilisation Using an Optical Resonator”, *Applied Physics B Photophysics and Laser Chemistry* **31**, 97–105 (1983).
- [187] E. D. Black, “An introduction to Pound–Drever–Hall laser frequency stabilization”, *American Journal of Physics* **69**, 79–87 (2001).
- [188] B. E. Sherlock and I. G. Hughes, “How weak is a weak probe in laser spectroscopy?”, *American Journal of Physics* **77**, 111–115 (2009).
- [189] M. A. Zentile, J. Keaveney, L. Weller, D. J. Whiting, C. S. Adams, and I. G. Hughes, “ElecSus: A program to calculate the electric susceptibility of an atomic ensemble”, *Computer Physics Communications* **189**, 162–174 (2015).
- [190] X. Wu, Z. Wang, F. Yang, R. Gao, C. Liang, M. K. Tey, X. Li, T. Pohl, and L. You, “Observation of a dissipative time crystal in a strongly interacting Rydberg gas”, (2023) 10.48550/ARXIV.2305.20070.
- [191] D.-S. Ding, Z. Bai, Z.-K. Liu, B.-S. Shi, G.-C. Guo, W. Li, and C. S. Adams, “Ergodicity breaking from Rydberg clusters in a driven-dissipative many-body system”, (2023) 10.48550/ARXIV.2305.07032.
- [192] P. C. Parks, “A new proof of the Routh-Hurwitz stability criterion using the second method of Liapunov”, *Mathematical Proceedings of the Cambridge Philosophical Society* **58**, 694–702 (1962).

- [193] J. Schachenmayer, A. Pikovski, and A. Rey, “Many-Body Quantum Spin Dynamics with Monte Carlo Trajectories on a Discrete Phase Space”, *Physical Review X* **5**, 011022 (2015).
- [194] P. Hertz, “Über den gegenseitigen durchschnittlichen Abstand von Punkten, die mit bekannter mittlerer Dichte im Raume angeordnet sind”, *Mathematische Annalen* **67**, 387–398 (1909).
- [195] J. Holtzmark, “Über die Verbreiterung von Spektrallinien”, *Annalen der Physik* **363**, 577–630 (1919).
- [196] J.-C. Pain, “Expression of the Holtzmark function in terms of hypergeometric  ${}_2F_2$  and Airy Bi functions”, *The European Physical Journal Plus* **135** (2020) 10. 1140/epjp/s13360-020-00248-4.
- [197] X. Wang, J. He, J. Bai, and J. Wang, “Rydberg Level Shift due to the Electric Field Generated by Rydberg Atom Collision Induced Ionization in Cesium Atomic Ensemble”, *Applied Sciences* **10**, 5646 (2020).
- [198] K. Singer, M. Reetz-Lamour, T. Amthor, L. G. Marcassa, and M. Weidemüller, “Suppression of Excitation and Spectral Broadening Induced by Interactions in a Cold Gas of Rydberg Atoms”, *Physical Review Letters* **93**, 163001 (2004).
- [199] T. Franz, “Quantum Simulation of Relaxation Dynamics of a Heisenberg Hamiltonian Using Rydberg Spins”, MA thesis (2018).
- [200] H. S. Moon, L. Lee, K. Kim, and J. B. Kim, “Laser frequency stabilizations using electromagnetically induced transparency”, *Applied Physics Letters* **84**, 3001–3003 (2004).
- [201] S. C. Bell, D. M. Heywood, J. D. White, J. D. Close, and R. E. Scholten, “Laser frequency offset locking using electromagnetically induced transparency”, *Applied Physics Letters* **90**, 171120 (2007).

## H | ACKNOWLEDGEMENTS

There are many people without whom this thesis would not exist at all, or who have contributed to it in one way or another. In particular, I would like to thank...

... **STUART ADAMS** for the many and long discussions, your infinite supply of ideas, and for your trust in me.

... **MATTHIAS WEIDEMÜLLER** for giving me the opportunity to go to Durham for even more research into Rydberg physics while also being my supervisor.

... the lab crew in ph54, including **LUCY DOWNES**, **MAX FESTENSTEIN**, **OLIVER HUGHES**, and **KEVIN WEATHERILL**. It has been great fun to work with all of you and it was an amazing time even though things didn't always go as planned. Thanks for sharing your lab and all those funny moments with me.

... the wider **QLM GROUP** at Durham – I am not sure whether you know that the QLM environment is maybe not perfect, but still special. Which includes the many people who I have met in this context, and particularly those with whom a friendship has grown out of the lab and into the life beyond. **ANNIKA BELZ** and **ALEX MATTHIES**, I am looking at you. The time in QLM was so much funnier with you, and I won't forget the many bouldering sessions nor the endless walks & talks.

... the **RYDBERG GROUP** in Heidelberg for re-adopting me during the time of thesis writing. It was much nicer to write my thesis with all the coffee breaks and conversations than it would have been without.

To the many people who have taken some of their time to proofread this thesis: Your thoughtful feedback and very helpful comments have much improved this work. My thanks go to **ANNIKA BELZ**, **LUCY DOWNES**, **SEBASTIAN GEIER**, **ALEX MATTHIES**, **FINN MÜNNICH**, **PAULINE SEUBERT**, **EMELY WEICHERT**, and **GERHARD ZÜRN**.

Meinen **FREUND\*INNEN** danke ich für die tolle Zeit im Studium. Frei nach dem Motto *gemeinsam ist man stark* sind wir uns durch das Unilabyrinth geirrt und haben schlussendlich den Weg nach draußen gefunden. Zwischen Vorlesungen und Zettelrechnen war viel Zeit für die schönen und lustigen Dinge im Leben, und wir haben sie ausgiebig genossen. Ohne Euch wären die letzten Jahre einfach nicht dasselbe gewesen. Für die gemeinsame Zeit möchte ich Euch von Herzen danken, ich erinnere mich sehr gerne daran zurück.

Meine **FAMILIE** und ich haben viel zusammen erlebt und gesehen. Ich danke Euch für Eure Unterstützung auf meinem Weg, von klein auf bis an diesen Punkt.

*"Hope  
is the belief in  
the plausibility of the possible,  
as opposed to  
the necessity of the probable."*

(Maimonides)